Understanding Laser-Induced Alignment and Rotation of Molecules Embedded in Helium Nanodroplets

PhD Thesis

Anders Aspegren Søndergaard
Department of Physics and Astronomy
Aarhus University
December 2016

Preface

This thesis was submitted to the Graduate School of Science and Technology at Aarhus University, Denmark, in order to fulfill the requirements for obtaining the PhD degree in physics. The work was carried out from August 2013 to December 2016, under supervision of Professor Henrik Stapelfeldt, at the Department of Chemistry, Aarhus University.

Errata

This edition of the thesis contains the following corrections and additions compared to the officially submitted thesis:

- Mads Bøttger Hansen and Ove Christiansen have been acknowledged.
- References [A1-A2] have been updated since they have now been submitted.
- Section 2.2.5 has been added in the hope that it will stimulate future research.
- The gas phase experiment target chamber pressure has been corrected from 9×10^{-7} mbar to 6×10^{-8} mbar (page 57).
- The caption of Fig. 5.5 duplicated that of of Fig. 5.6 and has been corrected.
- The argument lists of V and W in (6.2) were swapped and are now correct.
- The numerical evaluation of fluences (page 100) used a moment of inertia of I_2 that was a factor 2π too high and the factor $1/2$ under the square root in (6.43) was neglected. The resulting fluences (6.46)-(6.48) have been corrected from $7.1\,\mathrm{J/cm^2}$, $14.5\,\mathrm{J/cm^2}$ and $6.1\,\mathrm{J/cm^2}$ to $1.1\,\mathrm{J/cm^2}$, $4.10\,\mathrm{J/cm^2}$ and $2.45\,\mathrm{J/cm^2}$, respectively. The text "somewhat lower, only about" has been replaced with "about the same," to reflect the better agreement.

Acknowledgement

I would like to thank my supervisor Henrik Stapelfeldt for the exciting opportunity to work with superfluid helium and ultrafast lasers in Femtolab. Henrik

has been a truly excellent supervisor. Thanks to Henriks vast expertise and foresightfulness, leading him to always have many great ideas, there has never been a lack of interesting new directions for my project. I thank him further for always making time for scientific discussions.

Femtolab is a group of highly, yet diversely talented and motivated people, all of whom I thank for contributing to maintaining an enjoyable, stimulating and altogether extraordinary research environment. Of these people, I have worked most closely together with Lars Christiansen and Benjamin Shepperson, from whom I have also learned most of what I know about the experimental equipment. Lars and Benjamin are both immensely experienced, and I thank them for supplying their invaluable know-how and for the many joyful hours we shared both in and outside the lab.

Lauge Christensen has been an authoritative source of general understanding and specific knowledge of the different experimental techniques used in Femtolab. During the group meetings and in the offices, he greatly facilitated inspiring and helpful discussions, which I much appreciate. The ideas leading to the development of the theory in chapter 2 were conceived in one such office discussion.

Jan Thøgersen is credited for the smooth operation of all the laser systems. Not only is he an invaluable help when laser components break, he also includes students around him in the repair work, regardless of experience, and takes time to explain the problem. I have learned much about the lasers by assisting Jan.

In addition to those already mentioned, Rasmus Ranch Johansen, Naja Villadsen, Anders Vestergaard Jørgensen, Mette Heidemann Rasmussen, James Pickering and Adam Chatterly all deserves thanks for many stimulating discussions of both science and other topics, as well as for their many achievements that are each celebrated with cake at π o' clock. Thanks for the canoe trips, Christmas lunches and the very sociable lunch- and coffee breaks.

From outside Femtolab, I would like to thank Robert Zillich for many fruitful discussions and for his helpfulness during my implementation of a simulation program based on the theory he developed.

I am grateful for discussions with Jonathan Underwood, Klaus von Haeften, Tamar Seideman, and Marius Lewerenz who also provided the HCCH-He potential that is used in my simulations.

Thanks to Mads Bøttger Hansen and Ove Christiansen for their study of the CH_3I-He potential, which unfortunately deviates too far from being cylindrically symmetric to be included in the modeling of chapter 6.

Jan Kaczmarczyk and Mikhail Lemeshko have recently looked at the experimental results presented in this thesis. Although not presented here, their angulon theory promisingly captures much of the observed dynamics. I would like to thank Jan and Mikhail for many interesting discussions about rotation of molecules in superfluid helium.

Finally, thanks to my family and friends for support. I am indebted to my wife Kathrine for her love and incredible dedication during the whole project. My life is greatly enriched by Kathrine and our kids Bjørn and Ulf.

Contents

Abstract

In this thesis, the rotation of isolated molecules and molecules solvated in superfluid helium nanodroplets is studied. The study is both theoretical and experimental. Coherent rotation of the molecules is induced by an ultrashort, linearly polarized laser pulse with a duration of about a picosecond or less. A few picoseconds after the pulse, the coherent rotation induced by the laser pulse causes the molecules to align, i. e. confining the molecular axes along axes fixed in space, though only for a short time. In this thesis, only experiments where a single molecular axis becomes confined are considered.

The established theory for laser-induced alignment of isolated molecules is reviewed. Following the review, the existing theory is extended to take into account the way most experiments are done in practice. The newly developed theory is shown to be in excellent agreement with experiments. The theory is implemented in an efficient simulation program which has been made freely available.

A new machine for conducting alignment experiments on isolated molecules and molecules solvated in superfluid helium droplets under identical laser conditions have recently been built in Femtolab. This machine is described and results of experiments performed on I_2 molecules in this machine are presented. These results show several new, never observed before alignment features for molecules in superfluid helium. Particularly, the results show coherent rotation all the way out to 600 ps or more. Furthermore, as the strength of the alignment laser is increased, the coherent rotation stops. Increasing the strength further also leads to new, never observed before alignment features. At high laser pulse strengths, fast initial dynamics emerge. The new, fast dynamics is interpreted as short-lived cavitation of the helium solvent. In the cavity, the molecule rotates freely without interacting with the helium until the cavity collapses a few picoseconds later.

The observed results are rationalized with simplified models, one based on quantum mechanics and another based on classical physics. Both of these complementary models support the interpretations of the experimental result.

The new results seem to reconcile impulsive laser induced alignment with rotationally-resolved IR spectroscopy after years of being at odds with each other.

Dansk Resumé

I denne afhandling bliver rotation af frie molekyler og molekyler opløst i superflydende helium nanodråber undersøgt. Studiet er både eksperimentelt og teoretisk. Kohærent rotation af molekylerne bliver startet af ultrakorte, lineært polariserede laser pulser ikke længere end omtrent et picosekund. Få picosekunder efter laser pulsen får den kohærente rotation molekylerne til at ensrettes. Det vil sige at akserne for hvert molekyle kommer til at pege langs de samme inertielle akser. Ensretningen ophører dog kort tid efterfølgende. Denne afhandling omhandler kun eksperimenter hvor en enkelt molekylefast akse bliver ensrettet.

Der bliver givet en kort gennemgang af den etablerede teori om laserpuls ensretning af molekyler. Efterfølgende bliver denne teori udvidet så den også beskriver den måde de fleste eksperimenter foregår på i praksis. Denne nye teori bliver eftervist eksperimentelt, og viser sig at være i særdeles god overensstemmelse med forsøgene. Teorien bliver implementeret i et effektivt simuleringsprogram som er gjort frit tilgængeligt.

En ny maskine til at udføre ensretningseksperimenter med frie molekyler og molekyler opløst i superflydende helium nanodråber under identiske laserbetingelser, er for nyligt blevet opført i Femtolab. Denne maskine bliver beskrevet, og resultater af eksperimenter med I_2 molekyler foretaget på maskinen bliver fremlagt. Disse resultater viser at iod opfører sig på en helt ny måde som aldrig før er set for molekyler i superflydende helium. Specielt viser resultaterne at kohærent rotation bliver ved helt ud til 600 ps eller længere. Hvad mere er, at nå pulsstyrken øges, så stopper den kohærente rotation. Når pulsstyrken øges yderligere observeres helt ny opførsel, som igen aldrig er set tidligere. Ved de høje laser pulsstyrker opstår der nemlig tidlig og meget hurtig dynamik. Den nye hurtige dynamik tilskrives at molekylet i dets rotation udhuler heliumdråben og derefter roterer frit, indtil hullet kollapser omkring molekylet få picosekunder senere.

De målte resultater bliver rationaliseret med simplificerede modeller. En model er baseret på kvantemekanik og en anden er baseret på klassisk fysik. Begge komplementære modeller understøtter fortolkningen af de eksperimentelle resultater.

De nye resultater ser ud til at genforene kortpuls molekylær ensretning med rotationsopløst IR spektroskopi efter flere års uoverensstemmelse.

List of Publications

The work presented in this thesis forms the basis of the following publications:

A1 Anders A. Søndergaard, Benjamin Shepperson and Henrik Stapelfeldt. "Non-adiabatic laser-induced alignment of molecules: Reconstructing $\langle \cos^2 \theta \rangle$ directly from $\langle \cos^2 \theta_{2D} \rangle$ by Fourier analysis". *Submitted to J. Chem. Phys (2016).*

A2 Benjamin Shepperson, Anders A. Søndergaard, Lars Christiansen, Jan Kaczmarczyk, Mikhail Lemeshko, Robert E. Zillich and Henrik Stapelfeldt. "Laser-induced alignment of iodine molecules in He-nanodroplets: Long-time coherence, revivals, and breaking-free". *To be submitted to Phys. Rev. Lett. (2017).*

A3 Anders A. Søndergaard, Robert E. Zillich and Henrik Stapelfeldt. "Rotational dissociation of impulsively aligned van der Waals complexes". *In preparation (working title, 2016).*

Other publications that I have contributed to:

B1 Benjamin Shepperson, Adam Chatterley, Anders Aspegren Søndergaard and Henrik Stapelfeldt. "Rotational revivals of molecules in He droplets induced by 170-ps-long alignment pulses". *In preparation (working title, 2016).*

B2 Benjamin Shepperson, Adam Chatterley, Anders Aspegren Søndergaard and Henrik Stapelfeldt. "Near-adiabatic alignment of molecules: Molecules in droplets align stronger than isolated molecules". *In preparation (working title, 2016).*

B3 Benjamin Shepperson, Anders Vestergaard Jørgensen, Anders Aspegren Søndergaard, Lars Christiansen and Henrik Stapelfeldt. "Impulsive alignment of molecules in droplets: Comparison between light and heavy rotors". *In preparation (working title, 2016).*

CHAPTER 1

Introduction

The aim of the PhD project presented in this thesis is to improve the current understanding of laser-induced alignment and rotation of molecules embedded in superfluid helium nanodroplets. In the following sections, introductions to laser-induced alignment and helium nanodroplets are given.

1.1 Laser-induced alignment

Molecules in the gas or solution phase are randomly oriented due to the stochastic nature of microscopic thermal interactions. It is, however, possible to control the rotation of molecules and to align them. Alignment refers to the confinement of molecular (polarizability) axes along laboratory fixed axes. One-dimensional (1D) alignment refers to confinement of a single molecular axis along a laboratory-fixed axis. Three-dimensional (3D) alignment refers to alignment where three linearly independent molecular axes are confined to three laboratory fixed axes. Note that if two axes are confined, the third is automatically also confined. Two-dimensional (2D) alignment is therefore equivalent with 3D alignment. Although not explored in my thesis, it is noted that for polar molecules, complete rotational control also requires orientation, where orientation refers to the molecular dipole moments pointing in a particular direction.

Among other things, alignment of molecules uniquely enables: 1) Studying the alignment-dependence of molecular reactions and light-matter interactions. 2) Performing measurements in the molecular frame of reference, thus optimizing the information content of experimental observables [1–12]. One way to align molecules is by using the moderately intense laser fields that are attainable in short and ultrashort laser pulses on the nanosecond to femtosecond time scales [5].

Alignment of molecules in this way is classified as either adiabatic or impulsive alignment. If the pulse duration τ is much longer than the rotational period of the molecule T, the alignment is adiabatic. In this case, the laser pulse forces the molecules to align with the polarization axis only for the duration of the pulse. In the opposite limit $\tau \ll T$, called impulsive alignment, the pulse induces coherent rotation of the molecules. The rotation in turn leads to alignment after the pulse is over. It is thus possible to study aligned molecules under field-free conditions. This thesis is mainly concerned with impulsive 1D alignment. The theory of laser-induced alignment of isolated molecules is described in greater detail in chapters 2 and 3.

1.2 Superfluid helium and helium nanodroplets

Another important spectroscopic technique is cryogenic matrix isolation. Exotic, short-lived species, such as molecular radicals and -ions, reactive intermediates of chemical reactions, and weakly bound van der Waals complexes can be studied by embedding the species in a cold, unreactive host material, called a matrix. Over the past two decades, helium nanodroplet spectroscopy has developed. Helium droplets consisting of 10^3-10^8 atoms have been declared the ideal spectroscopic matrix, since they are ultracold ($T = 0.37\,\mathrm{K}$), readily pick up and cool down a variety of molecules or atoms and the superfluid properties, e. g. that of vanishing viscosity, minimize the interaction between the droplet and the species of interest. Furthermore, many modern laser techniques applies unproblematically, since helium is transparent in a wide spectral range from the far IR to the UV [13–15].

Within the last five years, a main topic of the research in Femtolab at Aarhus University has been on laser-induced alignment of molecules embedded in helium nanodroplets [16–19]. A successful combination of laser-induced alignment and helium nanodroplet spectroscopy could open up for unique opportunities to study alignment dependent chemistry in this dissipative environment, as well as studying alignment of heavier, less rigid molecules e. g. of relevance in biochemistry. These molecules are otherwise difficult to isolate without breaking them apart [15]. Alignment of molecules in classical solvents is hindered by several obstacles. In a classical solvent, the molecules are not free to rotate, due to collisions with the solvent. Even if coherent rotation could be initiated by a laser pulse, the coherence, and thereby the alignment would be lost to the collisions. The intense laser pulse would also interact with the solvent and e. g. cause ionization. This would interfere with the alignment and potentially make reliable detection impossible. Most of these obstacles are absent in superfluid helium droplets.

Alignment dependent solute chemistry is not the only motivation behind the helium droplet research in Femtolab. As a macroscopic quantum system, superfluid helium is a remarkable substance with an entire research field of its own. See for example the review journal "Progress in low temperature physics". The ability to control particles in helium droplets provides new ways of probing the peculiar nature of superfluid helium [20]. Rotating molecules inside helium droplets may

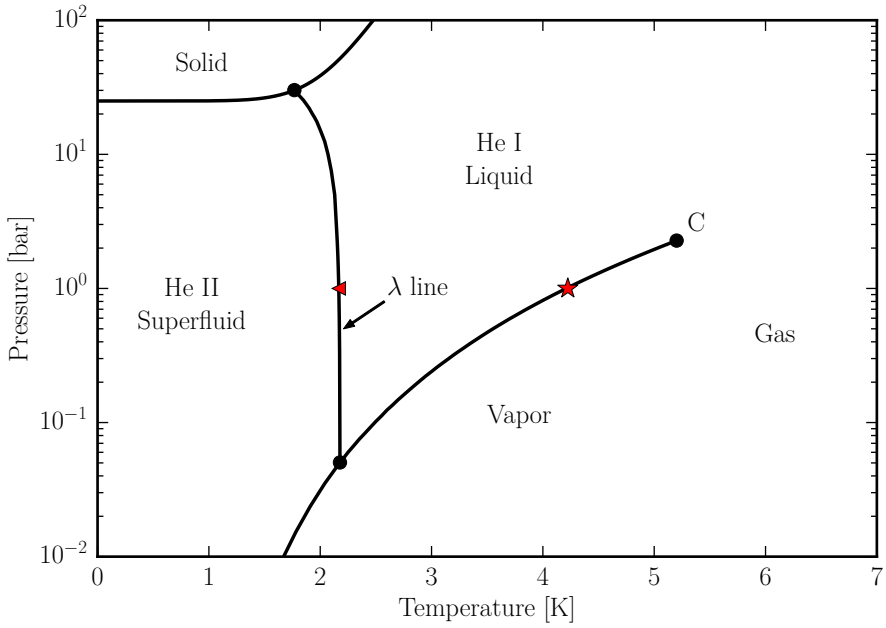

FIG. 1.1: The pressure-temperature phase diagram of ^{4}He. The red star and triangle marks the boiling point (4.22 K) and λ-transition point (2.17 K), respectively, of helium at atmospheric pressure. The critical point C is at 5.2 K and 2.3 bar. This diagram is based on data from Ref. 26.

e. g. be a way of inducing quantized vortices. These have long been known to exist in bulk superfluid helium [21, 22], but were only recently detected in large helium droplets [23–25]. Helium exists in two isotopes, the bosonic ^{4}He and fermionic ^{3}He. In this thesis, helium, or He without a superscript, refers to ^{4}He. The phase diagram of helium, shown in Fig. 1.1, exhibits two anomalous features: 1) There are two liquid phases, He I, which in most respects is a normal liquid, and He II, which is a superfluid. The λ-line separating the normal and superfluid phases is named after the shape of the heat capacity curve at the crossing of the line [27]. 2) Helium remains liquid all the way up to 25 bar even at absolute zero. These features are unique[1] to Helium and ^{3}He, although ^{3}He is first a superfluid below 3×10^{-3} K due to its fermionic nature. The liquidity down to absolute zero is attributed to the weak van der Waals interaction and the low mass of Helium and ^{3}He. As a consequence, the de Broglie wavelength exceeds the interatomic distance, and a large delocalization of the atoms ensue. No crystallization is thus possible without adding pressure [14, 29]. The superfluidity is thought to be a

[1] However, parahydrogen is a likely candidate for a new superfluid [28].

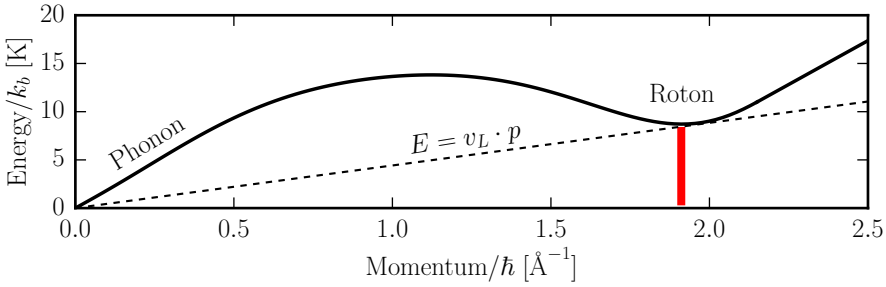

FIG. 1.2: Elementary excitation dispersion curve (fully drawn line) in bulk helium at a temperature $T = 0.4\,\mathrm{K}$ at zero pressure. The curve is based on neutron scattering data [34]. The roton gap is indicated by the red bar. The dashed line represents excitations that are allowed by momentum and energy conservation for a particle moving at the Landau velocity v_L.

consequence of Bose-Einstein condensation of the helium atoms (or cooper pairs of atoms in the case of ^{3}He) into a macroscopically occupied quantum state [22, 27, 30–32]. A detailed theory of the connection between Bose-Einsten condensation and superfluidity has not yet been firmly established, however, even after more than half a century of superfluid helium research. The relatively strong repulsive interaction between the atoms (compared to dilute Bose gasses) complicates the analysis [33]. The idea that superfluidity stems from Bose-Einstein condensation has led to a very successful two-fluid description, where superfluid helium is thought of as two interpenetrating and inseparable liquids [35, 36]. One of the liquids is the superfluid component, which is inviscid and has zero entropy. In a simplified picture, the superfluid component corresponds to the condensed helium (although really, the condensate fraction is only about 10 % even at 0 K, where the superfluid fraction is 100 %). The other, normal component is a normal liquid with conventional viscosity. The normal component carries all the entropy and thermal energy of the liquid, as it's composed of the elementary, particle-like excitations called phonons and rotons. The two-fluid model explains the fountain effect, where helium can be cooled by flowing through extremely fine pores in a porous plug. Since only the superfluid component can flow viscouslessly through the pores, the thermal energy in the normal component is left behind. A fountain can be created and sustained by heating the superleaked helium, hence the name. The two-fluid model also predicts a new heat conduction mechanism called second sound, where heat is transported as a wave instead of through diffusion [37]. This effect gives superfluid helium its extreme heat conductivity. Film flow or creep can also be understood in terms of the two-fluid model. There is a well-executed experimental demonstration video of some of the extraordinary properties of superfluid helium in Ref. 38.

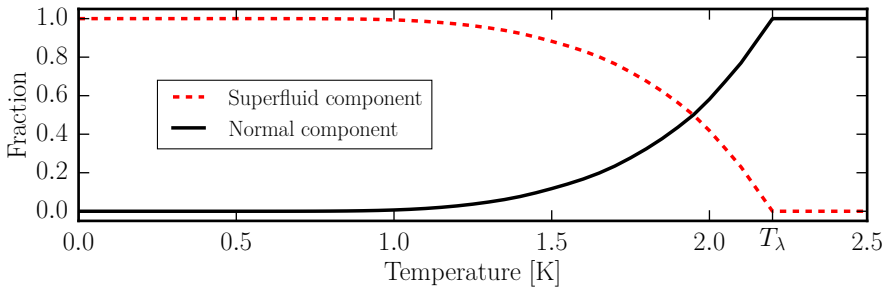

FIG. 1.3: Superfluid and normal fluid density fraction of liquid helium at low pressure and under the superfluid transition temperature T_λ. The ratio is calculated with Landau's two-fluid model on the basis of neutron scattering data [34].

The dispersion curve for bulk helium is shown in Fig. 1.2. Phonons are the excitations with a linear dispersion relation near $T = 0\,\mathrm{K}$. The slope of the phonon dispersion is the speed of sound in He II. Rotons are the excitations near the characteristic dip at the red bar. At the minimum they are the quantum mechanical analog of classic atomically small vortex, or "smoke" rings, with the inner helium moving forwards and the outer helium flowing back around it [39–42]. The low viscosity of He II can be understood as a consequence of the so-called roton gap (indicated by the red bar) in the dispersion curve of the elementary phonon and roton excitations. Together with conservation of energy E and momentum p and the nonexistence of other available excited states, the roton gap implies that objects moving with a velocity v, slower than the Landau velocity of $v_L = 58\,\mathrm{m/s}$, are unable to induce these excitations. A momentum- and energy transfer can only occur if the straight line $E = vp$ intersects the excitation curve (or if the excitation curve lies below the line in the case of a collision in more than one dimension). Thus, any object moving slower than the Landau velocity experiences no viscous drag [36, 43]. It is seen that rotons are the first states to be excited if a particle is accelerated from rest in liquid helium. The Landau velocity can be calculated as roughly $v_L \approx \Delta/p_0$, where Δ is the minimum roton energy and p_0 is the corresponding momentum. The same kind of elementary excitation spectrum is also observed in helium nanodroplets [44], and the Landau velocity has recently been demonstrated to exist in the droplets [20]. Under some circumstances, viscous drag can be experienced in bulk helium at much lower velocities, due to the creation of tangles of quantized vortices [45, 46], or even due to turbulence in the normal component [47], i. e. due to interactions with already existing excitations.

In a famous experiment, Andronikashvili [48] used an array of closely spaced, rotating discs to characterize the two-fluid behavior. The normal component of the helium follows the rotating discs adiabatically due to the viscous forces. This

effectively modifies the moment of inertia of the disc array, which is then measured. As the temperature is lowered, a classical liquid would cause an increase in the moment of inertia due to the increased viscosity and eventual solidification. However, in liquid helium, a sharp drop in the effective moment of inertia is observed as soon as the λ line is crossed (see Fig. 1.1). This is caused by the conversion from the normal component to the superfluid, inviscid component, as per Fig. 1.3. Note that below 1 K, the liquid is almost purely superfluid. In an analogous "microscopic Andronikashvili experiment" [49, 50], Grebenev *et al.* used an OCS molecule instead of a stack of discs. They measured the rotationally-resolved IR spectrum of OCS molecules in helium and ^{3}He nanodroplets. The results are shown in Fig. 1.4. The rotational spectrum for isolated OCS molecules is shown in panel a). Note the narrow lines corresponding to transitions between specific rotational states. In the ^{4}He droplets, the spectrum, shown in panel b), also consists of narrow, but slightly broader lines with linewidths of about 160 MHz. The interpretation is that the molecules can rotate freely in up to a few nanoseconds. This long lifetime of free rotation is seen as evidence of superfluidity in helium nanodroplets. A fit of the line intensities to a Boltzmann distribution gives a temperature of 0.37 K, which is consistent with previous results [51, 52]. This indicates that despite the very weak interaction with the helium, the rotational degrees of freedom equlibrate with the helium bath on a time scale that is shorter than that of the experiment [14].

The molecule attracts helium atoms stronger than helium itself does. This causes a local break-up of the superfluid in the vicinity of the molecule. The local helium atoms attach to the molecule and form a non-superfluid solvation shell that adiabatically follows the molecule in its rotation. The prominent spectral shift between panel a) and b) by about 0.6 cm^{-1} and the reduced linespacing by about a factor of 2.8 is directly attributable to the moment of inertia contributed by this solvation shell. The same effect has been demonstrated for a large variety of other molecules. The moment of inertia is typically increased by about a factor of 3 [14, 15]. Rotational spectra, such as the one in Fig. 1.4 b) are reproduced simply by adjusting the moment of inertia in a calculation for the isolated molecule.

The result of the same experiment in ^{3}He droplets, shown in panel c) is strikingly different. The ^{3}He droplets are not superfluid, since their temperature of 0.15 K is well above the superfluid transition temperature of 3×10^{-3} K. The sharp lines are absent and the rotational spectrum is significantly broadened, indicating viscous slowing of the rotation as expected from a normal liquid.

1.3 Motivation and outline

In my PhD project, I have studied laser-induced alignment of molecules in helium nanodroplets. In this thesis, I present both a theoretical description of the problem as well as a series of new experiments. The original plan was to provide an understanding of previous experiments [17, 18], that seemed at odds with spectroscopy. For example, the previous results show that the free rotation breaks

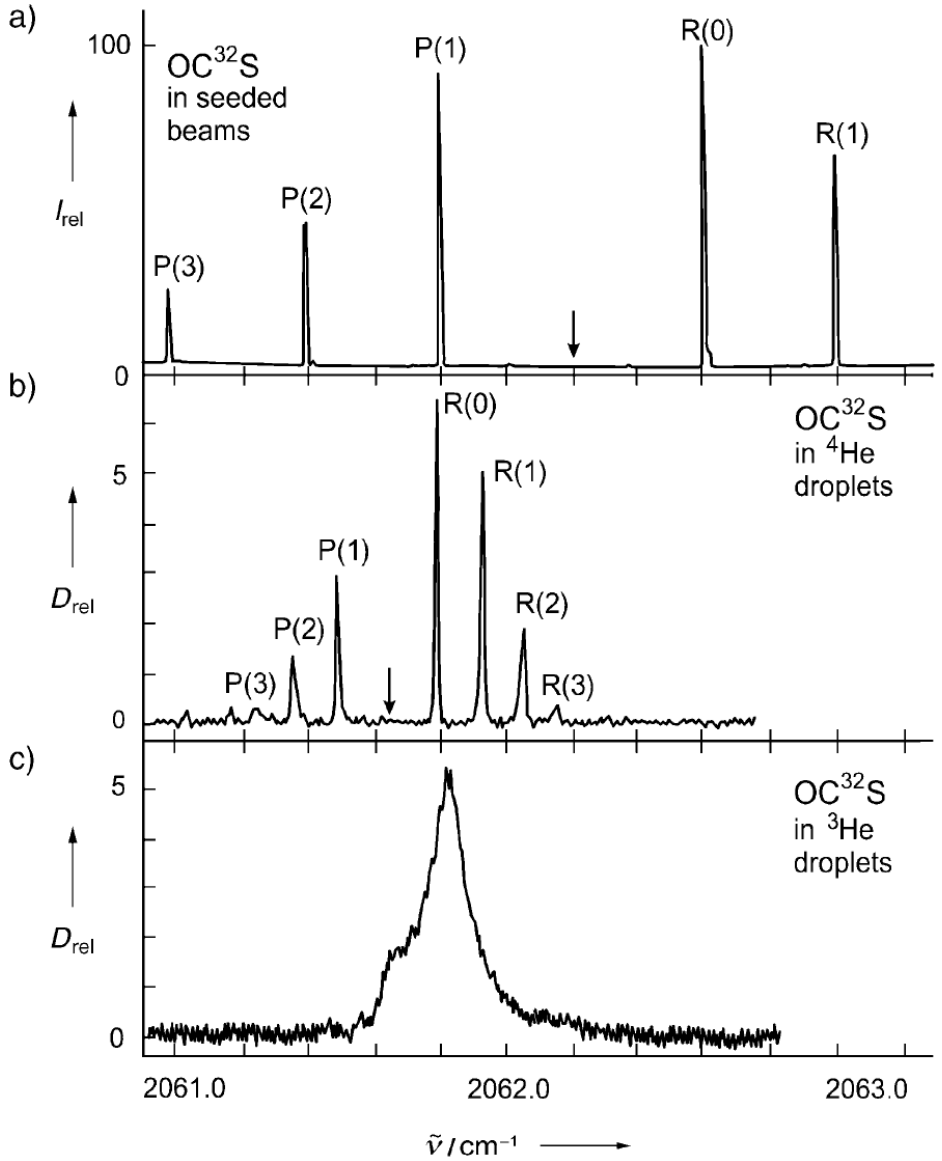

FIG. 1.4: Rotational spectrum of OCS in different cryogenic matrices: a) Isolated OCS in an Ar seeded beam, b) in ^{4}He droplets consisting of 6000 atoms, and c) in ^{3}He droplets with 1.2×10^4 atoms. The arrow in a) and b) indicates the position of the forbidden Q-branch. Excerpt from Ref. 14.

down almost immediately, and that a simple adjustment of the moment of inertia far from suffices in a description of the rotational dynamics. In the beginning of my studies, I was part of an experiment where CS_2 was aligned inside helium droplets. This experiment showed new, but just as puzzling alignment dynamics in helium: CS_2 rotates freely (and apparently without a solvation shell) for 1-2 ps before the free rotation suddenly breaks down. To understand these results, I collaborated with Robert Zillich from the Johannes Kepler University in Linz, Austria. Together, we developed a theoretical model for exploring laser-induced alignment in the presence of just a single helium atom. The model is described in chapter 6. As the modeling progressed, it slowly became clear that all of the previous alignment experiments on molecules in droplets were either done on too light molecules[2] or with laser intensities that were too high. This realization turned the direction of the research in Femtolab around from looking at increasingly smaller molecules to looking at heaver molecules using weaker alignment laser pulses. This is contrary to the normal reasoning in alignment of isolated molecules, where stronger pulses usually lead to better alignment. In chapters 4 and 5, I present new experimental results on alignment of I_2 molecules inside helium droplets. Although alignment of I_2 molecules in droplets was done earlier [18], the new experiments presented here are done with both weaker and stronger pulses. For the stronger pulses, fast dynamics similar to the case of CS_2 is observed. The major result presented here, however, is that the coherent rotation induced by the weaker pulses is so long lived ($\sim 0.6\,\mathrm{ns}$) that the dynamics again resemble free rotation, possibly with a modified moment of inertia. As I am writing this thesis, Benjamin Shepperson and Mette Rasmussen are in the lab measuring alignment of the much heaver 4,4-diiodobiphenyl ("iodine with two benzene rings in-between") inside helium droplets. Although preliminary, the very promising results already indicate rotational coherence lasting for several nanoseconds.

During the model development together with Robert Zillich, I have gained a deep understanding of the quantum mechanical description of alignment. With this understanding, I was able to resolve a long-standing issue [53] concerning a discrepancy between the experimental and theoretical characterization of alignment. I describe the theory of alignment in chapter 2, where my work on resolving this discrepancy is presented in section 2.2. Before I first met Robert, I re-implemented an alignment simulation program that was originally developed by Christer Bisgaard [54]. I re-implemented it to make it easier to use and maintain, and I made it significantly faster. Since then, I have added a graphical user interface, and as the first alignment simulation program ever, it can now simulate alignment in a way that is directly comparable to the result of an experiment. This has allowed e. g. the first determination of the droplet temperature in Femtolab by direct comparison of theoretical predictions with those obtained in an experiment (after the effects of the dropet have been deconvolved with a method developed by Lauge Christensen [55]). The program is presented in chapter 3.

[2] In the sense that the moment of inertia is too low.

CHAPTER 2

Theory of laser-induced alignment for isolated molecules

Before delving into laser-induced alignment and rotation of molecules embedded in helium nanodroplets, it is important to first understand rotation and alignment of isolated molecules. The theory of molecular alignment is therefore reviewed below in section 2.1. Historically, due to the superfluid nature of cold helium and on the basis of rotationally-resolved spectra such as those in Fig. 1.4, it was anticipated that the alignment dynamics of molecules in helium nanodroplets could be understood with this theory together with a simple re-scaling of the molecular moment of inertia. This re-scaling should account for the solvation shell that adiabatically follows a molecule in its rotation. As will be demonstrated with the experimental results presented in chapter 5, this is not the case. In chapter 6, the theory presently discussed will be expanded and used to rationalize those results.

A significant shortcoming of the established theory of alignment is that it fails to take into account the way most measurements are done in practice. The widely used observable $\cos^2\theta$, where θ is the angle between the laser polarization and the molecular axis, is actually not available in typical experiments where the measurement takes place on a 2 dimensional screen. Here, only the angle θ_{2D} is available. This angle is the angle between the laser polarization and the *projection* of the molecular axis on the 2D detector screen. I have contributed to the theory of alignment of isolated molecules by developing an efficient algorithm for calculating matrix elements and expectation values of $\cos^2\theta_{2D}$, and indeed of any other observable. The algorithm is easy to add to existing simulation programs. In my analysis of linear molecules, I have discovered how, under conditions that

are typically met in alignment experiments, $\langle\cos^2\theta\rangle$ can be reconstructed from $\langle\cos^2\theta_{2D}\rangle$ via Fourier analysis. All of this work is presented in section 2.2, and it forms the basis of a manuscript currently in preparation [A1]. The effects of only measuring the projected molecular direction has interested me since the beginning of my PhD study. But I was first provoked into developing the algorithm after an exciting discussion I had one day with Lauge Christensen and Henrik Stapelfeldt about a year ago. Lauge had been trying, with some success, to extract $\langle\cos^2\theta\rangle$ from measuring $\langle\tilde{Z}^2\rangle$, where $\tilde{Z}$ is the coordinate in the detector plane along the laser polarization (related to Z, the molecular direction coordinate along the laser polarization, $Z^2 = \cos^2\theta$. Only an uncalibrated measurement of $\langle\cos^2\theta\rangle$ is available in this way). I owe Lauge special thanks for his compelling arguments and encouragement that led me to undertake the analysis.

2.1 Quantum mechanical description

In the following, the quantum mechanical theory of molecular alignment is introduced. The focus of this thesis is on 1D alignment of linear molecules with laser pulses that are much shorter than the rotational periods of the molecules. Here, however, 1D alignment of symmetric tops is treated in general, as the descriptions of linear and symmetric tops follow the same structure. The theory for linear molecules is easily re-obtained by making the substitution $K = 0$. The simulation program described in chapter 3 would have been less useful if it could only simulate linear tops. Neither asymmetric tops, 3D alignment nor orientation will be introduced. Furthermore, the alignment is assumed to be induced by a non-resonant laser pulse. For a much more thorough introduction to the whole topic, the reader is referred to references 1, 5, 54, 56, 57.

Under the Born-Oppenheimer approximation, the Hamiltonian for a molecule can be written as a sum of a nuclear spin, an electronic, a vibrational and a rotational term, and the wave function separates into these parts. Under the rigid rotor approximation, the molecule is further assumed to have a time independent moment of inertia, e. g. by being in the vibrational ground state, or due to the fact that vibrations are much faster than rotation. Alignment is mainly concerned with the rotational part of the wave function. Only in cases where the molecule has inversion symmetry does the *parity* of the other parts of the wave function play a small, but important role that will be discussed later.

The Hamiltonian for a freely rotating, rigid, symmetric top is [58]

$$\mathcal{H}_{\text{free}} = B\mathbf{J}^2/\hbar^2 + (A - B)j_z^2/\hbar^2. \tag{2.1}$$

Here, $\mathbf{J}$ is the angular momentum of the molecule and j_z is the component of the total angular momentum along the molecular axis. For the three principal moments of inertia $I_a \leq I_b \leq I_c$ the rotational constants (in units of energy) are defined as $B = \frac{\hbar^2}{2I_b}$ and $A = \frac{\hbar^2}{2I_a}$. For an oblate top ($I_a = I_b < I_c$), $A = \frac{\hbar^2}{2I_c}$. This convention deviates from that of the cited literature, but is justified by enabling both prolate ($I_a < I_b = I_c$) and oblate tops to be handled with the exact same

computer code. For linear molecules, there is no rotation about the molecular axis, and $\mathcal{H}_{\text{free}} = B\mathbf{J}^2/\hbar^2$.

The alignment is induced by a linearly polarized, non-resonant laser field

$$\mathbf{E}(t) = E_0(t)\cos(2\pi f t)\hat{\mathbf{Z}}, \tag{2.2}$$

where $E_0(t)$ is the electric field amplitude at time t, f is the carrier frequency and $\hat{\mathbf{Z}}$ is the polarization direction. Although the specific pulse shape has no influence on a general analysis, the pulse intensity is usually assumed to be Gaussian

$$I(t) = I_0 \exp(-4\ln(2)((t-t_0)/\tau)^2). \tag{2.3}$$

The peak intensity I_0 occurs at time $t = t_0$ and the pulse duration τ is specified as the full width at half maximum. At optical frequencies, the period of oscillation (a few femtoseconds) is much shorter than the rotational period of a molecule, which is typically on the order of tens to hundreds of picoseconds or more. With a slowly varying envelope and under the dipole approximation, the interaction with any permanent dipole moment therefore averages out, and the cycle averaged molecule-laser interaction potential becomes [57]

$$V(\theta, t) = -\frac{E_0(t)^2}{4}(\Delta\alpha\cos^2\theta + \alpha_\perp). \tag{2.4}$$

Here $\Delta\alpha = \alpha_\parallel - \alpha_\perp$ is the polarizability anisotropy, and $\alpha_\parallel$ and $\alpha_\perp$ are the elements of the polarizability tensor $\underline{\underline{\alpha}}$ parallel and perpendicular to the molecular axis, respectively. It is assumed that a common frame diagonalizes both the inertia and the polarizability tensors. The term (2.4) arises because the laser induces a dipole moment $\mathbf{p} = \underline{\underline{\alpha}}\mathbf{E}(t)$ that preferentially points along the instantaneous E-field direction and thus doesn't average out. The total Hamiltonian for the rotation of the molecule is then

$$\mathcal{H} = B\mathbf{J}^2/\hbar^2 + (A-B)j_z^2/\hbar^2 - \frac{E_0(t)^2}{4}(\Delta\alpha\cos^2\theta + \alpha_\perp). \tag{2.5}$$

Certain limiting cases of alignment can be understood with classical mechanics. Classically, the laser exerts a torque τ on the each of the molecules in an ensemble of initially slowly rotating molecules through the induced dipole interaction (2.4). The torque is conveniently derived from the Euler-Lagrange equation. The (2D) Lagrangian is

$$\mathcal{L}(\theta, \omega, t) = \frac{1}{2}I\omega^2 - V(\theta, t), \tag{2.6}$$

where $\omega = \dot{\theta}$ and I is the (scalar) moment of inertia. The torque

$$\tau(t) = \frac{d}{dt}I\omega = \frac{d}{dt}\left(\frac{\partial\mathcal{L}}{\partial\omega}\right) = \frac{\partial\mathcal{L}}{\partial\theta} = -\frac{\partial V(\theta,t)}{\partial\theta} = \Delta\alpha\frac{E_0(t)^2}{4}\sin(2\theta), \tag{2.7}$$

is at a given time maximal when $\theta = 45°$, and it forces the molecules to align along the laser polarization at $\theta = 0$. In the *impulsive*, low temperature limit,

classical mechanics accurately describes the early alignment dynamics [59–61]. Impulsive alignment means that the pulse is short enough that the molecules don't move for the duration of the pulse. To the extent that $\sin(2\theta) \approx 2\theta$ is a good approximation, the torque, and thereby the gained angular velocity, is proportional to the angular displacement. Molecules initially at rest will therefore align at the same instant of time, shortly after the pulse. Better alignment can be achieved if the molecules are somehow pre-aligned, such that the approximation is good for all molecules. This type of alignment is attractive, because it occurs in the absence of an external field. It is also the focus of this thesis. In the long pulse limit, the adiabatically increasing torque will guide the molecules into an angular trapping potential, causing the molecules to undergo librating motion about the polarization axis [1, 5, 56]. Typically, higher degrees of alignment are achieved in this regime.

In the language of quantum mechanics, alignment of a molecule means localizing the direction of the molecular axis. A prerequisite for obtaining good alignment is therefore a large uncertainty in the angular momentum of the molecule. In other words, good alignment requires a large superposition of angular momentum states. To show how the laser induces this broad superposition, the rotational wave function is first expanded in the angular momentum basis, which coincides with the field free $V = 0$ stationary states

$$|\Psi_{KM}(t)\rangle = \sum_J C^J_{KM}(t)|JKM\rangle. \tag{2.8}$$

Here, J is the angular momentum quantum number, and K and M are the quanta of the projection of the angular momentum on the z and Z axes, respectively. Summation over K and M has been omitted, because even during the pulse, both K and M are conserved. The spatial representation of each $|JKM\rangle$ ket is

$$\langle\varphi,\theta,\chi|JKM\rangle = (-1)^{M-K}\sqrt{\frac{2J+1}{8\pi^2}}\mathscr{D}^J_{-M,-K}(\varphi,\theta,\chi), \tag{2.9}$$

where $\mathscr{D}^J_{M,K}$ is a matrix element of the Wigner $\mathscr{D}^J$ matrix. The Euler angles φ, θ and χ describe the rotation from the laboratory (space fixed) XYZ frame to the body fixed xyz molecular frame. The angles θ and φ are the polar and azimuthal angles of the molecular axis, respectively, and χ is the angle of rotation around the molecular axis. In the case of a linear rotor, $K = 0$ and the Wigner matrices reduce to the well-known spherical harmonics [58]

$$\langle\theta,\varphi|JM\rangle = Y_{JM}(\theta,\varphi) = \sqrt{\frac{2J+1}{4\pi}}\mathscr{D}^J_{-M,0}(\varphi,\theta,\chi). \tag{2.10}$$

Inserting the expansion (2.8) in the Schrödinger equation and projecting onto a particular $|JKM\rangle$ state yields a coupled system of linear ordinary differential equations for the expansion coefficients C^J_{KM} [2, 54]

$$i\hbar\frac{\partial}{\partial t}C^J_{KM} = H^J_K C^J_{KM} + \sum_{J'} C^{J'}_{KM}\langle JKM|V(\theta,t)|J'KM\rangle, \tag{2.11}$$

where

$$H_K^J = BJ(J+1) + (A-B)K^2 \tag{2.12}$$

is the energy eigenvalue of the $|JKM\rangle$ state and

$$\langle J'K'M'|V(\theta,t)|JKM\rangle = -\frac{E_0^2(t)}{4}\left(\Delta\alpha\langle J'K'M'|\cos^2\theta|JKM\rangle + \alpha_\perp\delta_{J'J}\delta_{K'K}\delta_{M'M}\right) \tag{2.13}$$

are the matrix elements of the interaction potential. A neat trick [54] for obtaining the matrix elements of $\cos^2\theta$ involves the Gaunt coefficient [58]

$$\int \mathscr{D}^{J''}_{M'',K''}(\Omega)\mathscr{D}^{J'}_{M',K'}(\Omega)\mathscr{D}^{J}_{M,K}(\Omega)d\Omega = 8\pi^2 \begin{pmatrix} J & J' & J'' \\ K & K' & K'' \end{pmatrix}\begin{pmatrix} J & J' & J'' \\ M & M' & M'' \end{pmatrix}. \tag{2.14}$$

Here $\Omega = \varphi, \theta, \chi$ and $d\Omega = \sin\theta\, d\theta\, d\varphi\, d\chi$. By inserting

$$\cos^2\theta = \tfrac{2}{3}\mathscr{D}^2_{0,0}(\theta) + \tfrac{1}{3}, \tag{2.15}$$

a formula for the matrix elements emerges

$$\begin{aligned}&\langle J'K'M'|\cos^2\theta|JKM\rangle = \\ &(-1)^{M-K}\frac{2}{3}\sqrt{(2J+1)(2J'+1)}\begin{pmatrix} J & J' & 2 \\ K & -K' & 0 \end{pmatrix}\begin{pmatrix} J & J' & 2 \\ M & -M' & 0 \end{pmatrix} \\ &+\frac{1}{3}\delta_{J'J}\delta_{K'K}\delta_{M'M}.\end{aligned} \tag{2.16}$$

As asserted above, the selection rules for the 3j-symbols[1] in (2.16) implies that K and M are uncoupled, i.e.

$$\langle J'K'M'|\cos^2\theta|JKM\rangle \propto \delta_{K'K}\delta_{M'M}. \tag{2.17}$$

Furthermore, only transitions with $\Delta J = 0, \pm 1, \pm 2$ are allowed. For linear molecules $K = 0$ only $\Delta J = 0, \pm 2$ transitions are allowed.

Armed with these selection rules, the coupled equations (2.11) for the expansion coefficients in the angular momentum basis can now be understood qualitatively. First, when the laser is off, $V = 0$ and the equations are not coupled at all. Their solutions are simply those of stationary states in general, i. e. complex phase factors $C^J_{KM}(t) = \exp(-iH^J_K(t-t_0)/\hbar)C^J_{KM}(t_0)$ with an angular frequency of $\omega = H^J_K/\hbar$ that increases quadratically with the angular momentum quantum number. Suppose now that the system starts out with all population in the ground state $C^0_{00} = 1$. For a linear molecule, when the laser is turned on, in the first small time step dt, some population will be transferred to the $|200\rangle$ state. The amount depends on the strength of the laser field. In the next small

[1] The 3j-symbols are proportional to the Clebsch-Gordan coefficients but obey more symmetry rules. For an excellent introduction to the topic, see the book of Zare [58].

time step, more population will be transferred to the $|200\rangle$ state from the ground state. However, some of the population in the $|200\rangle$ state will transfer back to the ground state (with approximately the opposite sign if the time step is short enough due to the two factors of $-i$ involved), and some will transfer up to the next excited state $|400\rangle$. This chain of population transfers continues forming a broader and broader angular momentum wave packet. Finally the phase evolution of the highest populated states become so fast, that contributions from lower states tend to average out. This balance between the coupling strength (proportional to laser intensity) and phase evolution (proportional to state energy) determines how broad the wave packet can become. Note that this is what could be expected even without knowing the coupled equations (2.11). The width of the induced wave packet should depend on the energy that the laser is able to pump into the rotation. Even though a broad wave packet is necessary, it is not sufficient for alignment. The relative phases of the expansion coefficients must lead to a collective maximum in the degree of alignment $\langle \cos^2\theta \rangle$ for alignment to occur. In section 2.2.2, it will among other things be shown how the phases imprinted by a δ kick [59–61] causes the alignemt trace $\langle \cos^2\theta \rangle(t)$ to become a sum of sines.

The quantum mechanical theory above generally predicts the alignment dynamics accurately. However, it is interesting to revisit the adiabatic limit mentioned above, where the pulses are long and where the alignment at the peak of the pulse is of main interest. In this regime, the adiabatic theorem of quantum mechanics implies that the field free stationary states adiabatically turn into the corresponding eigenstates of the full Hamiltonian (2.5), known as pendular states, and back to the original states (up to a geometrical phase [62]) after the pulse. A simpler theory of alignment in this regime is based on the time independent Schrödinger equation at the peak of the alignment pulse [1, 5, 54, 56, 57]. In molecular alignment, a distinction is made between adiabatic and nonadiabatic[2] alignment. Nonadiabatic alignment simply refers to a situation that is not adiabatic, but it is often used interchangeably with impulsive alignment, which is the opposite limit of adiabatic alignment. The alignment dynamics in the two limits are quite dissimilar. This thesis is primarily concerned with impulsive alignment.

2.2 Characterizing alignment: $\langle \cos^2\theta \rangle$ vs $\langle \cos^2\theta_{\mathbf{2D}} \rangle$

The degree of alignment is characterized by $\langle \cos^2\theta \rangle$. Coincidentally, the molecule-laser interaction potential (2.4) involves a factor $\cos^2\theta$, so the matrix elements of $\cos^2\theta$ are already available from (2.16). Given the state vector $|\Psi(t)\rangle$ expressed as expansion coefficients, it is then a simple matter to evaluate the degree of alignment as the vector-matrix-vector product

$$\left\langle \cos^2\theta \right\rangle(t) = \langle \Psi(t)| \cos^2\theta |\Psi(t)\rangle. \tag{2.18}$$

[2]Strictly, diabatic is the antonym of adiabatic. Perhaps nonadiabatic won because the pronunciations are too similar.

Experimentally, as will be seen in chapters 4-5, the degree of alignment is characterized by Coulomb exploding the molecules. An intense femtosecond laser pulse multiply ionizes the molecules and the emission directions of the recoiling ionized fragments are recorded with a velocity map imaging (VMI) spectrometer. In the VMI, the charged fragments are accelerated by the electric field between two capacitor plates onto a 2 dimensional (2D) micro-channel plate detector in front of a phosphor screen. The situation is summarized in Figure 2.1. As is evident from the figure, in the experiment, the degree of alignment is not characterized by $\langle\cos^2\theta\rangle$, but by $\langle\cos^2\theta_{2D}\rangle$, i. e. by the same expectation value but for the projected molecular angle instead. Under some conditions, it is possible to invert the measured 2D angular distribution to its 3D counterpart by employing what is known as an Abel inversion [63]. In this way, $\langle\cos^2\theta\rangle$ can be measured experimentally. The main drawback with the Abel inversion technique is that it requires high statistics (i. e. a large number of detected ions) to be feasible. This limits the practical applicability of the method to usually only inverting a few selected times in a recorded 2D alignment trace $\langle\cos^2\theta_{2D}\rangle(t)$.

Here, an alternative approach is proposed. Instead of inverting a 2D measurement, the 2D result is calculated for direct comparison with the experiment. This requires some extension of the theory, but as will be shown in section 2.2.3, it also leads to a new and much more efficient method for inverting recorded 2D alignment traces. That method is efficient because it works directly on a recorded 2D trace, and thus avoids working with distributions altogether.

The coordinate system chosen above is such that the Euler angles θ and φ can be identified as the standard polar and azimuthal spherical coordinates of the molecular z-axis, respectively. In the lab frame XYZ, the unit vector pointing along z is therefore $\hat{\mathbf{z}} = (\sin\theta\cos\varphi, \sin\theta\sin\varphi, \cos\theta)$. In the experiments, the alignment laser polarization is always in the plane of the detector. In a plane perpendicular to the polarization, the ion images have cylindrical symmetry due to the linear laser pulse, and will not show the alignment. For concreteness, therefore, but without loss of generality, the plane of the detector is taken to be parallel to the $X = 0$ plane. The angle θ_{2D} is between the $\hat{\mathbf{Z}}$ direction and the projection $\mathbf{z}_{2D} = (0, \sin\theta\sin\varphi, \cos\theta)$. From the dot product $\cos\theta = \hat{\mathbf{Z}} \cdot \mathbf{z}_{2D} = ||\hat{\mathbf{Z}}||\,||\mathbf{z}_{2D}||\cos\theta_{2D}$ it is seen that

$$\cos^2\theta_{2D} = \frac{\cos^2\theta}{\cos^2\theta + \sin^2\theta\sin^2\varphi}. \tag{2.19}$$

Having the detector parallel to the $Y = 0$ plane means replacing $\sin^2\varphi$ with $\cos^2\varphi$ in (2.19). However, choosing either plane, or indeed any plane containing the Z axis, leads to the same matrix elements. As will be shown below, the cylindrical symmetry causes any φ dependence to be integrated out. The choice of plane will matter, though, if the laser pulse is not linearly polarized. It is apparent that $\cos^2\theta_{2D} \geq \cos^2\theta$ since $||\mathbf{z}_{2D}|| \leq 1$. A 2D alignment measurement will therefore always overestimate the actual degree of alignment.

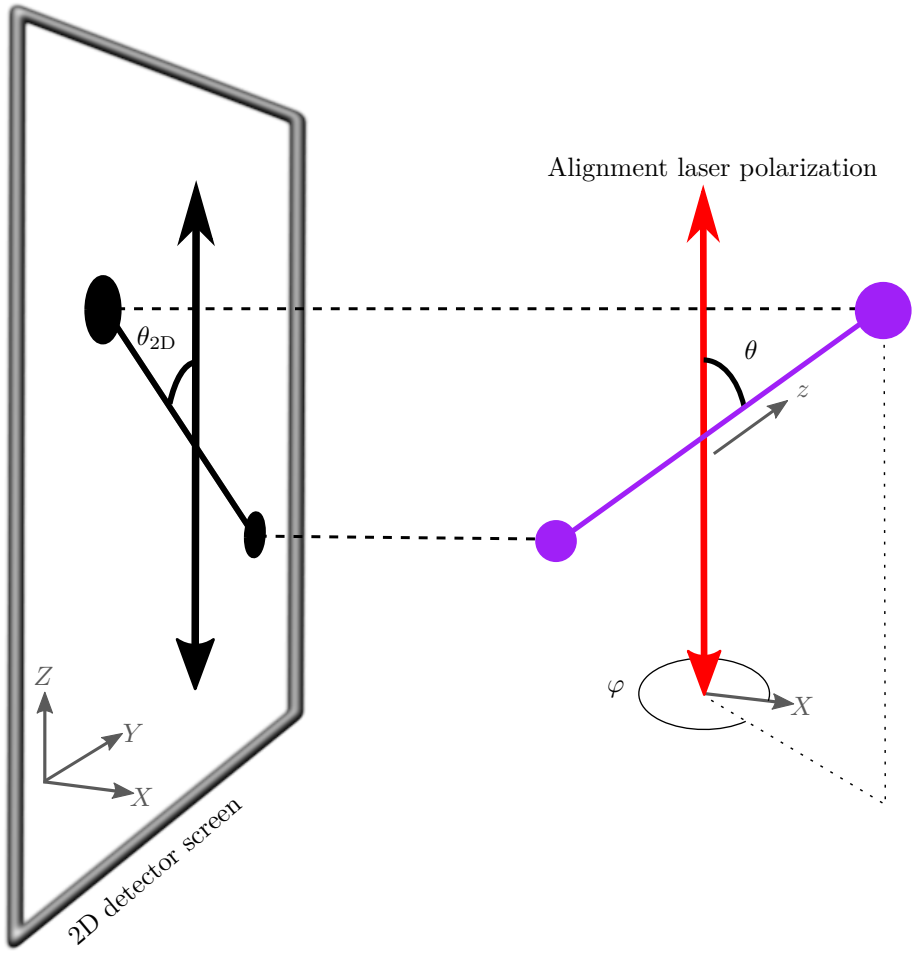

FIG. 2.1: The coordinate system. The detector screen spans the laboratory fixed ZY plane. The linear molecule is aligned by a linear laser pulse, polarized along the Z axis. The polar and azimuthal angles θ and φ parameterize the orientation of the molecule fixed z axis with respect to the laboratory fixed coordinate system XYZ. The measurement projects the polar angle θ into the polar angle θ_{2D} in the detector plane.

2.2.1 Matrix elements

Given the matrix elements of $\cos^2\theta_{2D}$, it is again a simple matter of calculating a vector-matrix-vector product to obtain the 2D degree of alignment

$$\left\langle\cos^2\theta_{2D}\right\rangle(t) = \langle\Psi(t)|\cos^2\theta_{2D}|\Psi(t)\rangle. \tag{2.20}$$

In a similar way as for the matrix elements of $\langle\cos^2\theta\rangle$, the matrix elements of *any* observable $\mathcal{O}(\varphi,\theta,\chi)$ can be calculated efficiently by expanding $\mathcal{O}$ in the $|JKM\rangle$ basis,

$$\begin{aligned}\mathcal{O}(\Omega) &= \sum_{JKM} a^J_{M,K}\langle\Omega|JKM\rangle \\ &= \sum_{JKM} a^J_{M,K}(-1)^{M-K}\sqrt{\frac{2J+1}{8\pi^2}}\mathscr{D}^J_{-M,-K}(\Omega)\end{aligned} \tag{2.21}$$

and using the Gaunt coefficient trick on each of the terms in the expansion. The expansion coefficients are

$$a^J_{M,K} = \sqrt{\frac{2J+1}{8\pi^2}}\int \mathscr{D}^J_{M,K}(\Omega)\mathcal{O}(\Omega)d\Omega. \tag{2.22}$$

Inserting the expansion (2.21) into the matrix element bracket $\langle\mathcal{O}\rangle$ and applying equations (2.9) and (2.14) yields[3]

$$\begin{aligned}&\langle J'K'M'|\mathcal{O}|JKM\rangle = (-1)^{M-K}\sqrt{(2J+1)(2J'+1)}\times \\ &\sum_{J''K''M''}(-1)^{M''-K''}a^{J''}_{M'',K''}\sqrt{\frac{2J''+1}{8\pi^2}}\begin{pmatrix} J & J' & J'' \\ -K & K' & -K''\end{pmatrix}\begin{pmatrix} J & J' & J'' \\ -M & M' & -M''\end{pmatrix}.\end{aligned} \tag{2.23}$$

The matrix elements $\langle J'K'M'|\mathcal{O}|JKM\rangle$ for $K\neq K'$ or $M\neq M'$ are not in general zero, as is the case with $\langle J'K'M'|\cos^2\theta|JKM\rangle \propto \delta_{K'K}\delta_{M'M}$. However, it is always true that $\langle J'K'M'|\cos^2\theta_{2D}|JKM\rangle \propto \delta_{K',K}$, since Wigner matrices with different K have zero overlap, and the angle θ_{2D} does not depend on χ (any projection of the vector $\hat{\mathbf{z}} = (\sin\theta\cos\varphi, \sin\theta\sin\varphi, \cos\theta)$ onto a space fixed plane does not involve χ. Physically, any vector is unchanged by a rotation about an axis along the vector). The χ dependence of a Wigner matrix is contained in a separate factor, so anything that does not depend on χ cannot change the proportionality of a bracket with $\delta_{K'K}$. Furthermore, as noted above, a linear laser pulse never changes K or M. A good anzats for simulation purposes is that the initial state or ensemble member is stationary[4] $|\Psi_{KM}\rangle_0 = |JKM\rangle$ with a definite K and M. Expansion coefficients $C^{J'}_{K'M'}$ with $K\neq K'$ or $M\neq M'$ are

[3] A more detailed derivation can be found in appendix A.1.

[4] Random phases in the initial superposition would add incoherently in an ensemble anyway.

therefore always zero. The expectation value is then

$$\begin{aligned}\langle\Psi_{KM}(t)|\mathcal{O}|\Psi_{KM}(t)\rangle &= \sum_{J'JK'KM'M} \overline{C^{J'}_{K'M'}(t)} C^{J}_{KM}(t)\langle J'K'M'|\mathcal{O}|JKM\rangle \\ &= \sum_{J'J} \overline{C^{J'}_{KM}(t)} C^{J}_{KM}(t)\mathcal{O}^{J'}_{JKM}. \end{aligned} \tag{2.24}$$

Regardless of the values of the observable matrix elements, only those with the K and M values of the initial state will matter, because the rest end up being multiplied with expansion coefficients that are all zero[5]. Only the matrix elements

$$\mathcal{O}^{J'}_{JKM} = \langle J'KM|\mathcal{O}|JKM\rangle \tag{2.25}$$

survive. These observations significantly reduce the number of matrix elements that must be calculated and stored.

By inserting $K' = K$ and $M' = M$ in (2.23) and using the symmetry properties of the 3j symbols, an expression for $\mathcal{O}^{J'}_{JKM}$ is obtained

$$\begin{aligned}\mathcal{O}^{J'}_{JKM} = &\frac{(-1)^{(M-K)}}{4\pi^{3/2}}\sqrt{(2J+1)(2J'+1)} \\ &\times \sum_{J''} a_{J''}\sqrt{2J''+1}\begin{pmatrix} J & J' & J'' \\ -K & K & 0 \end{pmatrix}\begin{pmatrix} J & J' & J'' \\ -M & M & 0 \end{pmatrix}. \end{aligned} \tag{2.26}$$

Here, the reduced expansion coefficient a_J is introduced as

$$a_J \equiv \sqrt{2\pi}\cdot a^J_{0,0} \tag{2.27}$$

$$= \sqrt{\frac{2J+1}{4\pi}}\int P_J(\cos\theta)\mathcal{O}(\Omega)d\Omega \tag{2.28}$$

$$= \sqrt{\frac{2J+1}{4\pi}}\int_{-1}^{1} du P_J(u)\int_0^{2\pi} d\varphi \int_0^{2\pi} d\chi\ \mathcal{O}(\varphi,u,\chi) \tag{2.29}$$

i. e. a_J is the expansion coefficient in Legendre polynomials $P_J(u)$ of $\mathcal{O}$, where the χ and φ dependence has been integrated out. The normalization is chosen such that the Legendre polynomials can be identified as the spherical harmonics $Y_{J0}(\theta,\varphi)$, which are more stable to evaluate numerically. In the last line (2.29), the substitution $u = \cos\theta$, $du = -\sin\theta d\theta$ has been inserted. Due to the symmetry properties of the 3j symbols, the sum over J'', M'' and K'' in (2.23) collapses into a sum only over J'' where $K'' = K - K'$ and $M'' = M - M'$. For the case of a linearly polarized pulse, then, only the terms with $M'' = K'' = 0$ need to be evaluated. In numerical simulations, the infinite $|JKM\rangle$ basis is truncated at some maximal $J = J_{\max}$. Due to the $J'' \leq J + J'$ selection rule of (2.26), only the expansion coefficients up to $J = 2J_{\max}$ are then required in a simulation. Remarkably, the symmetry of the laser interaction makes it unnecessary to know the entire observable in order to calculate its expectation value. Only a small set

J	$\mathcal{O}=\cos^2\theta$	$\mathcal{O}=\cos^2\theta_{2D}$
0	1/3	$5.000\,000\,000\,000\times10^{-1}$
2	2/3	$6.250\,000\,000\,000\times10^{-1}$
4		$-1.875\,000\,000\,000\times10^{-1}$
6		$1.015\,625\,000\,000\times10^{-1}$
8		$-6.640\,625\,000\,000\times10^{-2}$
10		$4.785\,156\,250\,000\times10^{-2}$
12		$-3.662\,109\,375\,000\times10^{-2}$
14		$2.920\,532\,226\,563\times10^{-2}$
16		$-2.400\,207\,519\,531\times10^{-2}$
18		$2.018\,356\,323\,242\times10^{-2}$

Table 2.1: First 10 nonzero reduced expansion coefficients a_J, each multiplied with $\sqrt{2J+1}/4\pi^{3/2}$, for the observables $\mathcal{O}=\cos^2\theta$ and $\mathcal{O}=\cos^2\theta_{2D}$ (see text). For odd J, $a_J=0$.

of its reduced expansion coefficients are required. In particular, it is not necessary to know which plane the detector is in for the case of $\mathcal{O}=\cos^2\theta_{2D}$.

The numerical evaluation of the integral (2.29) together with the evaluation of the 3j symbols in (2.26) is easily more than 1000-fold less computationally demanding than naively evaluating $\langle J'KM|\mathcal{O}|JKM\rangle$ through its definition as a triple-integral over 2 Wigner $\mathscr{D}$ matrices and $\mathcal{O}$. The same set of $2J_{\max}$ reduced expansion coefficients is used for all the matrix elements, whereas the direct application of the definition requires evaluating a new triple-integral for each of the roughly $J_{\max}^2\times M_{\max}\times K_{\max}$ required matrix elements. The definition also involves an integrand consisting of two associated Legendre polynomials P_J^M and $P_{J'}^M$ even when $K=0$, instead of just one as in (2.29). Not only does this lead directly to further costly evaluations of Legendre polynomials, but the more complicated integrands require more evaluations for the same quadrature accuracy.

The reduced expansion coefficients a_J are calculated with the adaptive 61 point Gauss-Kronrod quadrature rule from GSL [64] with absolute and relative error tolerances set to 10^{-13}. This allows numerical errors in at most 3 of the least significant digits out of the (roughly) 16 available in double precision. For comparable accuracy, the trapezoidal and Gauss-Legendre quadrature rules are found to be infeasible. For $\mathcal{O}=\cos^2\theta_{2D}$, the evaluation of all the reduced expansion coefficients a_J up to $J=100$ takes about 170 ms on a normal laptop computer. This is more than 10 times slower than solving the Schrödinger equation (2.11). However, it must only be done once. The Schrödinger equation must be solved for each ensemble member and for each focal volume intensity shell, as detailed in section 3.2. The 10 most significant reduced expansion coefficients of

[5] This seems like an elaborate way of stating $0\cdot X=0$. But the 0's can be hard to recognize.

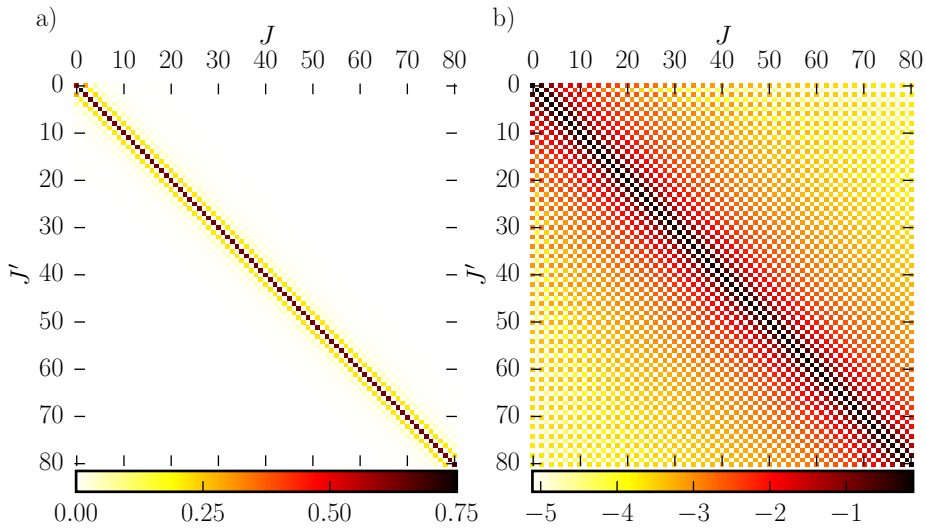

FIG. 2.2: Graphical matrix representation of $\langle J'00|\cos^2\theta_{2D}|J00\rangle$ for J up to 80. In the left panel, the absolute value of each matrix element is plotted. In the right panel, the base 10 logarithm of the absolute value of each element is plotted.

$\cos^2\theta$ and $\cos^2\theta_{2D}$ are listed in table 2.1. Here, they are each multiplied with a normalization factor $N_J = \sqrt{2J+1}/4\pi^{3/2}$, such that[6]

$$\langle\mathcal{O}\rangle = \left\langle \sum_J N_J a_J \mathscr{D}^J_{0,0} \right\rangle . \tag{2.30}$$

The middle column is thus a direct consequence of equation (2.15). As the 3j symbol with all zeros evaluates to 1, it is easy to verify by inserting the first row of the table into equation (2.26), that the implementation calculates $\langle 000|\cos^2\theta_{2D}|000\rangle = 0.5 \pm 10^{-14}$. This is in agreement with the expectation that a randomly oriented molecule has $\langle\cos^2\theta_{2D}\rangle = 1/2$. Similarly, $\langle 000|\cos^2\theta|000\rangle = 1/3$. The coefficients for odd J are all zero because $\cos^2\theta_{2D}$ is even. When the bottom row of a 3j symbol is all 0's, the sum of the top row must be even. Thus whenever $M = 0$ or $K = 0$, the odd bands in the matrix representation $\mathcal{O}^{(J+2n+1)}_{JKM}$ are all zero, since j'' must then be even in (2.26).

The textbook formulas for 3j symbols suffer from catastrophic cancellation and are numerically unstable [58, 65]. On the finite precision arithmetic implemented in modern CPUs (IEEE 754 double-precision), they fail even for moderately large quantum numbers. In this thesis, the 3j symbols are evaluated accurately and efficiently using the J recursion relation from reference 66. The Fortran 77 routine

[6] This does not mean that $\mathcal{O} = \sum_J N_J a_J \mathscr{D}^J_{0,0}$!

`drc3jj` for the evaluation of the recursion relation was downloaded from reference 67, and appears to have the same authors as reference 66. It is noted that a newer, simplified technique for calculating 3j symbols exactly [68] and an efficient storage scheme based on Regge symmetry [69] is available. However, pre-calculating the $\mathcal{O}$ matrix representation takes at most a few seconds, even for larger molecules, and only ever has to be done once, so these improved methods are not explored.

The $|J - J'| \leq J'' \leq J + J'$ selection rule helps visualizing the matrix representation (2.26) of $\mathcal{O}$. The diagonal $J = J'$ contains contributions from all the reduced expansion coefficients $a_{J''}$. The n'th bands with $|\Delta J| = |J - J'| = n$ contains contributions from all but the n first reduced expansion coefficients. If $a_{J''}$ is negligible for $J'' > J_{\text{thr}}$, where J_{thr} is some threshold J value, then only the last expansion coefficient $a_{J_{\text{thr}}}$ contributes the J_{thr}'th band, and all higher bands $|\Delta J| > J_{\text{thr}}$ are negligible. As can be seen from table 2.1, the coefficients a_J for $\cos^2\theta_{2D}$ quickly falls off. As expected, the bands in the matrix representation of $\cos^2\theta_{2D}$, shown in Fig. 2.2, therefore quickly diminish in magnitude away from the diagonal. As a good approximation, $\cos^2\theta_{2D}$ obeys the selection rule $\Delta J = 0, \pm 2, \pm 4$ for $K = 0$.

Remarkably, the matrix elements in each band seem to converge quickly as J increases. This is in fact a general feature of the matrix elements $\mathcal{O}^{J+\Delta J}_{JKM}$ for different K and M. For fixed J'' and M'', as $J, J' \to \infty$ with fixed $J' - J = \Delta J$ and $J' - |M'| \to \infty$, the asymptotic formula [70]

$$\sqrt{J + J' + J'' + 1} \begin{pmatrix} J & J' & J'' \\ M & M' & M'' \end{pmatrix} \to (-1)^{J''-J-M'} d^{J''}_{\Delta J, -M''}(\xi) \qquad (2.31)$$

relates the 3j symbols to the reduced Wigner rotation matrices $d^J_{M,K}(\xi)$. Here, $\cos\xi = \frac{M'}{J'+1/2} \to 0$. The argument to the Wigner matrix converges. Therefore, the Wigner matrix also converges. Using (2.31) twice it can be seen that the matrix elements $\mathcal{O}^{J+\Delta J}_{JKM}$ in (2.26) converge as $J \to \infty$. Earlier, this convergence was proven for $\mathcal{O} = \cos^2\theta$ by e. g. Seideman [2] and in the thesis of Bisgaard [54]. Their argumentation is worth revisiting and generalizing. Assuming that the reduced expansion coefficients a_J are all zero for $J > 2$, as is the case for $\cos^2\theta$, the leading order term of the matrix elements (2.26) scale as J^0, J^{-2} and J^0 for $\Delta J = 0, 1, 2$, respectively. This can be seen by inserting the analytical expressions for 3j symbols found in table 2.5 in Zare [58]. The most important of these expressions are also given in the equations (3.1)-(3.4) below. So e. g. for $\mathcal{O} = \cos^2\theta$ the $\Delta J = 0, \pm 2$ bands converge to a nonzero value, and the $\Delta J = \pm 1$ bands converge to zero.

The general case of evaluating $\langle\cos^2\theta_{2D}\rangle$ for an asymmetric top has still not been rigorously analyzed. However, an asymmetric top wave function is just a linear combination of symmetric top basis functions, only where K is no longer a good quantum number [58]. It is conceivable that the matrix elements in (2.23) are already sufficiently well determined to be useful in a calculation for an asymmetric top, and e. g. only a change of basis is required. In the thesis of Christer Bisgaard [54], the asymmetric top wave function is propagated in the

eigenstates of the Hamiltonian after the pulse, and transformed back into the $|JKM\rangle$ basis whenever an expectation value must be calculated.

To summarize, the matrix elements, and thereby the expectation value of an observable, e. g. $\cos^2\theta_{2D}$, can be evaluated efficiently with the following algorithm:

1. Choose a suitable basis size with a maximum J quantum number J_{max}.

2. Evaluate the first $2J_{max}$ reduced expansion coefficients a_J numerically with equation (2.29). The adaptive 61 point Gauss-Kronrod quadrature rule is highly suited for this task. For calculating $\langle\cos^2\theta_{2D}\rangle$ only the first a_J are required if high order bands in the matrix representation are neglected.

3. For each fixed K and M quantum number required, evaluate and store the matrix elements $\mathcal{O}^{J'}_{JKM}$ with formula (2.26). Care should be taken when evaluating the 3j symbols, since common formulae are numerically unstable.

4. Whenever an expectation value is required, evaluate it with equation (2.24).

2.2.2 Explorative spectral analysis of alignment traces

In this and the following section, the Fourier spectra of $\langle\cos^2\theta_{2D}\rangle$ and $\langle\cos^2\theta\rangle$ are analyzed. Among other things, this leads to a better qualitative understanding of alignment dynamics in general than in the preceding discussion. Most, if not all results concerning $\langle\cos^2\theta\rangle$ are already well-known. I do the derivation from the beginning anyway to highlight the similarities and differences between $\langle\cos^2\theta_{2D}\rangle$ and $\langle\cos^2\theta\rangle$.

Perhaps the first motivation for studying $\langle\cos^2\theta_{2D}\rangle$ theoretically in Femtolab appears in the thesis of Jens Hedegaard Nielsen [53]. Jens tried to assess the state purity in a state selected molecular beam by looking at the Fourier transform of an alignment trace. With $\langle\cos^2\theta\rangle$, this can be done with linear molecules because $\cos^2\theta$ only couples neighboring pairs of states with the same parity. The frequencies arising from states with another parity should thus not be present. In his efforts, Jens was frustrated enough to write this call to action:

> "However as we do not measure the full angular distribution but only the 2D projection of the ion distribution, a complication arises that really should be investigated further."

Jens went on to write

> "Furthermore it is either needed to use a probe technique that is sensitive to the full angle or at least do a more detailed investigation of the influence of only measuring the 2D projection."

This and the following sections may be seen as a response to Jens' call for further investigation.

It is apparent from simple uniform circular motion on the unit sphere in the $Z = 1/\sqrt{2}$ plane, characterized by a *constant* polar angle $\theta = 45°$, that the projected motion in the $X = 0$ detector plane is characterized by a periodic and time dependent polar angle θ_{2D}. The periodicity is that of the circular motion. This extra frequency comes from the dynamics in the φ angle. Clearly, the projection has the potential to introduce new frequencies. This example is slightly misleading, as the rotation of the individual molecules in 1D alignment takes place in a plane containing the polarization axis Z. This example was for motion in a plane perpendicular to the Z axis. However, as will be shown, new frequencies are actually introduced in $\langle\cos^2\theta_{2D}\rangle$ traces that are not present in $\langle\cos^2\theta\rangle$ traces. Furthermore, the amplitudes of the spectral components of $\langle\cos^2\theta\rangle$ are modified by the projection.

After the pulse, an analytic expression for the alignment trace $\langle\mathcal{O}\rangle(t)$ based on equation (2.24) is

$$\langle\mathcal{O}\rangle(t) = \sum_{J'J} |C^J_{KM}||C^{J'}_{KM}|\mathcal{O}^{J'}_{JKM} \exp\left(-2\pi i m^J_{J'}(t-t')/T_{\text{rev}} + i(\phi^J_{KM}(t') - \phi^{J'}_{KM}(t'))\right) \tag{2.32}$$

where $T_{\text{rev}} = h/2B$ is the revival time, t' is an arbitrary but fixed time after the pulse and

$$m^J_{J'} = \frac{J(J+1) - J'(J'+1)}{2} \tag{2.33}$$

is an integer since $J(J+1)$ is always even. Equation (2.32) can be seen as a generalization of a result obtained by Bisgaard [54] for $\mathcal{O} = \cos^2\theta$. The phase and magnitude of $C^J_{KM}(t')$ after the pulse at $t = t'$ are $\phi^J_{KM}(t')$ and $|C^J_{KM}|$, respectively. After the pulse, the magnitudes do not depend on time. The field-free evolution of the expansion coefficients $C^J_{KM}(t) = C^J_{KM}(t')\exp\left(-iH^J_K(t-t')/\hbar\right) = |C^J_{KM}|\exp\left(-iH^J_K(t-t')/\hbar + i\phi^J_{KM}(t')\right)$ has been inserted to obtain (2.32). Evidently, the alignment trace is periodic with a period T_{rev} and (2.32) is an expansion in the Fourier basis

$$\langle\mathcal{O}\rangle(t) = \sum_{n=-\infty}^{\infty} c_n \exp(i\omega_n t). \tag{2.34}$$

The harmonic number n is related to the angular frequency by $\omega_n = n\cdot 2\pi/T_{\text{rev}}$. The Fourier coefficient is given by

$$\begin{aligned} c_n &= \frac{1}{T_{\text{rev}}}\int_{t'}^{t'+T_{\text{rev}}} \langle\mathcal{O}\rangle(t)\exp(-i2\pi n t/T_{\text{rev}}) \\ &= \sum_{J'J} \delta_{n,m^J_{J'}} |C^J_{KM}||C^{J'}_{KM}|\mathcal{O}^{J'}_{JKM} e^{i\Delta\phi^{J'}_{JKM}(t')} \end{aligned} \tag{2.35}$$

Here $\Delta\phi^{J'}_{JKM}(t') = \phi^J_{KM}(t') - \phi^{J'}_{KM}(t')$. It should be noted that the Fourier series (2.35) is only for a state with definite K and M, and not e. g. for an ensemble.

A qualitative understanding of alignment traces in the impulsive limit gleams off of equation (2.32). With a δ kick pulse [59–61] acting on the ground state $|000\rangle$, there is no phase evolution during the pulse, so all phases $\phi^{J'}_{JKM}$ would be identical at $t = 0$ immediately after the pulse. Taking $t' \to t_0^+ = 0$, the sum (2.32) would then turn into a sum of cosines (and a constant term), since $m^J_{J'}$ changes sign under exchange of J' and J, and the real, Hermitian $\mathcal{O}^{J'}_{JKM}$ does not. However, a relative phase $\phi^{J+2}_{KM}(t') - \phi^{J}_{KM}(t') = -i$ is introduced by the factor i in the equations (2.11) (neglecting the first term on the right hand side), so the sum is actually over sines. As the pulse strength increases, higher J states become populated, and the first peak of alignment moves closer to $t = 0$, since the sines have increasing frequency, each an integer multiple of the fundamental frequency. Note that the analysis is more complicated for initial states with $|KM| > 0$, since the parity changing $\Delta J = \pm 1$ matrix elements (2.26) are then also in play. It may help, however, that they converge to 0, as noted above.

Generally, the power spectrum $P(\omega_n) = |c_n|^2$ of $\langle \mathcal{O} \rangle (t)$ consists of a series of peaks, each at a discrete angular frequency ω_n, $n = m^J_{J'}$ corresponding to the energy differences between pairs of populated states. The amplitudes of the peaks are given by the populations $|C^{J'}_{KM}|^2 |C^J_{KM}|^2$ of the states multiplied with the square of the matrix element $\mathcal{O}^{J'}_{JKM}$ coupling them, along with a phase relation in case more than one pair of states contribute to the same spectral component. The DC term c_0 in (2.35) involves only the diagonal $\mathcal{O}^J_{JKM}$. All the time dependence of $\langle \mathcal{O} \rangle (t)$ involves only the off-diagonal matrix elements. As noted above, the band $\mathcal{O}^J_{JKM}$ generally converges as J increases. The permanent alignment level (i. e. the DC term) therefore also converge in general as the laser moves population to higher J states. This can be seen by from (2.35). The DC term becomes $c_0 = \sum_J |C^J_{JKM}|^2 \mathcal{O}^\infty_{\infty KM} = \mathcal{O}^\infty_{\infty KM}$. If $K = M = 0$, $c_0 \to \frac{1}{2}$ for $\langle \cos^2 \theta \rangle$ [2]. For $\langle \cos^2 \theta_{2D} \rangle$, $c_0 \to 0.6366\ldots$ This means that for cold molecules subjected to short, intense alignment pulses, $\langle \cos^2 \theta_{2D} \rangle$ is centered around a value of roughly 0.64, and $\langle \cos^2 \theta \rangle$ is centered around a value of roughly 0.5. The first few diagonal matrix elements of $\cos^2 \theta_{2D}$ for low M can be seen in Fig. 2.3. It appears that the matrix elements all converge towards the same limit as $J \to \infty$ as long as M is held fixed. This is in fact case, since the ξ angle in (2.31) converges to 0 independently on M' (but does so slower with increasing $|M'|$).

2.2.3 Reconstruction techniques based on Fourier analysis

Consider now the case $\mathcal{O} = \cos^2 \theta$ for a linear molecule, or more generally a symmetric top starting out in a $K = 0$ or $M = 0$ state, e. g. the ground state. The aim is first to reproduce and explain known alignment behavior, and to show how the rotational wave packet can be reconstructed from such a trace. The matrix elements (2.16) are all zero except when $J' = J \pm 0, 2$. This means that only the pairs of states J and $J \pm 2$ contribute in the sum (2.35) for $n \neq 0$. For the positive frequencies $J > J'$, the *observable* $\cos^2 \theta$ admits harmonic numbers $n = m^{J+2}_J = 2J{+}3$, corresponding to the frequencies $\omega = 2B(2J{+}3)/\hbar$. However, the real frequency spacing is $8B/h = 4/T_{\text{rev}}$ (or $\Delta n = \pm 4$) due to the $\Delta J = 0, \pm 2$

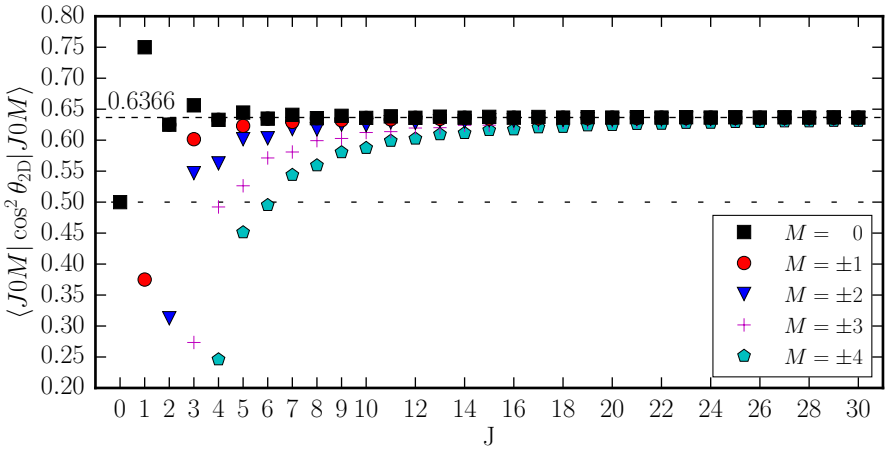

FIG. 2.3: The diagonal matrix elements $\langle J0M|\cos^2\theta_{2D}|J0M\rangle$ for $M = 0, \pm1, \pm2, \pm3, \pm4$. These values contribute directly as the permanent alignment level for each $|J0M\rangle$ state.

rule of the *laser interaction* (2.13). The laser interaction changes J in steps of 2, so only every other frequency admitted by $\cos^2\theta$ shows up. For example frequencies corresponding to $J', J = 4, 6$ appear, while frequencies corresponding to $J', J = 3, 5$ does not, or vice versa if the initial state had an odd J. This constant frequency spacing gives rise to beats, or *revivals* at times $t \approx 0 \cdot T_{\text{rev}}/4$, $1 \cdot T_{\text{rev}}/4$, $2 \cdot T_{\text{rev}}/4$, $3 \cdot T_{\text{rev}}/4$ and $4 \cdot T_{\text{rev}}/4$ etc. These beats are known as the prompt alignment, the 1/4 revival, the 1/2 revival, the 3/4 revival and the full revival, respectively. The phenomenon of revivals is analogous to pulses from mode-locked lasers [71] for example. They appear as a consequence of the quantization of angular momentum. An example of these revivals is shown for CS_2 in Fig. 2.4a). From the corresponding Fourier series, shown in Fig. 2.4c), the expansion coefficients $C^J_{KM}(t)$ can be inferred by solving the nonlinear system of equations (2.35) e.g. for even J

$$\begin{aligned}
\mathcal{O}^0_{2KM}|C^2_{KM}||C^0_{KM}|e^{i\Delta\phi^0_{2KM}(t')} &= c_3 \\
\mathcal{O}^2_{4KM}|C^4_{KM}||C^2_{KM}|e^{i\Delta\phi^2_{4KM}(t')} &= c_7 \\
\mathcal{O}^4_{6KM}|C^6_{KM}||C^4_{KM}|e^{i\Delta\phi^4_{6KM}(t')} &= c_{11} \\
&\vdots \\
\mathcal{O}^{J_{\text{m}}-2}_{J_{\text{m}}KM}|C^{J_{\text{m}}}_{KM}||C^{J_{\text{m}}-2}_{KM}|e^{i\Delta\phi^{J_{\text{m}}-2}_{J_{\text{m}}KM}(t')} &= c_{2J_{\text{m}}+3}
\end{aligned} \tag{2.36}$$

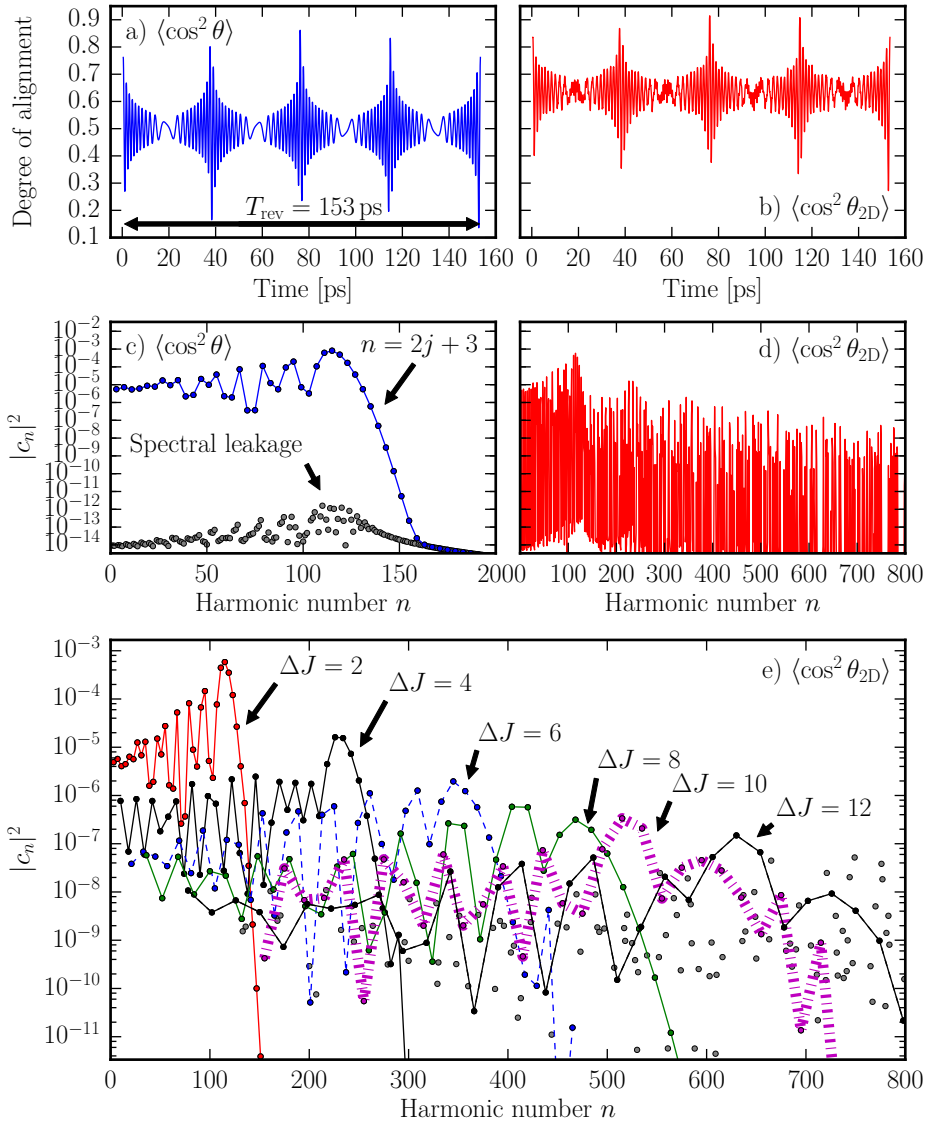

FIG. 2.4: Degree of alignment $\langle\cos^2\theta\rangle$ a) and $\langle\cos^2\theta_{2D}\rangle$ b) for CS_2 after a 300 fs, 10 TW/cm^2 pulse, starting from the ground state $|000\rangle$. The corresponding power spectra $|c_n|^2$ are shown in c) and d), respectively. The frequency is $f = n/T_{\mathrm{rev}} = n \cdot 6.54\,\mathrm{GHz}$. Panels d) and e) show the same spectrum. In panel d), lines are drawn between neighboring points, as is a usual when plotting. In e), lines are drawn between points $n = 4Ni + 2N^2 + N$, where $\Delta J = 2N$ and $i = 0, 1, 2, \ldots$.

where $|J_m KM\rangle$ is the highest populated state. Each phase factor $e^{i\Delta\phi^{J'}_{JKM}(t')}$ is clearly identical to the phase of the Fourier coefficient c_{2J+3} multiplied by the sign of $\mathcal{O}^{J'}_{JKM}$. The above $J_m/2$ equations and the normalization condition

$$\sum_J |C^J_{KM}|^2 = 1 \tag{2.37}$$

may then be enough to uniquely determine the remaining[7] $J_m/2+1$ unknowns. A strategy for solving the system of equations could e. g. be using the nonlinear least squares method, i. e. numerically minimizing the sum squared difference between the left- and right-hand side of the above equations by varying $|C^J_{KM}| \geq 0$. There must be at least one solution corresponding to the actual magnitudes of the expansion coefficients. That solution fixes the expansion coefficients up to an unimportant overall phase factor. Thus the entire wave function may be reconstructed from the Fourier series of a *single period* of a $\langle\cos^2\theta\rangle$ trace. If the Fourier series is not taken over exactly one revival time, the amplitudes c_n leak into neighboring frequencies. This has happened to a small degree in Fig. 2.4c). Reconstruction of the wave packet in this way relies on the assumption that the system starts in a pure state with definite K, M and $K \times M = 0$. For mixed states (i.e. statistical ensembles), the peaks in the power spectra coincide. This results in more unknowns than equations. In this project, no experiments have been performed on state-selected molecules, and only the 2D degree of alignment is measured. This reconstruction technique has therefore not yet been tried in practice. This problem is similar to the one Jens Hedegaard Nielsen encountered.

For a generalized linear molecule $K \times M = 0$, the Fourier spectrum (2.35) of $\langle\cos^2\theta_{2D}\rangle$ is now made up of couplings $\Delta J = 0, \pm2, \pm4, \pm6, \ldots$, since the matrix representation contains many bands. From equation (2.29) and table 2.1 it is seen that the expansion coefficients decrease as J increases. Higher order Legendre polynomials tend to be more oscillatory than lower order polynomials, so the expansion of the relatively slowly varying $\cos^2\theta_{2D}$ dies out as J increases. Couplings with low J therefore still dominate. The $\Delta J = \pm2$ coupling leads to the same frequencies as for $\langle\cos^2\theta\rangle$, with a modified amplitude due to the different numerical value of the matrix elements. The $\Delta J = \pm4$ coupling leads to new positive frequencies $\omega = 2B(4J + 10)/\hbar$, or $n = 4J + 10$, none of which overlap the $\Delta J = \pm2$ frequencies $n = 2J+3$. They are regularly spaced with a real frequency spacing of $16B/h$ ($\Delta n = \pm8$). This is twice the spacing of the $\Delta J = \pm2$ coupling, and gives rise to a new series of 1/8 revivals with a smaller amplitude due to the smaller matrix elements in the $\Delta J = 4$ diagonal. Similarly, higher order couplings lead to $1/12, 1/16, 1/20$, etc. revivals, diminishing in strength due to the decreasing magnitude of the expansion coefficients. An example $\langle\cos^2\theta_{2D}\rangle$ trace is shown in Fig. 2.4b). The new series of frequencies are captured in the corresponding power spectrum in Figs. 2.4d) and 2.4e). The 1/12 and higher order revivals are typically not observed in experiments because they are small and fast,

[7] Each vanishing Fourier coefficient determines that one of the unknowns are zero from e. g. its non-vanishing neighbor coefficients.

and they resemble noise. Generally, the $\Delta J = 2N$, $N = 1, 2, 3, \ldots$ coupling of the observable introduces new positive harmonics at $n = 2NJ + 2N^2 + N$, as can be seen by inserting $\Delta J = 2N$ in (2.33). The laser pulse always changes J in steps of 2, so the observed harmonics are $n = 4Ni + 2N^2 + N$ ($+2N$ if J is odd), where $i = 0, 1, 2, \ldots$ The $\Delta J = 10$ series of frequencies is the first one to overlap with just a few of the $\Delta J = 2$ series of frequencies. The $\Delta J = 6$ series for odd J is the first to overlap a few of the $\Delta J = 2$ series of frequencies for even J. This can safely be neglected, though, since the amplitudes are orders of magnitude smaller, as also seen in Fig. 2.4e). Note that this is not nearly as easy to read off from the same spectrum in Fig. 2.4d), where the frequency components are connected sequentially. Since the series of frequencies practically don't coincide, it is enough to only look at the $\Delta J = 2$ couplings again. The same system of equations (2.36) as for $\langle \cos^2 \theta \rangle$ above is obtained. The only difference is the numerical value of the matrix elements. This allows for reconstruction of the wave packet from $\langle \cos^2 \theta_{2D} \rangle$ in the same way as with $\langle \cos^2 \theta \rangle$, i. e. by simply ignoring the new frequencies. For each series of frequencies, a new system of equations can be derived. However, these systems contains no new information, since the entire wave packet can be reconstructed from the $\Delta J = 2$ series. This technique has again not been tested in this thesis, since I have not worked with state-selected molecules. In order to reconstruct the wave packet with these techniques, the ensemble of molecules must all experience the same kick pulse strength, i. e. the alignment pulse should have a uniform (top hat) spatial profile. For e. g. a Gaussian spatial beam profile, it is difficult to ensure that the detected molecules have all experienced the same alignment pulse strength.

Reconstructing $\langle \cos^2 \theta \rangle(t)$ directly from $\langle \cos^2 \theta_{\mathbf{2D}} \rangle(t)$

The above techniques rely on having an initial state with a well-defined K and M quantum number. Experimentally, this means the techniques only work for state selected molecules. It is only possible to reconstruct the wave function for a pure state. Perhaps a much more interesting result is that it is possible to reconstruct $\langle \cos^2 \theta \rangle(t)$ directly from $\langle \cos^2 \theta_{2D} \rangle(t)$ under more general conditions, as will be demonstrated here. This reconstruction method is insensitive to uncorrelated, broadband noise, as it involves cutting away most of the frequency spectrum.

The frequencies arising from the $\Delta J = 2$ coupling separate from other frequencies. A simple way to reconstruct $\langle \cos^2 \theta \rangle$ from $\langle \cos^2 \theta_{2D} \rangle$ therefore suggests itself. First, all frequencies other than those pertaining to the $\Delta J = 2$ series are discarded in the Fourier series of $\langle \cos^2 \theta_{2D} \rangle$. The sum on the right hand side of equation (2.35) then contains only one term for a given $n \neq 0$. The Fourier coefficient c_n for $\langle \cos^2 \theta \rangle$ is then reconstructed by dividing away the corresponding matrix element $\mathcal{O}^{J+2}_{JKM}$ for $\cos^2 \theta_{2D}$ and multiplying back on the same matrix element for $\cos^2 \theta$, i. e. multiplying with

$$U^2_{JKM} = \frac{\langle (J+2)KM | \cos^2 \theta | JKM \rangle}{\langle (J+2)KM | \cos^2 \theta_{2D} | JKM \rangle}. \tag{2.38}$$

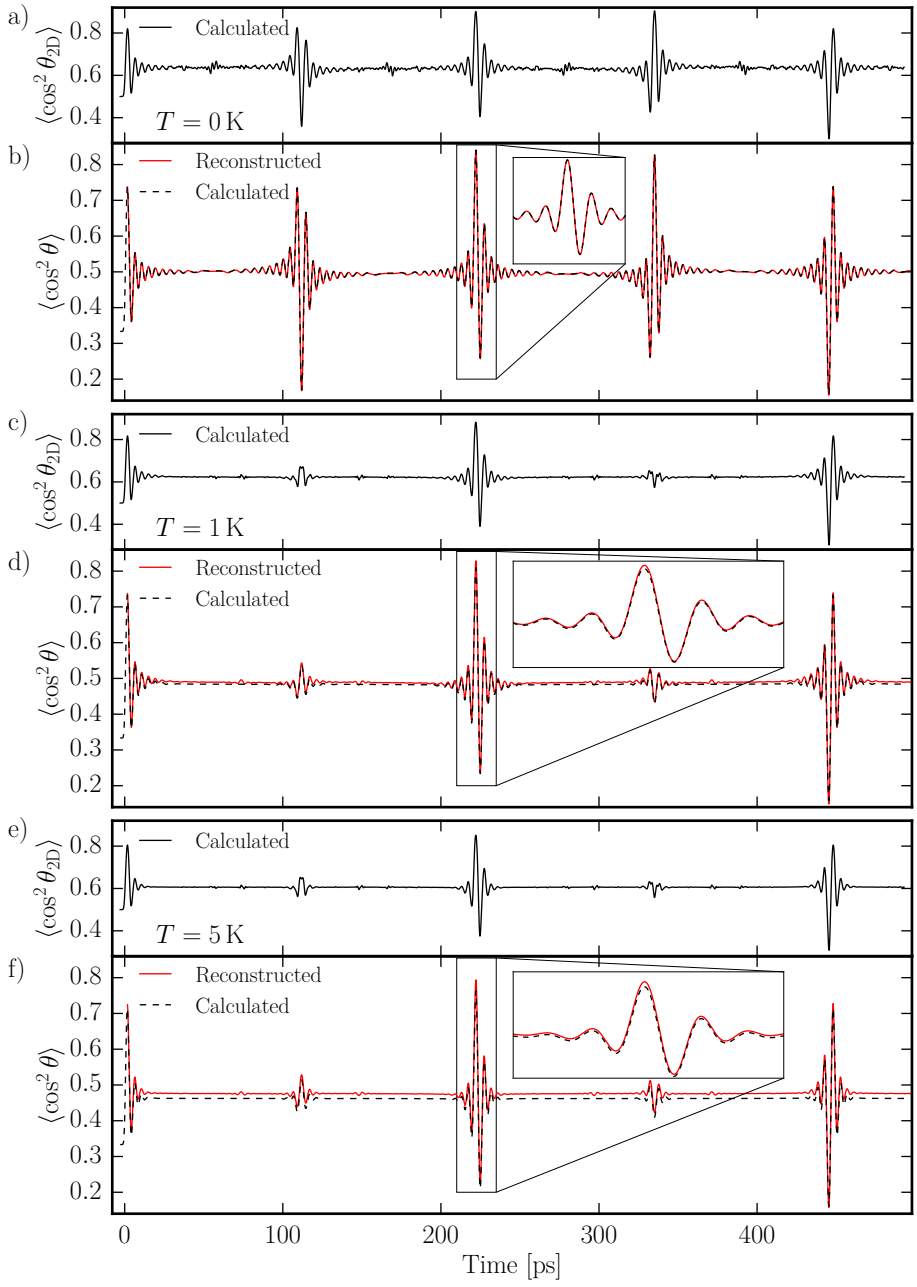

FIG. 2.5: Calculated $\langle\cos^2\theta_{2D}\rangle$ traces a),c),e) for I_2 at temperatures 0, 1 and 5 K, respectively. The peak laser intensity is 3.686 TW/cm^2 and the pulse duration is 1.3 ps. Panels b),d) and f) show the corresponding $\langle\cos^2\theta\rangle$ traces. Also shown is the reconstructed $\langle\cos^2\theta\rangle$ trace based only on the $\langle\cos^2\theta_{2D}\rangle$ trace (see text).

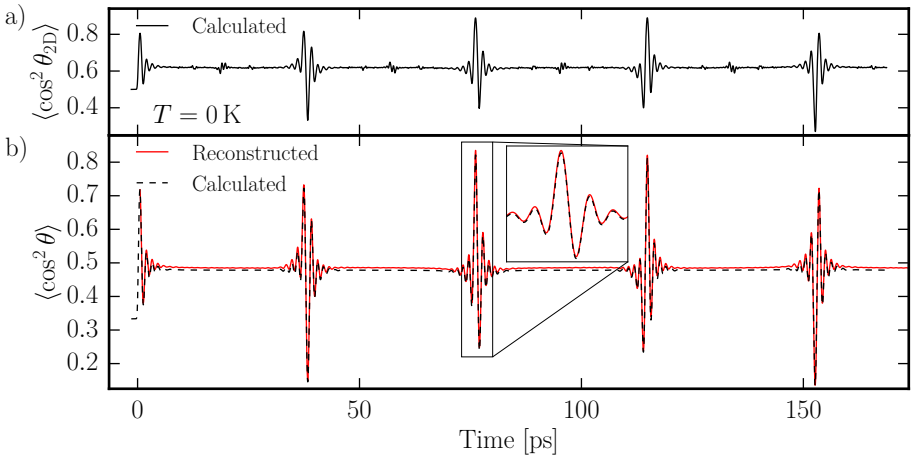

FIG. 2.6: As 2.5e) and 2.5f) except this is for CS_2 exposed to a $10\,\mathrm{TW/cm^2}$, 300 fs pulse

Reconstructing $\langle\cos^2\theta\rangle$ would then be a simple matter of applying the inverse Fourier transform. However, the DC term with $n = 0$ is not as easily reconstructed, since the different matrix elements in the sum in (2.35) cannot be taken outside the summation. However, inspection of the numerical values of

$$U^0_{JKM} = \frac{\langle JKM|\cos^2\theta|JKM\rangle}{\langle JKM|\cos^2\theta_{2D}|JKM\rangle} \tag{2.39}$$

indicates that the convergence noted above is extremely rapid, e.g. $U^0_{J00} \to 0.785398\ldots$ as $J \to \infty$. The approximation $U^0_{J00} \approx 0.785398$ is accurate to within 1 % already at $J > 4$ and at least as far as to $J = 1000$. Under this approximation, the matrix elements can be taken outside the summation and the full spectrum, and, in turn, $\langle\cos^2\theta\rangle$, can thereby be reconstructed. This reconstruction method is applied to a calculated $\langle\cos^2\theta_{2D}\rangle$ trace for the ground state of I_2 exposed to a relatively high intensity laser pulse. The result is shown in Figs. 2.5a)-2.5b). As can be seen, the agreement with the calculated $\langle\cos^2\theta\rangle$ trace is excellent. In contrast to the wave packet reconstruction method described above, this approximate method generalizes to ensembles of initial states with different M. Inspection of the numerical value of the conversion factors U^2_{JKM} reveals that the difference $U^2_{J00} - U^2_{J0M}$ for a given M quickly become negligible as J increases. The difference for $J > M + 10$ first exceeds 10 % when $M = 10$. In typical nonadiabatic alignment experiments, much higher J states dominate the wave packet. The $U^0_{J0M} \approx 0.785398$ approximation for the DC term has a comparable, but slightly worse accuracy for $M > 0$.

The black curves in Fig. 2.5 show $\langle\cos^2\theta_{2D}\rangle$ and $\langle\cos^2\theta\rangle$ calculated for I_2 for

different temperatures. The red, fully drawn curves are $\langle\cos^2\theta\rangle$ obtained from the $\langle\cos^2\theta_{2D}\rangle$ data by following the reconstruction method just described. For 0 temperature, only a single state is included, and the reconstruction is nearly perfect. As the temperature increases, a distribution of states with increasing M are populated. As a result, small deviations from the true degree of alignment are observed, particularly for the 5 K case. The most significant error is in the DC term. With the relatively low B constant of I_2, more M states are populated at a given temperature than for e.g. CS_2. The reconstruction therefore works better at 5 K for CS_2, as shown in Fig. 2.6.

As a side note, the effects of nuclear spin statistics on the alignment dynamics can be seen by comparing Fig. 2.6 with panel e) and f) in Fig. 2.5. CS_2 in the (even) electronic ground state can only occupy even rotational states due to the spin 0 bosonic sulfur only supporting one even spin combination. I_2 can occupy both even and odd rotational states since iodine has spin 5/2, supporting both even and odd nuclear spin combinations. The 1/4 and 3/4 revivals are strong for CS_2 and weak for I_2. I_2 still favors one parity over another, so those revivals are not entirely washed out. From the even ground state in Fig. 2.5b), the laser only excites to other even states, and the 1/4 and 3/4 revivals are suddenly strong for I_2. The quarter revivals for odd and even rotational states tend to cancel out [72].

The extension of this method to symmetric tops $|K|, |M| > 0$ is complicated by the fact that the $\Delta J = \pm 1$ selection rule now applies to both the laser interaction and the observables $\cos^2\theta$ and $\cos^2\theta_{2D}$. Symmetric tops thus exhibit 4 times as many frequency series, some of which overlap the $\Delta J = 1, 2$ series of frequencies of $\cos^2\theta$. The extra frequencies of $\cos^2\theta_{2D}$ can therefore not be trivially removed. However, in many cases, e. g. the one shown in Fig. 2.4, the most significant part of the wave packet is reasonably well localized spectrally. In those cases, the higher frequencies introduced by $\cos^2\theta_{2D}$ could then be expected to localize away from the low frequencies required for reconstructing $\cos^2\theta$.

Application of reconstruction method to experimental data

The result of applying the reconstruction method to experimental data is shown in Fig. 2.7. Panel a) shows a recorded alignment trace for I_2. Note that the trace is centered roughly around $\langle\cos^2\theta_{2D}\rangle = 0.64$. Panel b) shows the power spectrum of that alignment trace. It is seen that the predicted peaks arising from the $\Delta J = 2$ and $\Delta J = 4$ couplings are reproduced experimentally. Peaks from higher order couplings are washed out by experimental noise. The even amplitudes are lower than the odd amplitudes by about a factor 2, which is consistent with a 15:21 mixing due to nuclear spin statistics. This difference is absent in the $\Delta J = 4$ branch, however. The high harmonics involved in that branch are not sufficiently well resolved. The trace is sampled every 4 ps between the $\Delta J = 2$ revivals, and every 0.5 ps during those revivals. In panel c), the reconstructed $\langle\cos^2\theta\rangle$ trace is shown. Note the slight difference in scaling between panel a) and c). It is seen that $\langle\cos^2\theta_{2D}\rangle$ is consistently larger than $\langle\cos^2\theta\rangle$. This means e. g. the degree of alignment is overestimated, and the degree of anti-alignment is

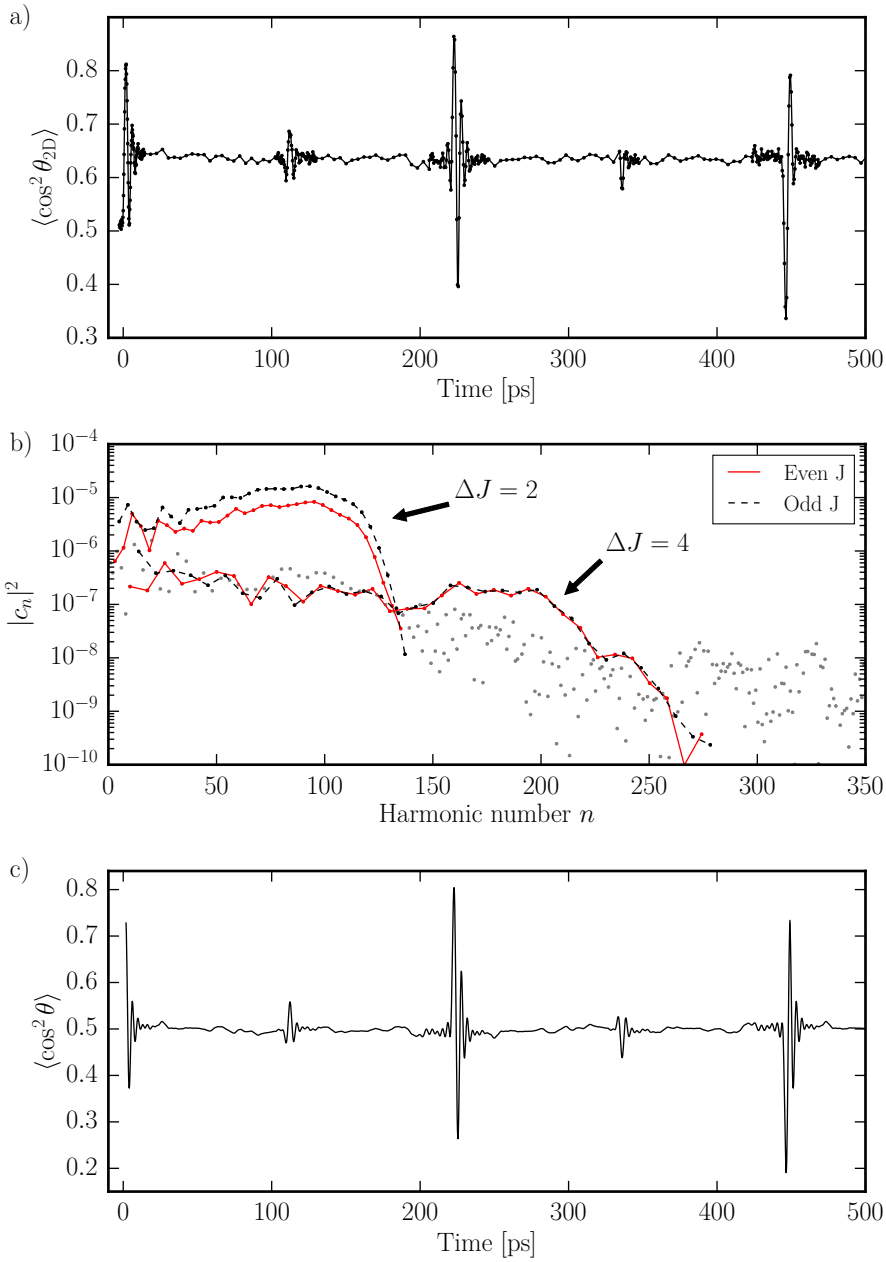

FIG. 2.7: a) Measured $\langle\cos^2\theta_{2D}\rangle$ trace for I_2. A 3.7 TW/cm^2, 1.2 ps alignment pulse is used. b) Power spectrum of the measured alignment trace. c) $\langle\cos^2\theta\rangle$ trace reconstructed from the measured $\langle\cos^2\theta_{2D}\rangle$ trace.

under-estimated. I recorded the experimental data presented here together with Benjamin Shepperson. This data is a small part of the data that will be presented in chapter 5.

2.2.4 Modeling probe selectivity and nonaxial recoil

In Coulomb explosion imaging experiments, an underlying assumption is that molecular fragments are recoiled along molecular bond axes. This assumption can be violated by e. g. multiple Coulomb interacting fragments, vibrations and non-instantaneous bond-breaking. Only diatomic molecules are guaranteed to recoil perfectly due to conservation of momentum. There has recently been some progress in deconvoluting nonaxial recoil from experimentally obtained alignment traces [55]. However, like the Abel inversion, the procedure relies on having better statistics than what is typically needed just to obtain an alignment trace. Consequently, only a few selected points along the alignment trace would typically be deconvolved. Another effect that can blur alignment traces is that of probe selectivity. The probe laser may enhance the ionization rate along certain molecular axes, thus skewing the measured expectation value [73]. The process of inverting this effect [74] has similar drawbacks.

With the machinery surrounding equations (2.26) and (2.29), the expectation value of any observable can be calculated efficiently by calculating a small set of reduced expansion coefficients for the observable. Thus, a quantum mechanical description of probe selectivity and nonaxial recoil is now within reach. Probe selectivity is a weighting $W_\rho(\Omega)$ of the detection probability depending on the molecule-probe orientation ρ. Given $W_\rho(\Omega)$, alignment traces with probe selectivity taken into account can be calculated by evaluating $\langle W_\rho(\Omega) \cos^2\theta_{2D} \rangle$.

Given that the molecule points in some direction Ω, nonaxial recoil is characterized by a probability $P(\Omega'|\Omega)$ that the fragment is actually ejected in another direction Ω'. The effects of this can be taken into account by evaluating $\langle \int \cos^2\theta'_{2D} P(\Omega'|\Omega) d\Omega' \rangle$. If $P(\Omega'|\Omega) = P(\Omega' - \Omega)$, i. e. the probability is only a function of the difference between the two orientations, then this is a spherical convolution, which can be performed efficiently. Both effects can be taken into account simultaneously by evaluating $\langle W_\rho(\Omega) \int \cos^2\theta'_{2D} P(\Omega'|\Omega) d\Omega' \rangle$. A derivation leading to these claims can be found in Appendix A.2.

The problem of determining $W_\rho(\Omega)$ and $P(\Omega'|\Omega)$ remains, however. Assuming a Gaussian dependence, the width of $P(\Omega'|\Omega)$ can be measured with the technique in reference 55. A literature study might give a similar idea for $W_\rho(\Omega)$, e. g. $W_\rho(\Omega) \propto \cos^2\theta'$, where θ' is the angle between the molecular axis and the *probe* polarization. These ideas are not explored further in this thesis, as the development of the theory is some of the very latest research that I have conducted during my PhD project.

2.2.5 Proposal: Calculating 2D angular distributions

A more rigorous comparison between theory and experiment could also involve comparing measured 2D angular distributions to those predicted by the theory. The 3D angular distributions $P(\theta)$ were obtained earlier [54], calculated directly from the expansion coefficients C_{KM}^{J} of the rotational wave function. However, the method that was used does not trivially apply to the 2D case, since the projection operation is cumbersome in the framework of angular momentum algebra and spherical coordinates.

Since expectation values can be calculated efficiently, the 2D distribution $P(\theta_{2\mathrm{D}})$ could instead be obtained from the expectation values of some basis functions. For example the moments

$$\left\langle e^{-\pi i n u} \right\rangle = \int_{-1}^{1} P(u) e^{-\pi i n u} \, du, \tag{2.40}$$

which are simply the Fourier coefficients of the 2D angular distribution. Here, $u = \cos\theta_{2\mathrm{D}}$. The 2D angular distribution $P(\theta_{2\mathrm{D}})$ can be calculated by inverse Fourier transforming the calculated expectation values. As $P(u)$ is real, $\left\langle e^{\pi i n u} \right\rangle = \overline{\left\langle e^{-\pi i n u} \right\rangle}$, and only e. g. positive moments need to be calculated. Calculating e. g. the first 100 moments would be roughly 100 times slower than calculating $\langle \cos^2\theta_{2\mathrm{D}} \rangle$ alone, but would still be very feasible. If the distribution is only required at few points in time, the calculation would be about as fast as calculating $\langle \cos^2\theta_{2\mathrm{D}} \rangle$ for the whole time range.

The 3D angular distribution can be calculated in the same way with $u = \cos\theta$. It would be interesting to compare the speed of this calculation with the speed of the method in the PhD thesis of Christer Bisgaard [54]. At least in the 3D case, the expectation values of the Legendre polynomials are probably better suited than those of the Fourier basis, since here the reduced expansion coefficients (2.29) can be evaluated analytically with the orthogonality properties of the Legendre polynomials. Thus no numerical integration would be required.

2.3 Summary

To summarize, the theory of 1D alignment of symmetric tops has been reviewed. An extension to the existing theory has been presented. This extension includes a way to calculate relevant matrix elements of arbitrary observables in the symmetric top basis efficiently. Specifically, the observable $\cos^2\theta_{2\mathrm{D}}$ has been analyzed. In order to compare experiments to theory, previous efforts have involved laboriously inverting 2D measurements to the corresponding 3D version. This work provides an alternative, namely theoretically predicting the 2D measurements. To further approach the experimental reality, a way to simulate nonaxial recoil and probe selectivity has been proposed. In addition, a highly efficient way of inverting 2D measurements of initially cold linear molecules have been introduced. This method relies only on spectral analysis of the final alignment trace $\langle \cos^2\theta_{2\mathrm{D}} \rangle$, and e. g. does not involve extra analysis or inversion of angular distributions.

CHAPTER 3

Building an efficient and user-friendly alignment calculator

In this chapter, an efficient and user-friendly alignment calculator for isolated symmetric tops is described. The calculator builds on the work of Christer Bisgaard [54]. Christer created a prototype implementation written in C++, which I have completely rewritten in Python and C. Having access to an already working prototype has allowed me to focus on improving the program design. The new program is significantly more user-friendly and portable, and an effort has been made to write easy to follow, modular and maintainable code. Furthermore, the time critical parts have been substantially optimized. With the new program, it is no longer necessary to edit program code in order to run a new molecule. Each new molecule can be specified with a few parameters in a simple, easy to follow configuration file. The propagation no longer depends on any particular solver implementation. This means that new, faster methods are easy to substitute in. Traces that would take several minutes to calculate with the prototype code now takes less than a second. The program can now be invoked through a command-line interface. I have also added a graphical interface. The graphical interface simply translates the graphical input to the command line invocation. The program runs on both Linux and Windows PCs. Furthermore, the program now calculates $\langle \cos^2 \theta_{2\mathrm{D}} \rangle$ as well as $\langle \cos^2 \theta \rangle$. Overall, the new calculator is much better suited for dissemination purposes, as it is easy to use and results can be delivered almost instantaneously. Students with little to no programming experience can quickly perform highly accurate simulations. The calculator has also proved to be a useful tool in the laboratory for quickly evaluating whether experimental results can be understood as exemplified in section 3.4

The basic principle behind of the simulation is straightforward. First, equations (2.11) are solved numerically during the pulse. After the pulse, the field-free stationary states are propagated by applying the usual complex phase factors. Expectation values are obtained by applying the matrix representation of each observable. Even so, a number of technical details complicate the description. These details mainly concern efficient utilization of the computer hardware. The most important of these are described in section 3.1. In order to reproduce actual alignment experiments, it is important to take into account thermal and focal volume averaging. These effects are discussed in section 3.2. In section 3.3, the graphical user interface is described. A brief introduction to the practicalities of using the program is given. This section is mainly aimed at new users of the program. In section 3.4, three interesting real-world examples of advanced usage of the calculator program is discussed. The theme here is to reproduce experimental results as accurately as possible. I have only been involved in the experimental work in the first example.

The calculator program has been made freely available for anyone to use [75].

3.1 Numerical solution of the time dependent Schrödinger equation

The matrix elements (2.16) of $\cos^2\theta$ are calculated with special case 3j symbol formulas from the book of Zare [58] that does not suffer from catastrophic cancellation,

$$\begin{pmatrix} J & J & 2 \\ M & -M & 0 \end{pmatrix} = (-1)^{j-m} A_2(2J+3)2[3M^2 - J(J+1)] \tag{3.1}$$

$$\begin{pmatrix} J+1 & J & 2 \\ M & -M & 0 \end{pmatrix} = (-1)^{j-m+1} A_2(2J+4)2M\sqrt{6(J+M+1)(J-M+1)} \tag{3.2}$$

$$\begin{pmatrix} J+2 & J & 2 \\ M & -M & 0 \end{pmatrix} = (-1)^{j-m} A_2(2J+5)\sqrt{6(J+M+2)(J+M+1)} \times \sqrt{(J-M+2)(J-M+1)} \tag{3.3}$$

$$A_2(X) = [X(X-1)(X-2)(X-3)(X-4)]^{-\frac{1}{2}}. \tag{3.4}$$

For performance reasons having to do with CPU cache utilization, the matrix elements are stored as three arrays, corresponding to the five diagonals in the symmetric matrix. The matrix elements of higher bands are all zero and are not stored. The interaction matrix elements for unit intensity $I = 1$ are then calculated as per equation 2.13 and stored in the same way. When needed, they are scaled with the instantaneous envelope intensity $I(t)$. Modern CPUs are much faster than memory (RAM), so in order not to stall calculations while waiting for the memory, CPUs implement a small, extremely fast cache memory area[1].

[1] Actually, they implement a hierarchy of increasingly faster but smaller caches.

Storing only the nonzero matrix elements, and in the order in which they are needed ensure locality of reference, such that the cache area is always full of the numbers that are needed next. For similar reasons, the expectation values are evaluated immediately after calculating the wave function $|\Psi(t_i)\rangle$ in each time step i after the pulse, such that the entire wave function $|\Psi(t)\rangle$ is only transferred to the cache area once. With a memory speed of about 10 GB/s, each reload of the entire wave function (~ 10 MB) would increase the overall running time of the simulation by 10 %[2]. In case $\langle\cos^2\theta_{2\mathrm{D}}\rangle$ must be evaluated, the matrix elements of $\cos^2\theta_{2\mathrm{D}}$ are calculated with the algorithm from section 2.2. For the common case of $K \times M = 0$, e. g. a linear molecule, the wave function is a superposition of states with the same parity. Therefore, rows and columns of the $\cos^2\theta_{2\mathrm{D}}$ matrix corresponding to the opposite parity are removed. This makes the evaluation of the expectation value (2.18) about 4 times faster in those cases.

The numerical solution method works with any pulse shape. This will be demonstrated below in section 3.4. However, for simplicity, the pulse intensity is assumed to be Gaussian

$$I(t) = I_0 \exp(-4\ln(2)((t-t_0)/\tau)^2), \tag{2.3}$$

where again I_0 is the peak intensity and τ is the full width at half maximum duration. For $|t - t_0| > 1.5\tau$, the intensity is set to zero $I = V = 0$. The time dependent Schrödinger equation is solved by solving the coupled system of ordinary differential equations (2.11). Of the explicit ordinary differential equation solvers available in the Gnu Scientific Library [64], the embedded Runge-Kutta Prince-Dormand (8, 9) method was found to be most efficient for solving the system. One state can be propagated in about 10 ms on a normal laptop computer. These 10 ms include the evaluation of $\langle\cos^2\theta_{2\mathrm{D}}\rangle$ and $\langle\cos^2\theta\rangle$ and the field-free propagation $1.1T_{\mathrm{rev}}$ after the pulse by applying the phase factors $\exp(-iH_K^J(t-t_0)/\hbar)$ to each of the expansion coefficients. Evaluation of $\langle\cos^2\theta_{2\mathrm{D}}\rangle$ alone takes most of the total time, since it involves the only non-sparse matrix in the entire simulation. At one point, however, by far the most of the running time of the entire program was spent inside the complex exponential standard C library function `cexp()`, called from the field free propagation code to evaluate the complex phase factors. The complex exponential function must evaluate the transcendental $\sin(x)$ and $\cos(x)$ functions. To avoid these expensive evaluations, the recursion relation

$$\exp(-iBJ(J+1)\Delta t) = \exp(-iB(J-1)J\Delta t)\exp(-2Bi\Delta t)^J \tag{3.5}$$

is utilized, such that `cexp()` must only be evaluated twice in each time step after the pulse, instead of once per basis state per time step. Here, $\Delta t = t - t_0$. This method significantly increases the overall program performance. As an

[2] This slow reloading approach is unavoidable in matrix languages such as Matlab or Pythons Numpy, since they can only perform one basic matrix operation at a time, resulting in one reload per basic matrix operation. This problem is only important for arrays larger than the cache size (typically a few megabytes).

alternative, the complex exponentials for a fixed time step could be evaluated once and for all. Then the wave function could be propagated incrementally with these constant factors. However, that method turned out to be numerically unstable. Note that the recursion relation also works for $K \neq 0$, since the $(A-B)K^2$ term does not depend on J. The exponential of the term therefore separates. The recursion breaks down, however, if centrifugal distortion is included.

In its current state, the program typically spends roughly 5 times longer in the field-free section than it spends inside the pulse propagation section. In the light of the newly developed theory of the previous chapter, a potentually significant performance improvement is revealed for this field-free section. Although the program is now so fast that spending time on further optimizations is hard to justify, this optimization is worth discussing. The discussion exemplifies how the new theory opens for more ways of thinking about alignment. By calculating the Fourier coefficients (2.35), the trace (2.34) can be obtained by use of the inverse fast Fourier transform (FFT). Doing so would e. g. eliminate the matrix multiplication with the observable in each time step. A simple comparison between the running time of the program and that of an inverse FFT of the relevant size has shown, however, that the current approach is still somewhat faster. The current methods running time was once dominated by the slow evaluation of the complex exponentials. The running time was drastically reduced by evaluating the exponentials with the recursion relation (3.5). The worse performance of the FFT method is therefore probably due to the relatively large number of complex exponential, so-called twiddle-factors involved in the well-known Cooley-Tukey FFT algorithm. However, the Fourier transform is linear, so instead of applying it to each initial state, it could as well be applied to a weighted sum of the Fourier coefficients of each initial state or focal volume intensity in an ensemble, as will be described shortly. In this way, the field-free propagation and calculation of expectation values for each state in an *entire ensemble* could be replaced by a *single* inverse Fourier transform. As much as a 6-fold performance improvement (depending on the basis size) could then be gained as a result. This optimization would mostly be worth implementing if the alignment of larger molecules at finite temperatures must be simulated, in the unlikely case that they are not asymmetric tops. A major downside to the Fourier transform approach is that extensions to the simulation algorithm, e. g. inclusion of centrifugal distorsion, could become impossible.

3.2 Thermal and focal volume averaging

The alignment laser pulse, called the *pump* pulse, also known as the kick pulse, rotationally excite the molecules and induces alignment. The *probe* pulse, used in the Coulomb explosion method, detects the orientation of molecules inside its focal volume. In the experiments, this focal volume is not much smaller than the focal volume of the pump. In order to obtain agreement with experiment, it is crucial, as was pointed out by Bisgaard [54], to average observables over the

spatial intensity profile of the pump within the focal volume of the probe. In the experiments, the two laser beams are collinear and have cylindrical symmetry. It is assumed that the detection probability is proportional to the probe intensity and that the spatial intensity profiles of both beams are Gaussian. For example, the pump intensity is given by

$$I(t,\ell) = I(t)\exp\left(-\frac{2\ell^2}{\omega_k^2}\right), \tag{3.6}$$

where ω_k is the spot size of the pump and ℓ is the distance from the center. Then, the probability dP of a detection from an infinitesimal cylindrical shell with a thickness $d\ell$ is

$$dP(\ell) \propto \exp\left(-\frac{2\ell^2}{\omega_p^2}\right)\ell d\ell, \tag{3.7}$$

where ω_p is the spot size of the probe. Calculated alignment traces are averaged over a number of coaxial, cylindrical iso-intensity shells (cut off at $\ell = 1.7\omega_p$) weighted by the detection probability $dP(\ell)/d\ell$ of each shell. In the experiments presented in chapter 5, $\omega_p = 20\,\mu\text{m}$ and $\omega_k = 35\,\mu\text{m}$. In order to obtain good agreement with experiments, it is also important to take into account temperature effects. The thermally averaged alignment trace is calculated as

$$\langle\cos^2\theta_{2D}\rangle = \sum_i w_i \left\langle\cos^2\theta_{2D}\right\rangle_i \tag{3.8}$$

where the sum is over the initial states $i = |JKM\rangle$ in the ensemble. The weights w_i are calculated according to the Boltzmann distribution, while taking into account nuclear spin statistics. The matrix elements for the laser interaction (2.13) and for the observable (2.26) are invariant under exchange of J and J', and the product of two 3j symbols is invariant under two odd, simultaneous permutations of columns. Therefore, the expectation value $\langle\mathcal{O}\rangle_{i=|JKM\rangle}$ is identical to $\langle\mathcal{O}\rangle_{i=|J,-K,-M\rangle}$. As a consequence, only about half of the states in an initial ensemble need to be propagated. The results from the rest are obtained by doubling the relevant weights w_i. The thermal and focal volume averaging over initial states and intensity shells is done in parallel, since the summation involved is completely incoherent. That is, one initial state can be propagated independently of the other.

The individual and combined effects of thermal and focal volume averaging can be seen in Fig. 3.1. The first panel 3.1a) shows $\langle\cos^2\theta_{2D}\rangle$ for I_2 starting in its ground state and subjected to an ultra fast pulse. A rich structure can be seen. The main revivals from the $\Delta J = \pm 2$ coupling are accompanied with several oscillations, or ringings, due to the large superposition of harmonics. In the middle between the four main revivals, some faster oscillations are seen. These are the revivals due to the $\Delta J = \pm 4$ coupling. They do not appear in a $\langle\cos^2\theta\rangle$ trace. Below, in panel 3.1b), the effects of focal volume averaging are shown. The different pump intensities inside the probe focal volume lead to

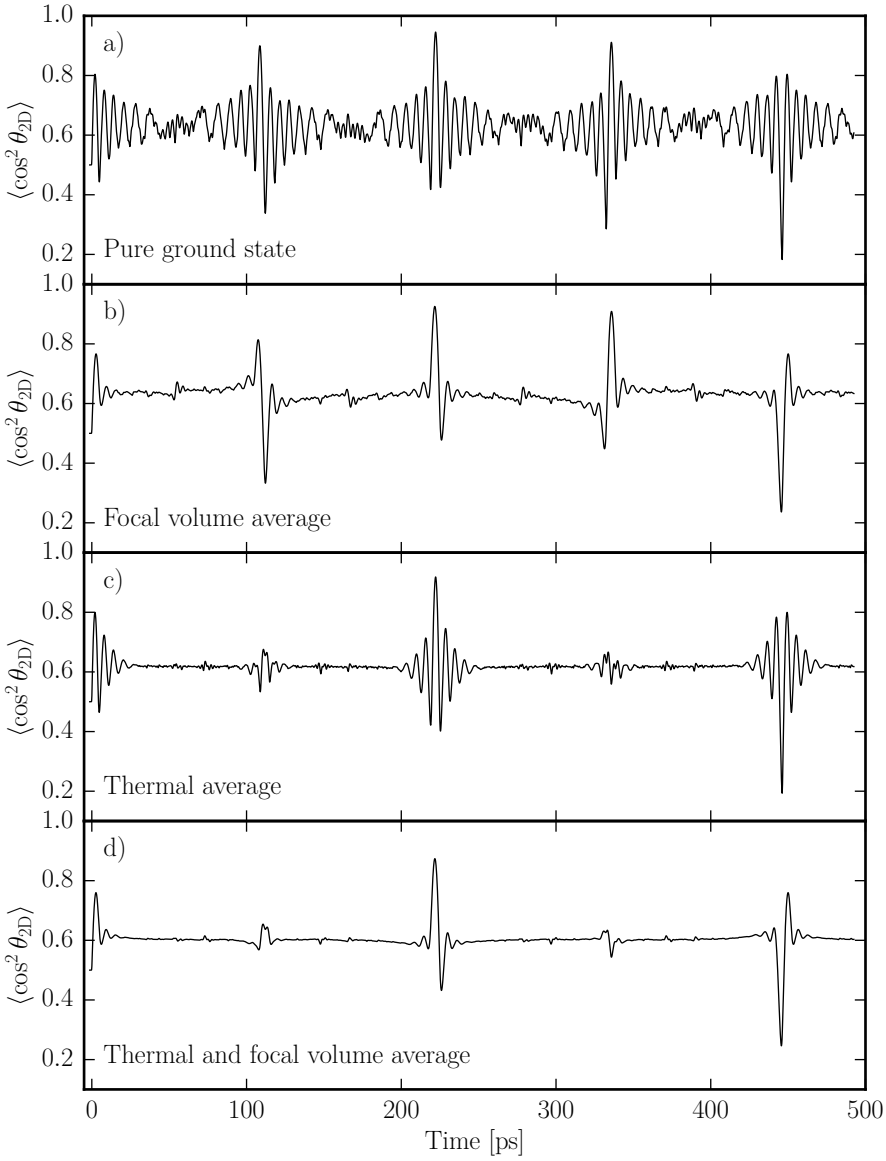

FIG. 3.1: Alignment traces calculated for I_2 subject to a 10 TW/cm^2, 300 fs Gaussian pulse. In panel a), only the ground state is propagated. In panel b), the ground state is averaged over 30 iso-intensity shells corresponding to a 35 µm pump and 25 µm probe spot size. In panel c), a 1 K Boltzmann ensemble is propagated. In panel d), the ensemble is focal volume averaged as in b).

different frequencies for the most prominent harmonics. This smears out most of the structure seen in the first panel, as the individual peaks belonging to each intensity arrive at different times, depending on the intensity shell. Only exactly at the revivals are the different harmonics guaranteed to be in phase, so the revivals become much more sharp. The effects of thermal averaging can be seen in panel 3.1c). Here, a 1 K thermal ensemble is subjected to the same pulse. The main change is that the 1/4 and 3/4 revivals die out. As discussed above, this is due to odd and even states being out of phase at the time of these revivals. Thermal averaging has a similar smearing effect as focal volume averaging, and further smears out the step function behavior of the permanent alignment level at each revival. In the final panel 3.1d), the combined effect of both averaging mechanisms is shown. The revivals are the only remaining structure. After taking into account both effects, $\langle \cos^2 \theta \rangle$ traces are completely flat between the 4 main revivals. This is not the case for $\langle \cos^2 \theta_{2\mathrm{D}} \rangle$. As can be seen, plenty of fine structure survives. This structure could easily be mistaken as experimental noise.

These averaging effects represent a loss of information, e. g. for reasons already discussed in the preceding chapter. Experimentally, the effects of thermal averaging can be eliminated by using a state-selected molecular beam [72]. The effects of focal volume averaging can be minimized by using a probe spot size significantly smaller than the pump spot size, at a cost of a significantly reduced detection probability. The focal volume effects can be completely removed by using a top-hat laser intensity pump beam profile. Focusing lenses for converting from a Gaussian to a top hat spatial profile are commercially available. To my knowledge, both effects have never simultaneously been removed in experiments.

3.3 Introduction to the graphical interface

The graphical front end of the calculator program is shown in Fig. 3.2. It is drawn in a Qt5 designer program, which saves the design in a .ui file. The .ui file is translated to Python code with the pyuic5 program. The interface logic is then written in Python. The interface logic validates the user input and passes it on to the command line version of the calculator, which is also written in Python. The command line tool distributes the initial states and intensities over the available CPU cores. The job of calculating the individual alignment traces is then passed on to a shared library, written in C and briefly described above.

Viewing the graphical interface in normal reading order, the molecules are specified by their rotational constants and polarizability tensors. A large selection of predefined molecules can be selected from a drop down menu. The molecules in the menu are loaded from the “conf/molecules.conf” file when the program starts up. The linearly polarized, Gaussian laser pulse is specified by its peak intensity and FWHM duration. The waists of the pump and probe pulses are specified in order to do focal volume averaging. The number of focal volume intensity shells is specified in the “#FVA shells” field. Specifying 1 shell disables focal

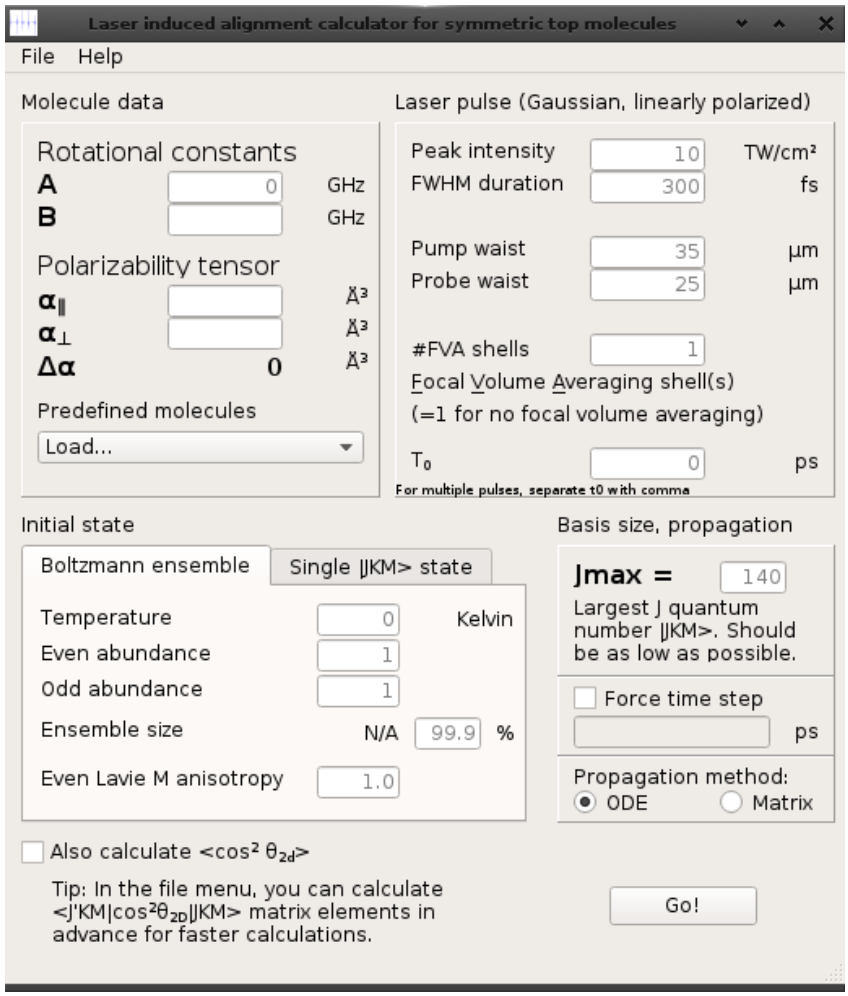

FIG. 3.2: Graphical interface of the alignment calculator program.

volume averaging. Multiple, temporally non-overlapping pulses can be specified by giving a comma separated list of pulse times. The parameters of each pulse may likewise be specified as a comma separated list in the above fields. In case more than one pulse is specified, fields with only one value are interpreted as comma separated lists with the field value repeated for each pulse. Completely identical pulses can e. g. be specified by only giving their times in a comma separated list in the "T_0" field. Below the molecule and pulse input fields, the initial state or states are specified. The user can choose between a Boltzmann ensemble or starting from a single $|JKM\rangle$ state. The even and odd abundances are discussed below. The ensemble size is calculated from the rotational constants, the temperature and the given percentile of the Boltzmann distribution to resolve. If 100 % of the distribution is selected, an infinite number of states would typically be required. With a lower percentile, fewer states must be propagated. Specifying the percentile allows a trade-off between accuracy and speed. The default 99.9 % quite aggressively trades for accuracy. The Even Lavie M anisotropy allows a skewing of the Boltzmann distribution to favor either low or high M states. This doesn't seem to have any influence over the alignment trace, as also noted in Ref. 54. Note that this anisotropy parameter is defined differently from the one in Ref. 54. If a single $|JKM\rangle$ state is chosen and focal volume averaging is disabled, the distribution of J states is also indicated to the user. In the lower right box, the basis size is specified by $J_{\max}$, i. e. the largest J quantum number to include. The calculation time scales quadratically with $J_{\max}$. If the basis size is too small, the calculation fails with an error message. A plotting time step can be specified. A reasonable time step that captures the $\Delta J = \pm 2$ coupling frequencies (and $\Delta J = \pm 4$ if $\langle \cos^2 \theta_{2D} \rangle$ is calculated) is automatically selected if the time step is unspecified. Performance wise, it is a good idea to increase the time step if adiabatic pulses are used, because the long pulse defines the relevant time scale instead of the ΔJ couplings. The propagation method defaults to solving the ordinary differential equations (ODE) in the way described above. However, the split step matrix method is also available. This method is described in chapter 6. The matrix method is sometimes faster for propagating through adiabatic pulses.

In the interface, suggestive default values are shown. This allows students to get an intuition of alignment dynamics without knowing the relevance of all the parameters. The intuition building is facilitated by the short calculation times. Typically, traces are delivered well within the attention span of a user.

3.3.1 Calculating abundances from nuclear spin statistics

Perhaps the least intuitive part of the user interface is the even and odd abundance fields. Abundance in this case refers to the naturally occurring abundance of even and odd *rotational states*. These have to do with nuclear spin statistics of inversion symmetric molecules, such as homonuclear diatomics. For molecules without inversion symmetry, the even and odd abundances are both 1. For molecules with inversion symmetry, the total wave function must be even under inversion of nuclear bosons and odd under inversion of nuclear fermions. The

total parity of the wave function is the product of the parities of the nuclear, vibrational, electronic and rotational wave functions. Assuming the vibrational and electronic states are even, the number of even and odd rotational states is then determined by the number of even and odd nuclear spin combinations. For a homonuclear diatomic molecule with nuclear spin S, there are $(2S+1)(S+1)$ inversion symmetric spin combinations and $(2S+1)S$ antisymmetric combinations. For example, the most abundant isotope of iodine, ^{127}I, has spin $S = 5/2$, and is thus a fermion. This means that there are 21 even and 15 odd nuclear spin combinations. The total wave function must be odd, so assuming the 21 even and 15 odd spin states are each equally likely, the even:odd abundance of rotational states is 15:21. The influence of nuclear spin on molecular spectra is described in many textbooks, e. g. section 11.5 in Ref. 76.

3.3.2 Remarks on practical usage of the calculator

Although the calculator is fairly intuitive, some important points may not be obvious. For example, it is easy to accidentally specify a basis size so large that the calculation takes unreasonably long time. To get an idea of the proper basis size to use, it is a good idea to calculate a trace only for the single state $|000\rangle$ with "#FVA shells" set to 1. For the given pulse, this gives the user a graph of $\langle J \rangle$ as a function of time, along with a graph of the 99.9 % percentile of the populated J states. A sensible $J_{\max}$ value is slightly higher than the highest point on the 99.9 % percentile curve. If a nonzero temperature is needed, the maximum J values should be adjusted according to the highest populated J state in the initial ensemble. Afterwards, thermal averaging can be enabled. When the basis size is big enough to support the thermal ensemble, focal volume averaging and calculation of $\langle \cos^2 \theta_{2D} \rangle$ can be enabled. In order to determine a reasonable number of focal volume intensity shells, the number should be increased until an increase no longer changes the calculated trace. Usually 20-30 shells seem to be enough. The computation time scales linearly with the number of shells. Generally, when trying to minimize the computation time, it is advisable to not calculate $\langle \cos^2 \theta_{2D} \rangle$, since doing so takes most of the time.

As stated above, when using long pulses, it is a good idea to also specify a longer time step. The time step is only for readout purposes. Internally, the wave function is automatically propagated in small enough time steps to ensure numerical stability. It is the calculation of expectation values that is most expensive. For long pulses, it is also advisable to start with a very low $J_{\max}$, since adiabatic pulses usually do not populate very high J states. The propagation of many basis states over a long pulse can easily take much longer than necessary.

3.4 Advanced usage examples

With the modular construction of the calculator program, the usage is not limited to what can be done from the graphical interface. For example, it is easy to fit

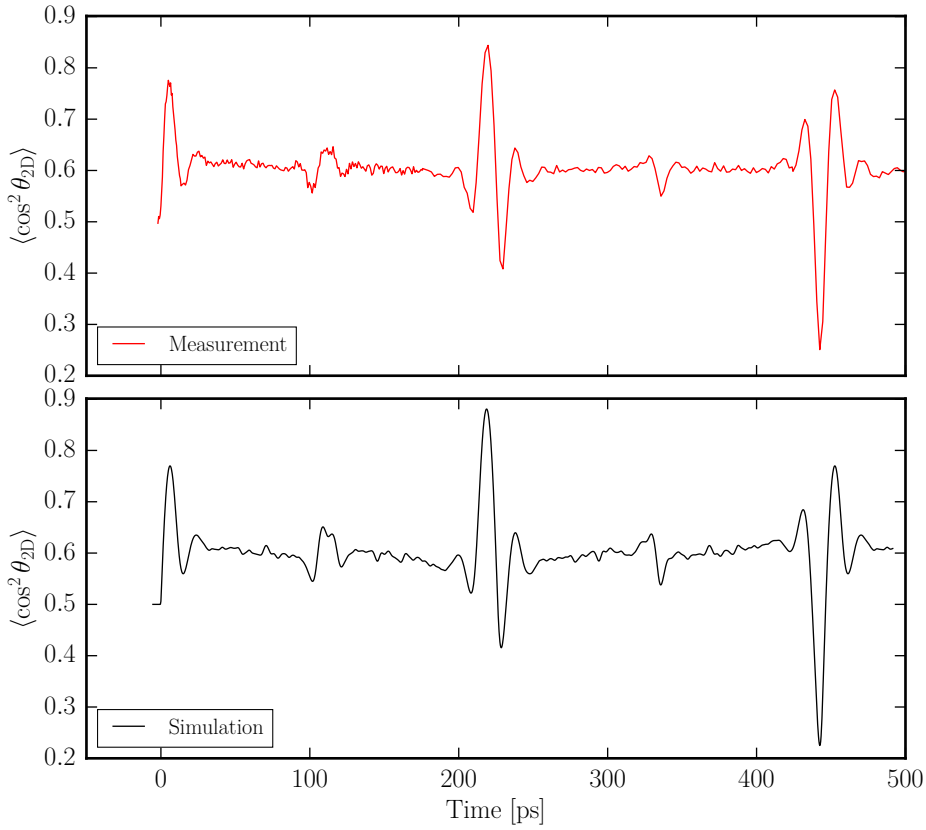

FIG. 3.3: Alignment trace of I_2 subject to a 2.7 TW/cm^2, 450 fs pulse. The top panel is the result of an experiment. The bottom panel is from a simulation, run at a fitted temperature of $T = 0.27$ K.

e. g. the temperature of the molecular beam. An example script for this purpose, `fit_temperature.py` is included in the calculator folder. The basic principle is to minimize the summed square error between the calculated and measured trace by varying e. g. the temperature. The high efficiency of the simulation implementation facilitates the fitting process. Note that the uncertainty of the fitted temperature depends on the uncertainty of e. g. the pulse specification. An example of such a fit is shown in Fig. 3.3. The upper panel shows a recorded alignment trace for I_2. Benjamin Shepperson and I carried out the experiment. The lower panel shows a simulation under the same conditions, where the trace is fitted to the one in the upper panel by varying the temperature. A remarkable agreement between the two traces is obtained. A temperature $T = 0.27$ K was obtained as a fitting result. With the Even-Lavie valve used in the experiment to

cool the molecules, a temperature lower than 1 K is expected [77]. Even so, 0.27 K seems unrealistically low since the molecules are seeded in helium during the supersonic expansion, and the helium droplet temperature is 0.37 K, indicating that the helium from the Even-Lavie valve should have condensed. As will be discussed in section 5.2.3, a more accurate temperature might have been obtained if the effects of centrifugal distortion had been taken into account. The sensitivity of the fitted temperature to changes in pulse parameters have also not been investigated.

The main difference between the experiment and the simulation is the maximum degree of alignment obtained for the half revival shortly after 200 ps. The simulation predicts a higher degree of alignment. The difference may partly be attributed to probe selectivity. As the molecules aligns with the pump pulse, the perpendicularly polarized probe beam Coulomb explodes fewer molecules. This effect was measured by Lars Christiansen and used as a way to characterize the degree of alignment from the ion yield [19].

A detailed comparison of the degrees of alignment reveals that many tiny peaks, or higher order revivals, also occur at the same time in the measured trace. Many seem in anti-phase, however. This could be due to centrifugal distortion, which is further discussed in section 5.2.3. Many of the fluctuations that are easily interpreted as experimental noise could turn out to be an actual signal. A better characterization of the experimental uncertainty of $\langle \cos^2 \theta_{2D} \rangle$ is needed.

A great, recent example of advanced usage is from what should have been a nearly adiabatic alignment experiment of I_2 molecules. This example is from preliminary work towards the publications [B1-B2]. In order to improve the repetition rate over an old Q-switched YAG laser, uncompressed pulses from a chirped pulse amplifier are used. While these pulses strictly are shorter than the rotational period of I_2, simulations, e. g. the one shown shown in Fig. 3.4a), indicate that the pulses still lead to nearly adiabatic alignment. However, when Benjamin Shepperson and Adam Chatterley did the experiment, it became clear from the resulting pronounced revivals, shown in the red curve in Fig. 3.4a), that the experiment is not as adiabatic as the simulations predicted. Benjamin and Adam then measured the cross correlation of the laser pulses with a 35 fs pulse. The cross correlation is scaled such that the fluence $F = 150\,\mathrm{J/cm^2}$ matches the pulse energy and spot size in the focus. The pulse, shown in Fig. 3.4b), is clearly not an ideal Gaussian. With a simple modification to the simulation program, propagation through the measured pulse is possible. The exact same simulation as in Fig. 3.4a), but using the measured pulse of Fig. 3.4b) is shown in Fig. 3.4c). As can be seen, the simulated and measured alignment traces are now in much better agreement. Certainly, no calculation of $\langle \cos^2 \theta \rangle$ could have even hoped for an agreement this good. As in the previous example, the disagreement is worst at the highest degrees of alignment, likely due to probe selectivity. The nonadiabaticity most likely stems from the two very steeply sloped rises of the pulse intensity in the beginning and towards the end of the pulse. After the experiment, the laser system was adjusted such that it again produces Gaussian pulses.

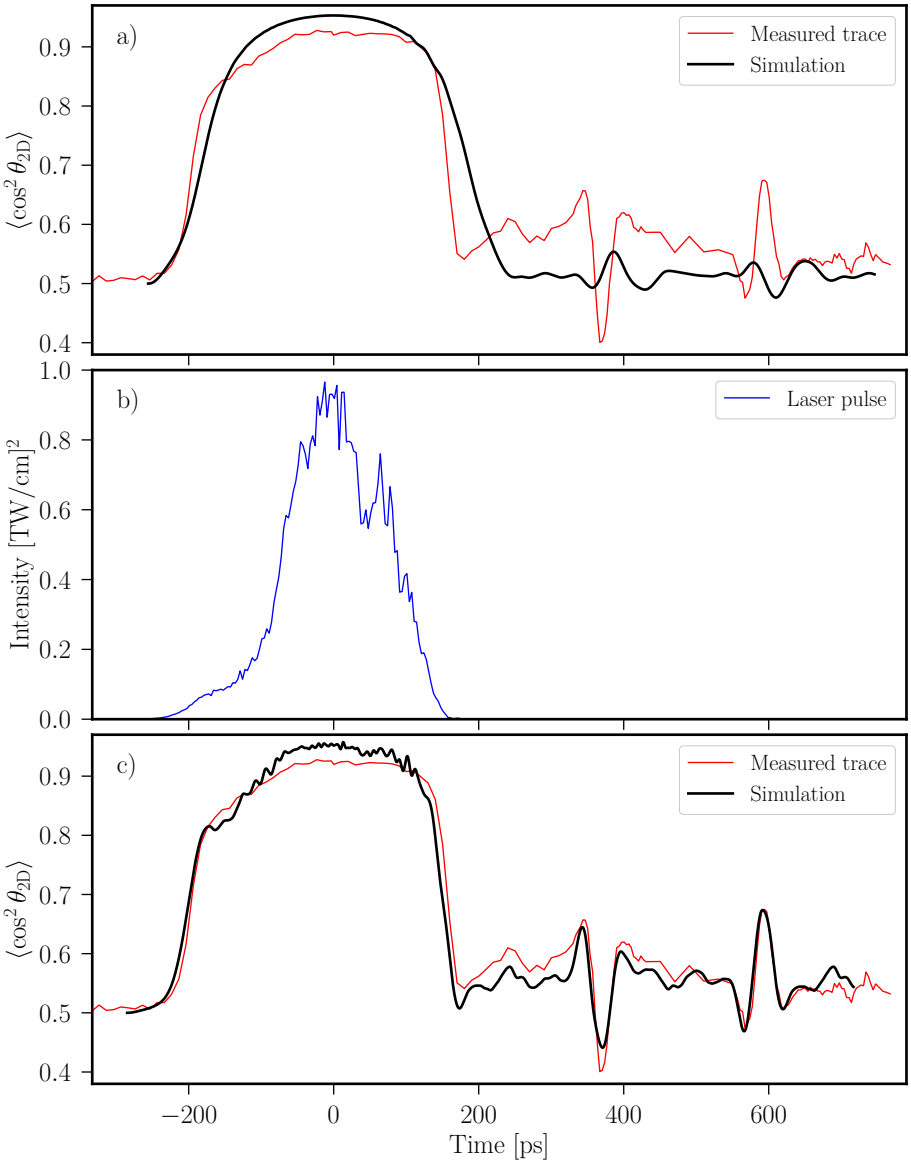

FIG. 3.4: Nearly adiabatic alignment experiment with I_2, using a 0.83 TW/cm^2, 170 ps pulse. Panel a) shows the measured alignment and a simulation for a 0.5 K initial ensemble using a Gaussian pulse. Panel b) shows the measured pulse. Panel c) shows the measured trace again, with a simulation for the same 0.5 K initial ensemble but using the pulse shown in panel b).

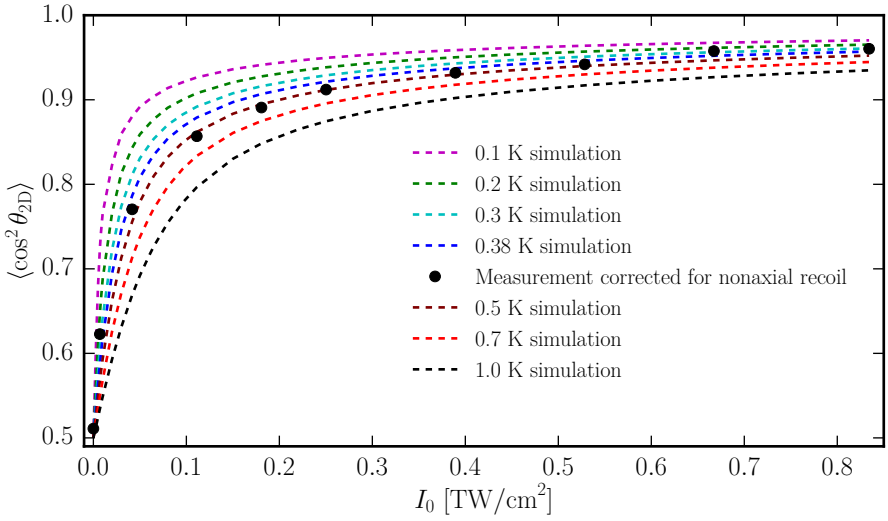

FIG. 3.5: Degree of alignment $\langle\cos^2\theta_{2D}\rangle$ of I_2 at the peak of a nearly adiabatic laser pulse as calculated by the simulation program (dashed lines) and as measured (black dots) in superfluid helium nanodroplets after correction of nonaxial recoil (see text). Figure data is from [B2].

The remarkable agreement between theory and experiment in the preceding examples not only demonstrates that the theory developed in chapter 2 is accurate. It also inspires renewed confidence in the quality of the experimental work. For example, the measurement of the strange pulse in Fig. 3.4b) becomes much more credible when it leads directly to an understanding of the observed alignment dynamics.

In a related experiment [B2] using the same pulse duration as in the previous example, Benjamin and Adam measured the maximum degree of alignment for I_2 molecules inside superfluid helium nanodroplets for various peak intensities I_0. The result, after deconvoluting the nonaxial recoil introduced by the helium droplet [55] is shown in Fig. 3.5. I wrote a simple script for iterating over intensities and initial temperatures which uses the calculator program to obtain the peak intensities shown as dashed lines in Fig. 3.5. It was Benjamin who used the script. As can be seen, the measured data shows that the initial temperature must be somewhere between 0.2 K and 0.5 K, which is consistent with a droplet temperature of about 0.37 K [14]. Between $\langle\cos^2\theta_{2D}\rangle = 0.85$ and about $\langle\cos^2\theta_{2D}\rangle = 0.92$ the experimental data seems to deviate towards the higher temperatures. The experimental results have not been corrected for probe selectivity, and the simulation does not take probe selectivity into account. If probe selec-

tivity had been accounted for, this deviation would likely not have been present. The probe prefers less aligned molecules since the probe and kick pulses are perpendicular. At the highest intensities, however, the angular distribution becomes so narrow that only a small, approximately constant part of the detection probability distribution is sampled. Thus $\langle \cos^2 \theta_{2D} \rangle$ at the highest peak intensities could be expected to give the best estimates of the initial temperature.

This last experiment constitutes the first measurement of the droplet temperature in Femtolab. It is probably also the first ever measurement of the droplet temperature that utilizes alignment of molecules.

In the examples, the effect of neglecting probe selectivity seems to have shown itself. A small, but noticeable discrepancy with the theory appears when the expected degree of alignment is between about $\langle \cos^2 \theta_{2D} \rangle = 0.85$ and $\langle \cos^2 \theta_{2D} \rangle = 0.92$. Nonaxial recoil has not manifested itself, since I_2 is diatomic and because the effect was removed from the droplet results. For I_2, probe selectivity seems to flatten out the alignment peaks, such that the measured degree of alignment is lower than the actual degree of alignment. It is still unclear exactly what the effect of probe selectivity is. A detailed study of these effects is clearly needed. With the ideas discussed in section 2.2.4 about calculating expectation values while taking both nonaxial recoil and probe selectivity into account, the goal of achieving a complete, quantitative understanding of both effects in combination seems like an encouragingly low-hanging fruit.

3.5 Summary

In summary, a versatile, user-friendly and highly efficient 1D molecular alignment calculator has been presented. The suggestive graphical interface and the high calculation efficiency invites the user, e. g. a student learning about alignment, to investigate the effects of changing relevant parameters. A student may in this way quickly gain an intuition of alignment dynamics. The effects of thermal and focal volume averaging have been discussed. Both effects tend to wash out structure in alignment traces. In this way, some information becomes lost. An experimental procedure for avoiding this loss of information has been outlined. A brief introduction to and remarks on practical usage of the calculator has been given. The audience of that part is mainly new users of the calculator. Through advanced usage examples, it has been demonstrated that the alignment theory developed in chapter 2 accurately describes real alignment experiments on iodine. The ease of use and efficiency of the calculator facilitates quantitative comparisons between experimental results and theoretical predictions. As has been demonstrated, this leads to an improved understanding of experimental results.

CHAPTER 4

Experimental setup

The experiments presented in this thesis were all performed using a very recent (completed summer 2015) He droplet setup and, unless otherwise noted, in collaboration with Benjamin Shepperson. The optical setup is described in section 4.1. The new droplet machine is presented in section 4.2.

Before the new machine was completed, I assisted Lars Christiansen and Benjamin with preliminary alignment experiments on CS_2 molecules using an older He droplet setup in the laboratory. It was through these experiments that I was introduced to the experimental methods and equipment employed in Femtolab. Later, but still before the new machine was built, I did experiments on isolated OCS molecules mostly on my own – again using the old setup. The results of those experiments will not be emphasized in this thesis, as the results obtained on the new machine encompass those of the old. They were, however, important, as they led me to do the simulations presented in chapter 6.

4.1 Optical setup

The optical setup is sketched in Fig. 4.1. The light source is a 35 fs Ti:Sa (800 nm wavelength) Spectra-Physics Spitfire-ACE-35F regenerative chirped pulse amplifier. The amplifier is seeded by a Spectra-Physics MaiTai SP and pumped by a Spectra-Physics Empower-45 Q-switched Nd:YLF laser. The seed laser has a repetition rate of 84 MHz, whereas the amplifier operates at a 1 kHz repetition rate. The final average power can be as high as 5 W, corresponding to 5 mJ per pulse, but only one third hereof was used for these experiments. The light source was shared with another experiment running concurrently in the other end of the laboratory.

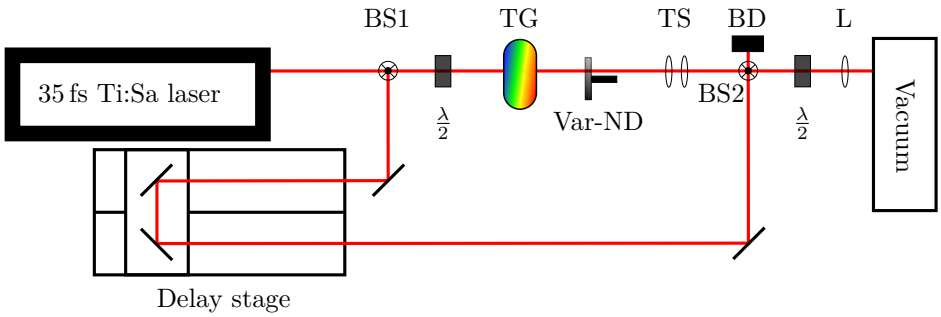

FIG. 4.1: Schematic diagram of the laser table setup. BS1 and BS2 are beam splitters, and BS2 is used to combine two beams. The $\frac{\lambda}{2}$ label refers to half-wave plates. These control the polarization of the laser beams. TG is a transmission grating pulse stretcher for controlling the pulse duration. Var-ND is a variable neutral density filter for attenuating the beam. TS is a telescope for controlling the spot size. BD is a beam dump and L is a 30 cm focal length singlet lens for focusing into the vacuum chamber. The unlabeled bars represent coated, ultrafast mirrors.

The output of the amplifier is split on a beam splitter BS1. The probe beam is sent onto a variable delay path (consisting of two delay stages: a Schneeberger R9800[1] followed by a finer-step but shorter Newport UTM 100PP.1 stage controlled by a Newport ESP300 universal motion controller) and recombined on a beam splitter BS2. The pump, or kick beam is sent through a half-wave plate into a transmission grating pulse stretcher TG. The frequency components are dispersed spatially and travel different distances before they are recombined by traveling backwards through the diffraction gratings. In this way, the pulse duration can be controlled. The pulse chirp is adjusted by varying the difference in path length. From the pulse stretcher, the kick beam goes through a variable neutral density filter Var-ND, such that the intensity can be controlled. The beam then encounters a telescope TS for controlling the spot size. In combination with the focusing lens L, this determines the final spot size of the focus in the target region. After the telescope, the kick and probe beams are recombined on a beam splitter, BS2. Half the power is dumped in the process. The combined beam then encounters another half-wave plate and the focusing lens before being sent into the target chamber. With the two half-wave plates, the linear polarization of the two beams can be fully controlled. The polarization of a beam is adjusted with the half-wave plates by minimizing transmission through a perpendicular polarizer.

Shortly after the vacuum chamber, the now diverging beams enter a Minioptic Delta single shot autocorrelator (not shown). By only allowing one beam through

[1] The delay introduced by the Schneeberger is only varied, in steps of 500 ps, when delays longer than 500 ps are required.

at a time, the pulse duration in each beam can be measured here. To ensure spatial overlap of the two beams in the focal region, a metal mirror is inserted immediately before the vacuum chamber. The light then passes through a dummy window of the same material and thickness as the one in the vacuum chamber. This ensures that the overlap outside the chamber is the same as inside. The foci are then characterized one at a time by scanning a 10 µm pinhole in front of a fast photodiode across the laser beams. In case the beams don't overlap, a mirror in one of the beamlines can be adjusted to move the focus of that beam. The delay stage is positioned as close to the vacuum machine as possible. Even so, it is hard to align the delay stage perfectly. The procedure of adjusting overlaps had to be done every few hundred scanned ps. Benjamin and I often discussed ways to automate this procedure, since doing so could potentially save a lot of time. The temporal overlap (informally "t_0") can be found in several ways. Since there is full control over the polarization in each beam, a method using a spectrometer was used here. This method, developed by Lauge Christensen and Anders Vestergaard Jørgensen [78], is significantly faster than e. g. looking for frequency doubled light generated in a nonlinear crystal. When the two beams overlap with the same polarization, they are virtually guaranteed to meet with different phases due to the tiny difference in path length. In this setup, dispersion is introduced in the pump beam to increase the pulse duration. Interference fringes in the frequency spectrum can then be seen when the pump and probe overlap in time. Ignoring third and higher order dispersion, the fringes become symmetric around the central frequency when the two pulses overlap perfectly. With a spectrometer positioned after the vacuum chamber, the temporal overlap is determined to within the uncertainty in stage position, or about 70 fs.

In order to compare experimental results to theoretical predictions, it is important to know the intensity of each pulse. If the pulses are assumed to have a Gaussian intensity profile (see equation (2.3) and (3.6)), the peak intensity I_0 can be calculated from the pulse energy E_{pulse}, the duration τ (FWHM) and the spot size ω with the formula [53]

$$I_0 = \frac{4\sqrt{\ln 2}}{\pi^{3/2}} \frac{E_{\text{pulse}}}{\omega^2 \cdot \tau}. \tag{4.1}$$

The pulse energy is simply the average beam power divided by the repetition rate. The experimental intensities reported in this thesis are all calculated with equation (4.1).

4.2 Droplet machine

The new machine, pictured in Fig. 4.2, consists of four separate vacuum chambers. These are the droplet source chamber, the doping chamber, the target chamber and the supersonic source chamber. The machine was designed and assembled by Benjamin Shepperson during my PhD project. In the construction phase, I have assisted Benjamin in the assembly and with the electronics. My most significant

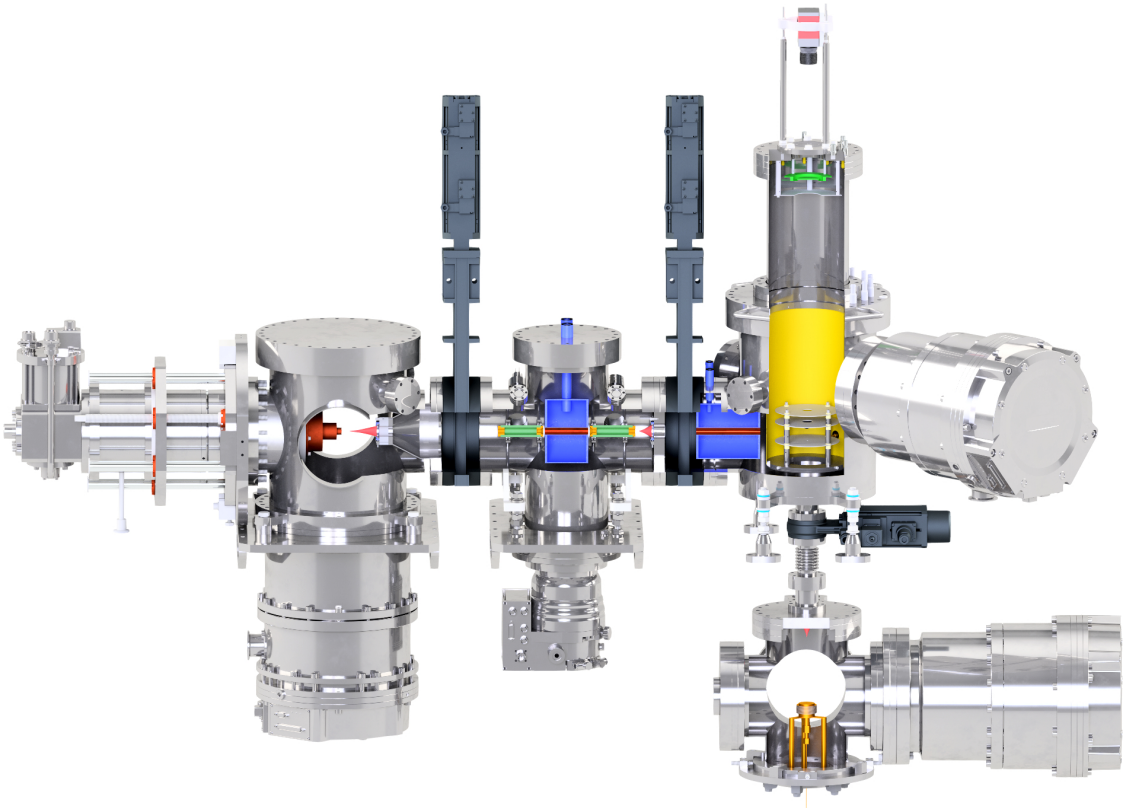

FIG. 4.2: Schematic of the droplet machine. The copper nozzle is attached to the cryostat in the droplet source chamber (left). After passing through a skimmer (red), helium droplets from the nozzle pick up molecules in the pickup cells (green) in the doping chamber (middle). Only the leftmost pickup cell is used in this PhD project. The droplet beam passes through another skimmer and two liquid nitrogen cold traps (blue) before entering the target chamber (top right) through a hole in the μ-metal shield (yellow). The supersonic source chamber below the target chamber houses the Even-Lavie valve (brass colored) for generating cold molecular beams. On top of the target chamber is the MCP detector (green) and a CCD camera (outside). The laser beams pass through another small hole in the μ-metal shield and overlap both the droplet and molecular beams in the center between the two lowest VMI capacitor plates (surrounded by the μ-metal). Each chamber is evacuated by its own turbomolecular pump. The schematic was designed by Benjamin Shepperson and prepared for display by Benjamin and Mette Rasmussen.

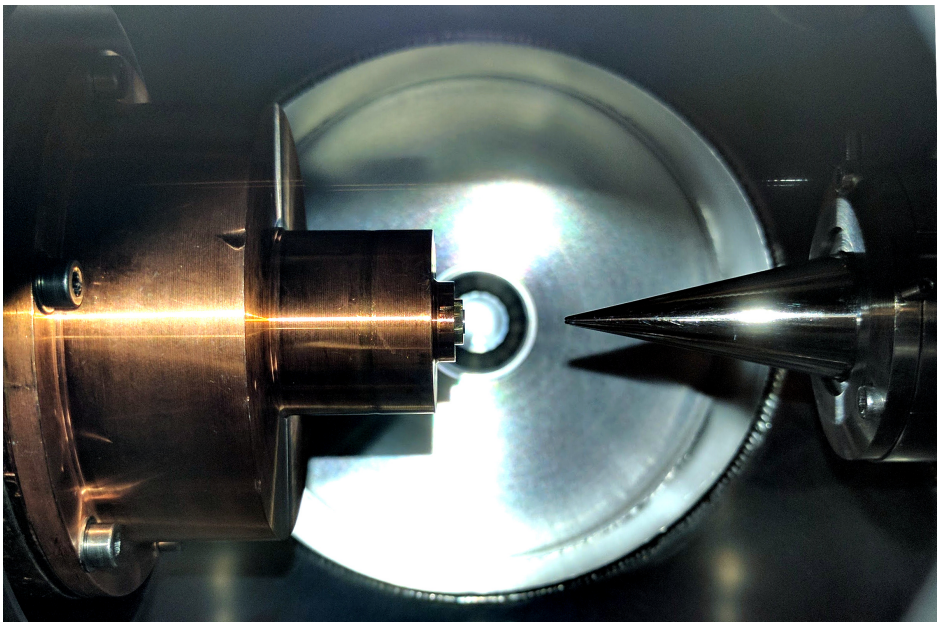

FIG. 4.3: Inside view of the droplet source chamber while the machine is operating. The outer copper shield is cooled to roughly 50 K. The nozzle inside is cooled to 14.00 K. The separation between the tips of the nozzle and the skimmer is roughly 2 cm.

contribution in the construction of the machine was to improve the temperature stability of the droplet nozzle by introducing two stainless steel plates between the cold head and the nozzle. These plates act as thermal insulators, and dampen out the powerful cooling cycle of the cryostat. In this way, the temperature stability improved from ± 0.5 K to ± 3 mK at 10 K at a cost of a slightly larger minimum nozzle temperature. I also advised Benjamin to open up the back-end of the pickup cells to reduce the number of molecular trajectories leading to a contaminating effusive background signal. One design goal was to minimize this effusive beam as much as possible.

The 0.6 mm thick 2-mm-diameter platinum iridium nozzle with a 5 µm aperture, shown in Fig. 4.3, resides inside the droplet source chamber. The nozzle is cooled to cryogenic temperatures with a closed cycle cryostat (Sumitomo Heavy Industies (SHI) Cryogenics RDK-415D 4K pumped with a SHI F-50H compressor). The temperature is regulated by heating up two resistors (Farnell MHP35470F 47 Ω 1 % 35 W) attached to the nozzle with a Lakeshore Cryogenics 335 temperature controller. The temperature is measured with a sillicon diode (LakeShore DT-670B-CU). Helium droplets are produced by continuously expanding high-purity (6.0) helium gas at a stagnation pressure of 25 bar through

the nozzle. With a nozzle temperature of 14 K, this leads to production of droplets consisting of on average 7×10^3 helium atoms [15]. These conditions are used in all of the droplet experiments presented in this thesis. The droplet size distribution follows a log-normal distribution, and thus becomes very broad for larger droplets [79]. After expansion into the vacuum, the droplets form and very quickly ($\sim 10^{-4} - 10^{-3}$ s) cool down to 0.37 K through evaporation of helium atoms. This was predicted [51] by using the liquid drop model [80, 81] that is also used in nuclear physics to e. g. calculate "evaporation" (i. e. nuclear decay) rates of neutrons in excited nuclei. The predictions are in good agreement with experiment [52]. In chapter 3, the droplet temperature in this machine is confirmed to be around 0.4 K. This was measured by comparing $\langle \cos^2 \theta_{2D} \rangle$ of I_2 molecules in a (nearly) adiabatic experiment with $\langle \cos^2 \theta_{2D} \rangle$ predicted by the theory in chapter 2. Each evaporated atom carries away at least the binding energy, which is about $7\,\mathrm{K} \cdot k_b$, or $5\,\mathrm{cm}^{-1}$. The speed of the droplet beam is about 300-400 m/s [82].

After expansion through the nozzle, the helium droplets pass through a 1-mm-diameter skimmer to collimate the droplet beam. The droplets then enter the doping chamber (see Fig. 4.2). Here, they pass through a 7.4 cm long cylindrical, coaxial pickup cell with an inner diameter of 1.4 cm. The cell is filled with a low pressure gas of the molecule of interest. The droplets pick up molecules from this gas since the Landau velocity is much smaller than the relative velocities of the droplets and the thermal molecules. The probability that a droplet picks up k molecules follows a Poisson distribution [15]

$$P_k = \frac{(\alpha L)^k}{k!} \exp(-\alpha L). \tag{4.2}$$

Here L is the length of the pickup cell and $\alpha = \rho\sigma$, where ρ is the number density of the gas and σ is the droplet cross-section. The pickup cell pressure, and thereby the molecular number density, is controlled with an adjustable leak valve (Kurt Lesker VZLVM940R). The pressure is adjusted such that the droplets primarily pick up none or a single molecule. Dimers can be detected e. g. in the mass spectrum. For I_2, a particularly simple way of detecting dimers is to look at the I^+ ion images taken with the probe pulse only, polarized in the plane of the detector. Dimers lead to a perpendicular (oval shaped) channel, which is absent for the monomers. In the I_2 experiments, the pressure is lowered until this perpendicular channel vanishes. This gives a detection rate of on average only one event per 20 laser shots, i. e. about 50 events per second.

After the pickup cell, the droplet beam travels through a 4-mm-diameter cylindrical hole in a stainless steel barrel filled with liquid nitrogen. The nitrogen is isolated from the vacuum by the stainless steel walls. This barrel acts as a cold trap, stopping unwanted unsolvated molecules from entering the target chamber. A second pickup cell after the cold trap allows for sequential doping. This cell is empty in the experiments presented in this thesis. At the end of the pickup chamber is another, 2-mm-diameter skimmer, followed by a second, smaller liquid nitrogen barrel with 4-mm-diameter cylindrical hole. This barrel is inside the target chamber. In the center of the target chamber, the droplet beam

is crossed by the two focused laser beams described above. The intersection of the beams is in the center of a velocity map imaging (VMI) spectrometer [83], which will be discussed below.

Below the target chamber is the supersonic source chamber. Here, a pulsed Even-Lavie valve (EL-7-4-2011-HRR, 600 Hz) produces a beam of cold (<1 K) isolated molecules [77]. The valve is operated at 100 Hz. Depending on the molecule, the sample is either placed inside the valve or in the supply line leading up to the valve and isolated from the metallic walls with fiber glass filter paper. Helium carrier gas at a stagnation pressure of 80 bar drives the sample vapors towards the valve opening, where the gas undergoes supersonic expansion into the vacuum. To control the pulses molecular density, the valve can be heated to increase the vapor pressure of the sample. The molecular beam passes a 3-mm-diameter skimmer before it enters the target chamber. In the I_2 experiments, the molecular density usually gave detection rates of about 50 events per repetition, or about 5000 events per second.

All of the chambers can be isolated with pneumatic gate valves (VAT). This allows control (blocking) of the droplet beam, such that e. g. the effusive beam from the pickup cell can be characterized. Likewise, the background conditions can be measured by isolating the target chamber. The isolation valves also allow the chambers to be vented independently.

Each chamber is pumped with its own turbomolecular pump. All of these turbos have magnetic bearings. The need for potentially contaminating bearing grease is thus eliminated. The turbos for the target and doping chambers are both backed by the same dry pump (Busch Vacuum BA 100 “Cobra”). The turbos for the droplet- and supersonic source chambers are both backed by an Edwards IGX 600L dry pump. The two backing pumps each evacuate their own manifold, to which the turbo exhaust lines are connected. The turbo pumping capacities (quoted for nitrogen) are 2200 L/s for the droplet source chamber, 450 L/s for the pickup chamber, 1100 L/s for the target and supersonic chambers. The turbo pumps on the target and supersonic chambers are capable of 1600 L/s, but are mounted on reduced flanges (CF 160).

The pressures inside the chambers are monitored with Vacom Atmion ATS40C full range ionization pressure gauges. Under droplet beam experiments with the cold traps filled, the pressures in droplet source, pickup and target chambers are roughly 3×10^{-4} mbar, 2×10^{-6} mbar and 1×10^{-8} mbar, respectively. Under the gas phase experiments with the cold trap in the target filled, the pressure in the supersonic source and target chambers are 1×10^{-5} mbar and 6×10^{-8} mbar, respectively.

4.3 Detection system

The laser system supplies a 1 kHz main electronic trigger signal. This trigger signal is relayed with a finely controlled delay by a Stanford Research delay generator DG535. The delay generator distributes the individually delayed trigger

signals to the Even-Lavie valve, an oscilloscope, a CCD camera and a fast, high voltage switch.

The molecular beam pulses from the Even-Lavie valve are synchronized to the laser pulses by varying the valve delay introduced by the delay generator. The delay is typically a few hundred microseconds, and is chosen such that the detected signal is maximized.

The molecular or droplet beams intersect the laser beams in the middle between the repeller and extractor plate electrodes of a velocity map imaging (VMI) spectrometer [83]. Experiments on isolated molecules and molecules in helium nanodroplets can thus be done under exactly the same conditions. The 1 mm thick plates are 3.5 cm apart. The droplet beam enters between the repeller and extractor plates from the side, and the molecular beam enters the VMI through a 3-mm-diameter hole in the center of the repeller plate. A voltage gradient of about 0.6 kV/cm accelerates charged particles through a 20 mm hole in the center of the extractor plate, and through a 20 mm hole in the grounded plate 20 mm after the extractor plate. The particles travel about 47 cm while diverge according to their initial velocities. The flight path is shielded from stray magnetic fields by a cylindrical sheet of μ-metal. After the flight, the particles impinge on a 2D position sensitive microchannel plate (MCP) detector (El-Mul Technologies B050V, chevron MCP with a 38 mm active diameter). The charged particles break loose electrons in the detector metal. These electrons are amplified across the detector by a 1800 V difference between the front and back of the detector. A phosphor screen behind the MCP lights up when it is hit by the amplified electron cascade. The phosphor screen is at a 2300 V higher potential than the back of the MCP. A CCD camera (Allied Vision Prosilica GE680) records the positions of light spots on the phosphor screen. After choosing the correct ratio of extractor to repeller voltages ("focusing the ion lens"), a given position on the detector corresponds to the projection of the particle velocity vector onto the plane of the detector [83]. The correct ratio is determined by focusing ionic species with low initial velocity (compared to the velocities obtained after Coulomb explosion) onto a single pixel. In the experiments presented in this thesis, H_2O^+, created from the background gas was used in the focusing procedure. In all of the gas phase experiments presented in this thesis, the repeller and extractor voltages are 3800 V and 6000 V, respectively. In the droplet experiments, the ejected ions move slower, and thus require a larger magnification. In those experiments, the repeller and extractor voltages are 3170 V and 5000 V, respectively. The voltage ratios, and thereby the focusing remain the same.

The camera is not fast enough to resolve arrival times of the many charged species created by the laser pulse. In order to only image a single species, the detector is gated by temporarily lowering the voltage on the front of the detector when the particle of interest arrives. At other times, a voltage difference of only 1300 V is maintained. When the voltage isn't lowered, the detector doesn't amplify the electrons generated by other species. The voltage is lowered by 500 V for a few hundred ns with the fast, high voltage switch. The switch timing is controlled by varying the delay introduced by the delay generator. The switch

is fast enough to discriminate single ions. In the experiments presented in this thesis, the switch opens the gate for a duration of 160 ns.

In order to determine the arrival time of the individual charged species, the VMI spectrometer can be turned into a time-of-flight (ToF) spectrometer by grounding the phosphor screen and the front of the MCP, while leaving the back side at 1800 V. The back-end of the MCP is connected to an oscilloscope (Lecroy Wavesurfer 64MXs-B 600 MHz, 10 GS/s) through a high-pass filter. The filter serves to protect the oscilloscope from the 1800 V (DC) supply voltage. The amplified electrons cause a brief voltage drop which is measured by the oscilloscope. The time-of-flight of a charged particle is determined by its mass m and charge q and other external factors such as the plate voltages and the flight distance. If the particle starts with zero velocity, the arrival time $t \propto \sqrt{m/q}$. If the particles have nonzero initial velocity, the ToF signal is broadened. With all the external factors held constant, the mass-to-charge ratio $r = m/q$ of each detected species can be determined after calibrating the spectrometer. Calibration can be done e. g. with the $(H_2O)^+$ and H^+ channels from the background gas in the isolated target chamber. A complete characterization of the detected species and the fragmentation channels of the molecules can typically be obtained from the mass to charge ratios. Impurities such as hydrocarbons, water, nitrogen and oxygen can likewise be identified. Of these, $(H_2O)^+$ is most often the strongest channel. The contribution from impurities is minimized by "baking" the chambers, i. e. by heating the chambers up over a few days before the experiment. The heat leads to higher desorption rates from the chamber walls, allowing the impurities to be pumped away more rapidly.

The repetition rate of an experiment is limited by the combination of electronic devices involved in the experiment. The Even-Lavie valve operates at up to 600 Hz, but due to limited pumping capacity, it is operated at at most 200 Hz. In the experiments presented in this thesis, the valve is only operated at 100 Hz. At 100 Hz and with the signal intensities recorded, the speed of the delay stage becomes the limiting factor.

The molecular density in the droplet beam is so small that much fewer events are detected per laser shot. In these experiments, the camera shutter is open for the duration of 10 laser shots, giving an effective repetition rate of the full 1 kHz of the laser system. With the longer opening time, it becomes necessary to eliminate ambient room light. This is done by wrapping a black piece of cloth around the camera and the rods connecting the camera to the target chamber. The long shutter opening time causes a few of the pixels to always light up. In the droplet experiments, only two pixels were faulty, and are not included in the analysis. In the ToF measurements, only the oscilloscope limits the repetition rate. Depending on the oscilloscope and the mode of operation, the full 1 kHz rate can be obtained.

The camera images and oscilloscope measurements are sent over a 1 gigabit/s ethernet connection to a computer. Here, the images are compressed online with a hit-finding routine. Only the coordinates of each lit pixel is stored. Offline analysis of the compressed images can be done any time after the acquisition.

CHAPTER 5

Alignment of molecules inside superfluid helium nanodroplets

A qualitative and quantitative understanding of 1D laser-induced alignment of isolated symmetric top molecules was attained in chapters 2 and 3. The apparatus for experimental investigation of molecular alignment was described in chapter 4. With the same setup, the nature of rotation and alignment of molecules inside superfluid helium nanodroplets can be examined. The stage has thus been set for the central topic of this PhD thesis.

Below, in section 5.1, a brief account of the previous results of nonadiabatic alignment of molecules inside helium nanodroplets is given. In section 5.2, new experimental results on alignment of I_2 molecules inside helium nanodroplets are presented. The results show qualitatively new, never observed before alignment dynamics. Together with the theory presented in chapter 6, these results lead to an improved Understanding of Laser-Induced Alignment and Rotation of Molecules Embedded in Helium Nanodroplets.

The results presented here forms the basis of a manuscript in preparation [A2].

5.1 Historical perspective

The results from rotationally-resolved IR spectroscopy mentioned in chapter 1 show that the free rotation of molecules in helium nanodroplets is unimpeded by the presence of the liquid. Only a small increase of the moment of inertia is introduced by a nonsuperfluid solvation shell adiabatically following the molecular rotation. The rotationally-resolved IR spectra of molecules in droplets are reproducible with the theory for isolated molecules where the moment of inertia is adjusted accordingly.

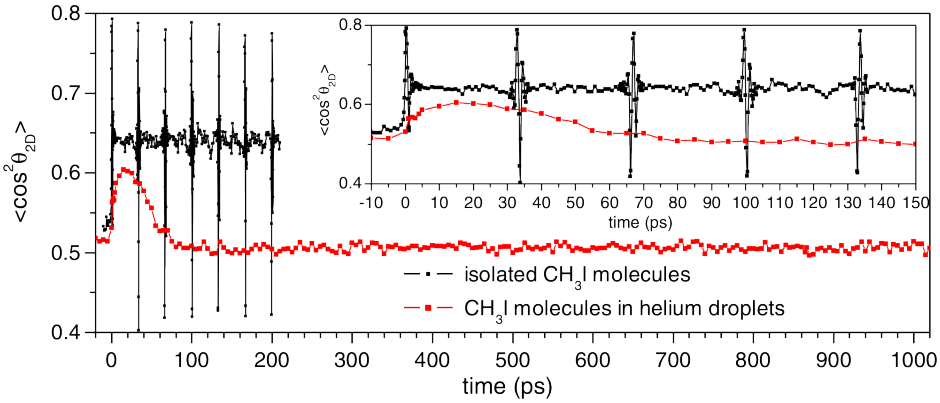

FIG. 5.1: The measured degree of alignment $\langle\cos^2\theta_{2D}\rangle$ of isolated CH_3I molecules (black squares) and of CH_3I molecules in He droplets (red squares) under identical conditions as a function of time after the alignment laser pulse. The alignment pulse parameters are $I_0 = 12\,\mathrm{TW/cm^2}$ and $\tau = 450\,\mathrm{fs}$. The inset shows the same data in a narrower time window. Excerpt from Ref. 17

When the rotation is induced by an ultrashort, intense, nonresonant laser pulse, the results are strikingly different. Here, the molecules are no longer free to rotate, and the theory for isolated molecules, presented in chapter 2, no longer reproduces the observed rotational dynamics. This is demonstrated in Fig. 5.1. Methyl iodide (CH_3I) molecules are aligned both in the gas phase and in helium nanodroplets. The isolated molecules align at regularly spaced intervals in a way that is fully consistent with the theoretical description given in chapter 2. This description is clearly not adequate for understanding alignment of molecules inside droplets. The molecules align on a significantly slower time scale that is not consistent with a small increase in the moment of inertia. After the initial alignment, the revival structure is completely absent, and a permanent alignment level $\langle\cos^2\theta_{2D}\rangle = 0.5$ is reached after about 100 ps, indicating that the molecules become randomly aligned. From Fig. 2.3 on page 25, it is seen that any $\langle J00|\cos^2\theta_{2D}|J00\rangle$ matrix element with $J > 0$ is larger than the one for $J = 0$. Thus the permanent alignment level must be strictly larger than 0.5 if any excited state is present, even if the coherence becomes lost or changed. See the discussion on page 24 about the permanent alignment level and the diagonal matrix elements following the Fourier series (2.35). Loss of coherence manifests itself in a loss of revivals, since it is the coherence that ensures the periodicity of each off-diagonal contribution and the resulting beat pattern. The above argumentation is also valid for the KM states that are populated at the droplet temperature (although here the equal population of the initial M states due to equipartition must be invoked – the matrix elements average to 0.5). The only other way a decay of the permanent alignment level is conceivable is if M (or K) is no longer a conserved quantum number, i. e. the helium somehow (e. g. via

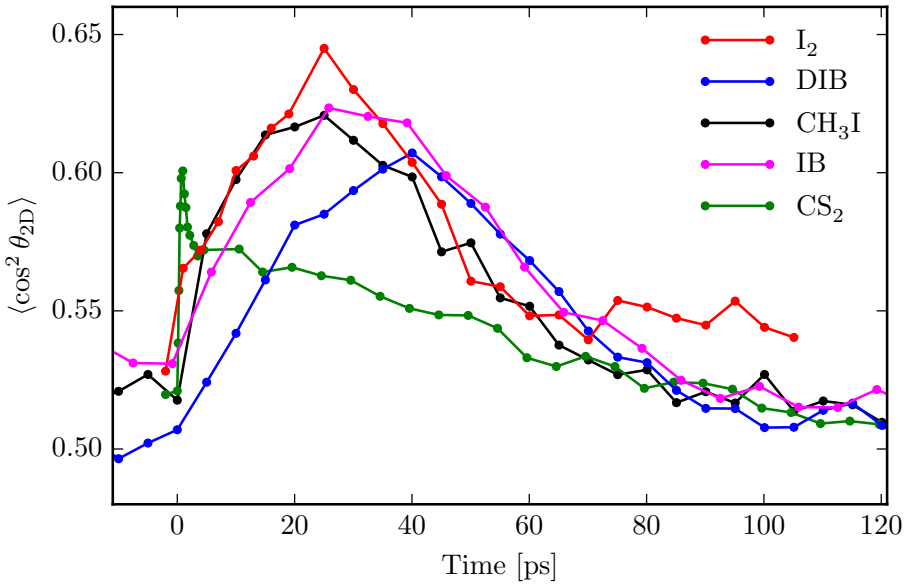

FIG. 5.2: Alignment traces for a variety of molecules inside helium droplets. DIB refers to 1,4-diiodobenzene, and IB refers to iodobenzene. Excerpt from Ref. 18

collisions) mixes M states on this extremely short time scale. It seems more than likely that the lifetime of the rotational states in the methyl iodide experiment is simply much shorter than the few nanoseconds determined from the linewidths in the rotationally resolved experiments on e. g. OCS (see Fig. 1.4 on page 7).

The same can be said for other molecules that have also been investigated in Femtolab. The same qualitative behavior is seen e. g. for the molecules shown in Fig. 5.2. Of the results shown here, I have only contributed to the experimental work for CS_2. The CS_2 result stands out, as it is the only molecule that exhibits any fast rotational dynamics. However, this rotation is "too fast", i. e. it almost matches the case of the isolated molecule perfectly, at least when only the first few ps are considered. This is also in disagreement with the expectation that the moment of inertia is modified by a factor of roughly 3 [15]. Is this a sign of cavitation, i. e. does the rotating CS_2 molecule punch a hole in the liquid, continuing in free rotation until the cavity collapses?

5.2 Alignment of I_2 molecules

Previously, I_2 molecules were aligned inside helium droplets (see Fig. 5.2), but showed similar behavior to that of other molecules. The results for CS_2 molecules motivated the development of the model presented in chapter 6, which in turn

motivated the new study on I_2 molecules presented here. The results of the modeling indicate that I_2 should show new behavior if the kick strength [59] is lowered compared to the kick strengths used previously. Here, new experimental results are presented for alignment of I_2 molecules in helium nanodroplets.

5.2.1 Isolated I_2

In order to show that the experiment works reliably, the experiment is first performed on isolated molecules under the same conditions that will be used in the droplet experiments. This also enables a direct comparison between the alignment dynamics of free molecules and molecules in helium nanodroplets.

The Even-Lavie manual advises against putting iodine in the valve as I_2 is corrosive. To avoid corrosion damage of the expensive valve, the sample was initially placed in the stainless steel helium supply line (Swagelok). From here, the vapors never reached the valve, however. To increase the vapor pressure, the iodine sample in filter paper inside the stainless steel pipe was heated with a heat gun. This very quickly caused severe corrosion damage to the supply line. To do the experiment, iodine had to be put inside the Even-Lavie valve sample holder. By keeping the valve parts and the iodine sample dry at all times and well isolated with glass filter paper, corrosion damage was avoided. The sample was inside the valve only long enough to record the experimental data. The valve was run at 30 °C, close to the lowest stable temperature of the valve. Corrosion inside the stainless steel sample holder for the droplet doping chamber also occurred after less than a week, when the sample was left under vacuum at room temperature.

The molecular axis distribution as a function of time is determined by Coulomb exploding the molecules with a 35 fs, 430 TW/cm^2 probe laser pulse at a controlled delay after the kick pulse. The probe spot size[1] is $\omega_p = 20\,\mu m$ and the kick spot size is $\omega_k = 35\,\mu m$. The 2D velocity distribution of the resulting I^+ ions are recorded with the VMI, described in section 4.3. The molecular axis distribution is approximated with the emission direction of the I^+ ionic fragment from the Coulomb explosion. For the isolated, diatomic I_2 molecules, the recoil can only happen along the bond axis. However, probe selectivity (see section 2.2.4) can still skew the axis distribution slightly. In the droplets, nonaxial recoil does occur for I_2 due to collisions with the helium atoms.

Examples of I^+ ion images for isolated molecules are shown in Fig. 5.3. From the recorded images, the degree of alignment $\langle\cos^2\theta_{2D}\rangle$ in panel f) is calculated as the average over $\cos^2\theta_{2D}$ for the individual ion hits (see section 2.2). A randomly aligned sample has $\langle\cos^2\theta_{2D}\rangle = 1/2$, a perfectly aligned sample has $\langle\cos^2\theta_{2D}\rangle = 1$, and a perfectly anti-aligned sample has $\langle\cos^2\theta_{2D}\rangle = 0$.

The degree of alignment is calculated only with the ion detections that fall between the white circles at radii 100 and 180 pixels, shown in panel b)-e). This radial range captures most of the I^+ ions born with an I^+ partner. This is clear from covariance analysis, which shows that when one I^+ ion is detected in the

[1] See equations (2.3) (3.6), (3.7) and (4.1).

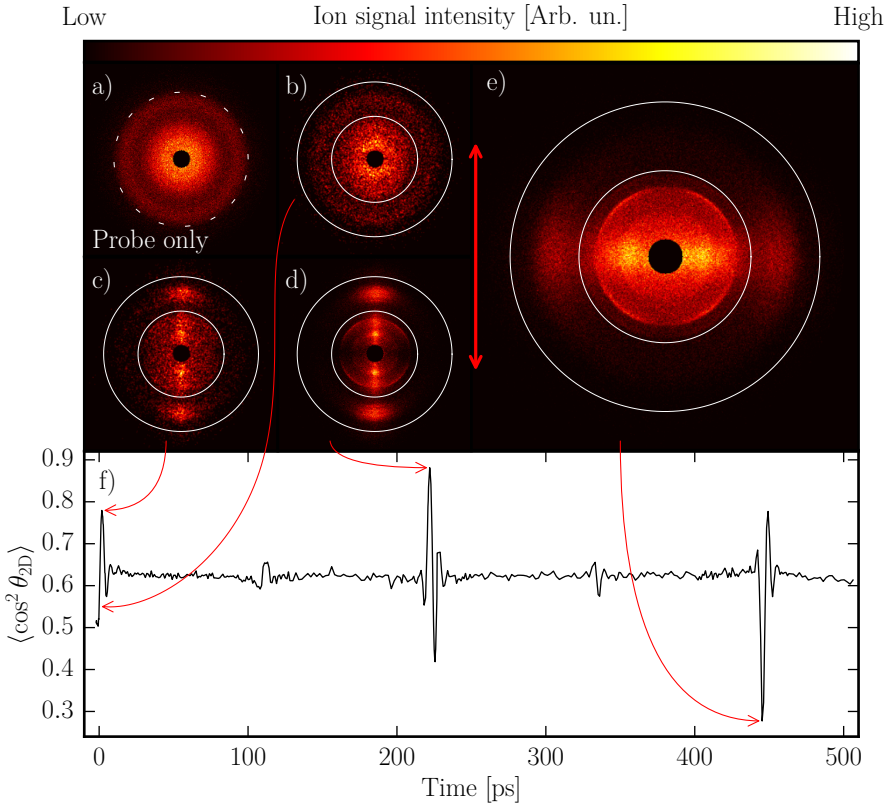

FIG. 5.3: Examples of I^+ ion images a)-e) used to determine the degree of alignment $\langle\cos^2\theta_{2D}\rangle$ in f) as a function of the delay between the kick and probe laser pulses. The kick pulse was blocked while recording image a). Images b)-e) are recorded after a 450 fs kick pulse with a peak intensity of 8.0 TW/cm^2. Each image is 451 × 451 pixels, corresponding to 36 × 36 mm^2 on the detector. The images are scaled individually to their maximum value to get all images on the same scale. The arrows indicate the timing and $\langle\cos^2\theta_{2D}\rangle$ of each image. The double-pointed arrow indicates the polarization of the kick pulse. The probe pulse is polarized perpendicularly to the image plane. The number of detected ions in panel b) and c) is too low to clearly show the distribution, so for display, these images have been smoothed with a Gaussian filter with a standard deviation of 1 pixel. The ion detections in the center have been artificially removed, since the strong signal here would break the color scale.

range, another I^+ is simultaneously detected in exactly the opposite direction (to within 2 pixels) at roughly the same distance from the center. I^{++} ions rejected by the gate. The spectrometer has not been calibrated. However, since I^+ was measured to have a flight time of 6.24 µs, and the camera records 12.4 pixels / mm of the detector, a simple calculation allows for estimation of the recoil speed. Assuming that I_2 breaks into two I^+ ions and that all the electrostatic energy

$$U = \frac{1}{4\pi\varepsilon_0}\frac{e^2}{d} \tag{5.1}$$

is converted to kinetic energy at the instant of the probe pulse, it is found that the I^+ ions from a molecule aligned with the plane of the detector must arrive at 156 pixels from the center. Here, the I_2 bond distance $d = 2.666$ Å is inserted, and e is the elementary charge. A more detailed integration[2] gives the same radius to within the uncertainty. This radius is indicated by the thin, white dashed circle in the probe only image in panel a). The fact that the calculated radius coincides with the observed sharp cut-off in the signal intensity is another strong indication that the selected radial range captures I^+ ions that are born with an I^+ partner. According to the same calculation I^+ ions created with an I^{++} partner should hit at a radius of 221 pixels, which is just within the limits of the shown images. Thus the I^+-I^{++} channel is seen to be negligible.

Two inner channels can be seen e. g. in panel d). As can be seen from the images in b) and c), these channels takes time to build up, and they apparently start out at higher radii. This fact and the characteristic shape [18] is consistent with the interpretation that these channels are caused by dissociation into I-I^+ and uncharged I-I pairs, that gain charge by the Coulomb explosion pulse (and thus have constant velocity after sufficient time for separation before the probe pulse). Such dissociation channels do not represent rigid rotation, and the inner radii are therefore excluded from the analysis. For reasons that are not yet understood, however, the dissociation channel exhibits alignment at the same time as the Coulomb explosion channel, as seen in Fig. 5.3d), and what looks like anti-alignment (or possibly an octopolar shape) in panel e). The dissociation is due to a low dissociation threshold of I_2 (12 441 cm^{-1}) [84]. Although the absorption cross section is low at 800 nm [85] the kick pulse still dissociates a small fraction of the molecules and leads to the time-dependent structure in the radial distributions.

In the images a)-e), the central portion has been cut out, as a highly localized signal arising from the doubly charged I_2^{++} molecular ion gives a disproportionately large, few-pixel signal intensities. These molecular ions, that have a lifetime longer than the flight time [86], have the same mass to charge ratio as I^+. Thus they are also detected while the detector gate is opened. They localize in the center because they are born without any significant velocity, however.

[2]The reader may be interested in the classical Coulomb explosion simulation program that I wrote. The program calculates 3D trajectories of charged, rigidly rotating molecular fragments and is designed for investigating deviations from axial recoil. The program can be found at https://github.com/andersas/nbody-coulomb.

Since the inner radial ranges have been cut out, the directions of molecules pointing in the direction of the detector are not recorded. This gives a small, and apparently negligible bias in favor of higher degrees of alignment.

5.2.2 I_2 molecules in helium nanodroplets

Examples of ion images from the same experiment performed on I_2 molecules in helium droplets are shown in Fig. 5.4. The only difference is the plate voltages. These must be lower, as the I^+ fragments are slowed by the droplet. Nevertheless, the ratio of the plate voltages have been kept the same. Furthermore, as this is just an example, the images are shown for a different kick pulse. However, each pulse configuration for the isolated molecules is also used in the droplet experiment and vice versa.

The I^+ fragments can pick up a small amounts of He atoms on the way out of the droplet [87]. In these experiments, the gate was set to select IHe^+ complexes, as this allows for completely background-free detection. There are no other species present with the same mass-to-charge ratio.

The degree of alignment is again calculated for the ions falling between the white circles, now at radii 55 and 180 pixels (see Fig. 5.4 panel b)-e)). There is a slight left-right asymmetry inside the inner circle due to a small, damaged area on the detector where the detection efficiency is reduced. Given that a time-of-flight of 6.87 µs was measured for IHe^+, and neglecting the influence of the droplet on the velocity, IHe^+ is expected to hit within a radius of 172 pixels. This radius is again indicated by the white, dashed circle in panel a). Clearly, the droplet slows down the ions. Under the liquid drop model [51], the droplet radius is $R = r_0 N^{1/3}$, where $r_0 = 2.22\,\text{Å}$ is an effective atomic radius of helium and $N = 7 \times 10^3$ is the number of helium atoms in the droplet. With these numbers and assuming that the ions in the worst case only travel at the Landau velocity, the escape time $t_e < 0.1\,\text{ns}$ is significantly lower than the time-of-flight and thus has no influence on the result. I.e the time-of-flight used in the calculation is essentially the same regardless of the influence of the droplet. The droplet peak seems to die out at a pixel radius of around 115 (indicated by a blue dashed circle in Fig. 5.4a)). This corresponds to an initial (2D) speed of 1.3 km/s, which is well above the Landau speed.

Although the measurement is background-free, there is again at least one dissociation channel present (see Fig. 5.4). The channel builds up over the first few ps. As in the gas phase, this channel is eliminated from the analysis. It is noted, however, that the channel exhibits apparent, roughly constant alignment as far as to the limit of 1.5 ns where no further measurements were performed. This apparent alignment most likely does not indicate stably populated rotational states, but is rather due to dissociation effects.

The recorded alignment trace in 5.4 f) exhibits the slow dynamics previously seen for e. g. I_2 or CH_3I molecules (see Fig. 5.1 and 5.2). In contrast to the previous results for I_2, the trace here also exhibits fast dynamics initially, resembling somewhat that of CS_2 in Fig. 5.2.

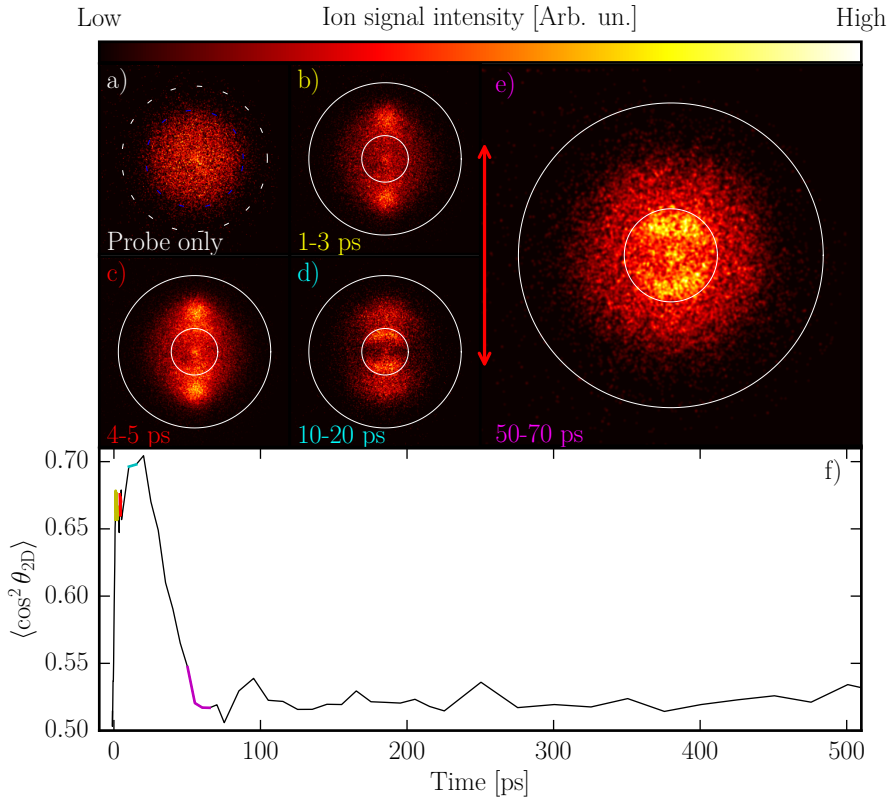

FIG. 5.4: Examples of IHe^+ images a)-e) for determining the degree of alignment f) of I_2 molecules inside helium droplets, as for the isolated molecules in Fig. 5.3. Image a) is again recorded without the kick pulse, and images b)-e) are recorded after a 1.3 ps, 3.7 TW/cm^2 kick pulse. The ion images are averaged over the indicated time intervals (colored) and scaled to their individual maxima. The corresponding time intervals are colored accordingly on the trace f). For display, all images are smoothed with a Gaussian filter with a standard deviation of 0.7 pixels.

5.2.3 Results

Ion images like those presented in Figs. 5.3 and 5.4 are recorded for a variety of pulse configuration and pump-probe delays. The resulting $\langle \cos^2 \theta_{2D} \rangle$ traces are displayed in Figs. 5.5-5.6. Panels with the same names in the two figures show results obtained under the same laser conditions. The right columns of panels expand on the initial times to highlight the structure that starts to appear in

panel e). Each row is annotated with the kick pulse fluence

$$F = \int_{-\infty}^{\infty} I(t)dt \overset{\text{Gaussian}}{=} \tau I_0 \sqrt{\frac{\pi}{4\ln 2}} \tag{5.2}$$

used in the experiment. In panels a)-e), the kick pulse duration (FWHM) is $\tau = 450\,\text{fs}$ and in panels f)-i) the pulse duration is increased to $\tau = 1.3\,\text{ps}$ in order to decrease the peak intensity. This is to avoid multiphoton (or tunneling) ionization caused by the kick pulse. It may appear problematic that both pulse parameters are varied in a seemingly unsystematic way. However, in the δ-kick [59–61] limit $\tau \to 0$, the kick pulse fluence alone determines the induced rotational wave packet [56], i. e. the two pulse parameters I_0 and τ merge into one.

Each data point in the gas phase traces is an average over 400 images, each containing roughly 50-60 ion hits. Of these, a total of roughly 15 000 hits are within the radial ranges for each delay on average. For the droplets, 10 000 images are recorded for each delay with on average one ion hit every two images. Of these, 3-4000 typically hit inside the radial ranges and contribute to the calculation of $\langle\cos^2\theta_{2D}\rangle$ at each data point. Due to the long acquisition time for the droplet experiments, parts of the $\langle\cos^2\theta_{2D}\rangle$ traces for the droplet experiments (panels f1)-h1) in Fig. 5.6) have not been recorded.

In Fig. 5.5 the results for the isolated molecules are shown. The experimental curves (black) are plotted on top of results from a simulation (red), where the simulation has been fitted by varying the temperature. It should be noted that the traces are nonuniformly sampled, e. g. the sample rate is higher during the revivals than between them. Between the revivals, the recorded trace looks more noisy where the sample rate is higher. It is unclear to what degree the fluctuations represent the noise level and how much the fluctuations represent actual fine structure due to the many small but nonzero bands in the $\cos^2\theta_{2D}$ matrix representation. See sections 2.2.2 and 3.2 where higher order revivals are discussed. These are found to be small and fast, resembling noise, and, crucially, they survive both thermal and focal volume averaging as seen in Fig. 3.1d) on page 40.

The fitted curves generally match the experimental curves well. However, as the kick pulse fluence is increased, small discrepancies in the oscillations at the revivals begin to show. The discrepancies are most pronounced in panels h1) and i1). The discrepancy is most likely due to centrifugal distortion, which has a tendency to distort the revivals asymmetrically [88, 89]. Asymmetric broadening of the revivals is reproduced qualitatively in preliminary simulations taking into account centrifugal distortion using a modified version of the program presented in chapter 3. Another contributing cause to the discrepancies could be that the detection probability is not linearly dependent on the probe pulse intensity, as is assumed in the focal volume averaging of the simulation.

The effects of neglecting centrifugal distortion seems to be reflected in the fitted temperatures in Table 5.1, that overall seem to decrease as the kick pulse

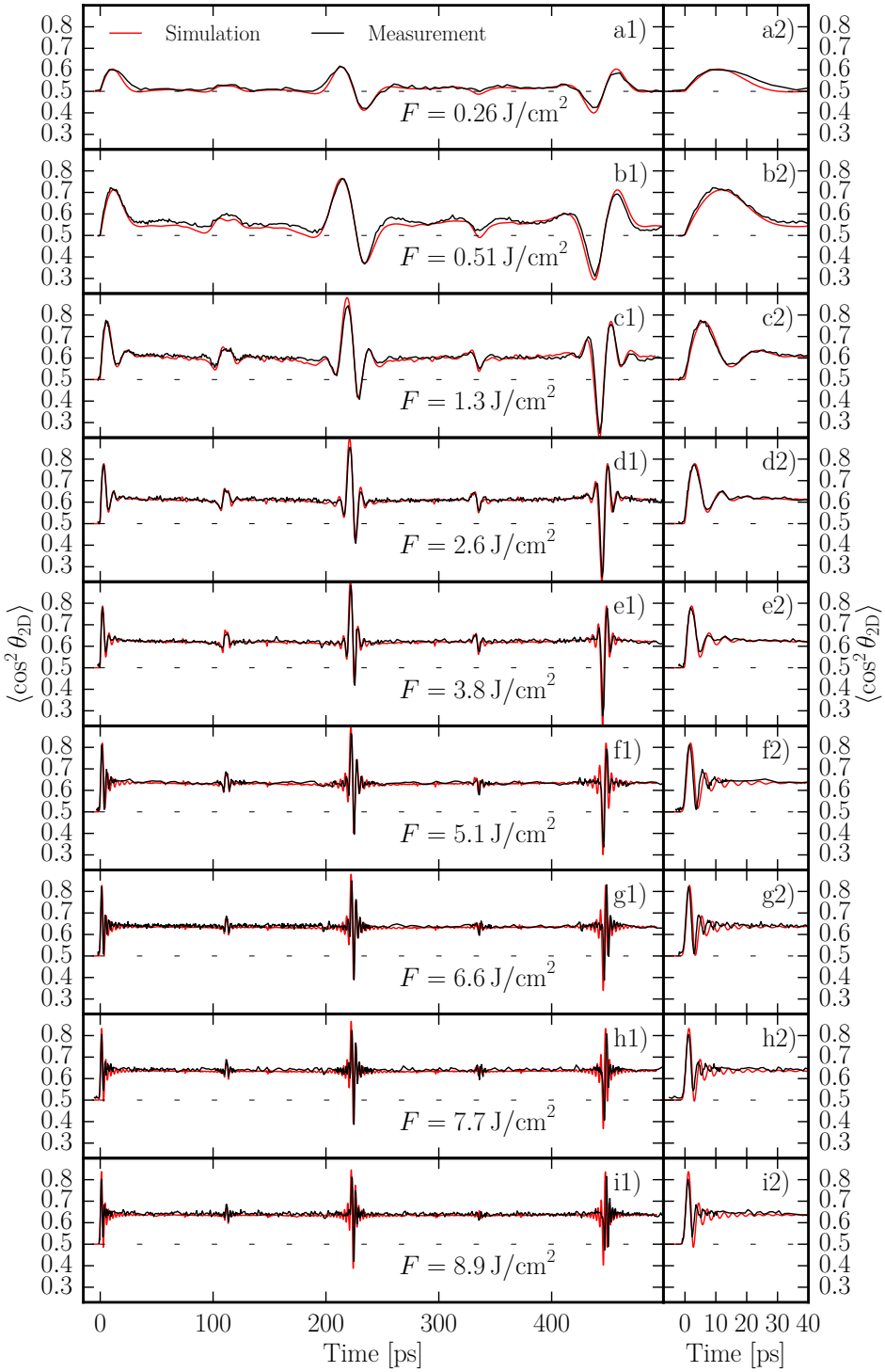

FIG. 5.5: The time-dependent degree of alignment represented by $\langle\cos^2\theta_{2D}\rangle$ of isolated I_2 molecules at 9 different fluences of the kick pulse. The rightmost panels is a zoom of the first 40 ps.

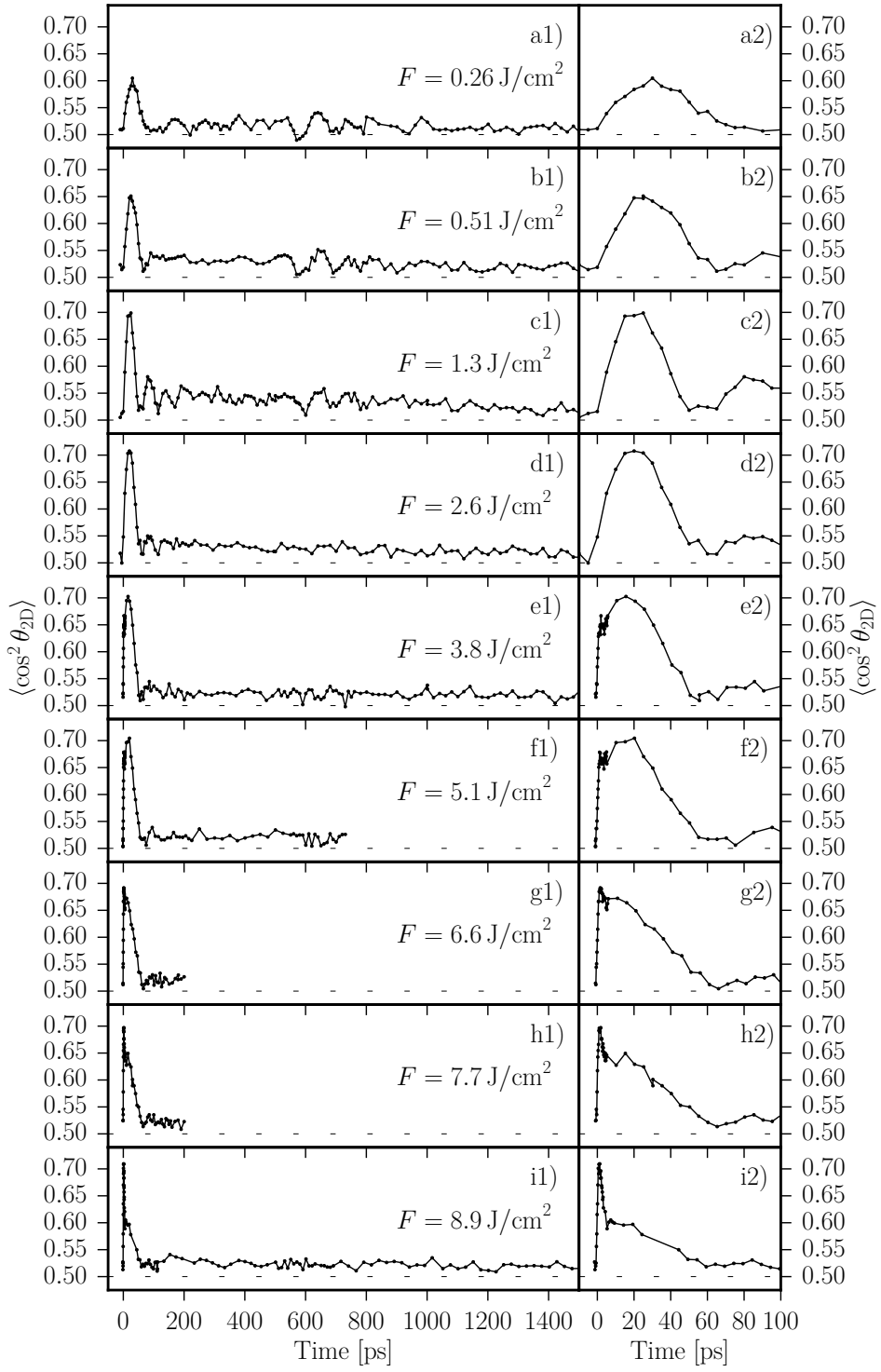

FIG. 5.6: The time-dependent degree of alignment represented by $\langle \cos^2 \theta_{2D} \rangle$ of I_2 molecules in He droplets at 9 different fluences of the kick pulse. The rightmost panels is a zoom of the first 100 ps.

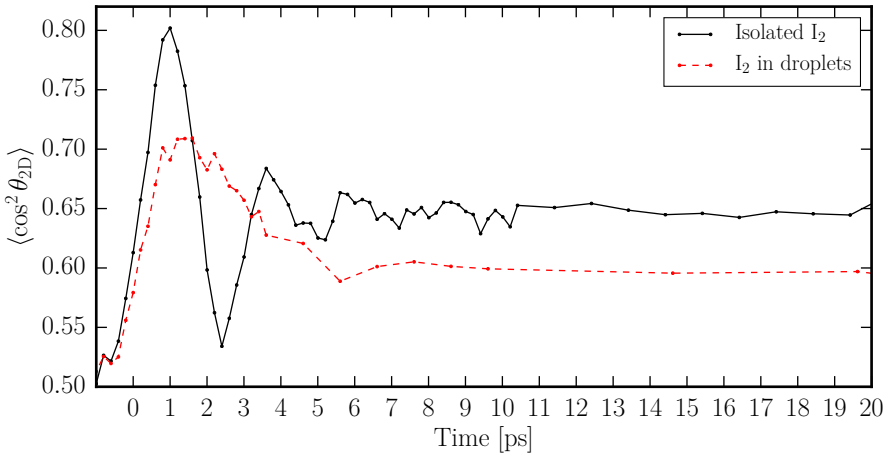

FIG. 5.7: Comparison of the measured early alignment dynamics for isolated I_2 and I_2 in the droplets at the highest kick pulse fluence $F = 8.9\,\mathrm{J/cm^2}$. The laser parameters are identical for the two traces.

fluence is increased. The difference might also (partly) be explained by the change in the pulse duration between panels a)-d) and e)-i), since the sensitivity of the fitted temperatures to variations in the pulse parameters have not been investigated. More precisely, the uncertainty in the pulse characterization may give rise to a systematic uncertainty in the difference between the kick pulse fluences measured at the two different kick pulse durations.

Panel	a	b	c	d	e	f	g	h	i
Temperature [mK]	790	383	273	625	546	130	102	100	97

Table 5.1: Temperatures fitted to the alignment traces in Fig. 5.5.

The true temperature of the supersonic beam is most likely best approximated by the result $T = 0.79\,\mathrm{K}$ obtained for the least intense pulse, since the molecules here experience the least centrifugal distortion. Such a rotational temperature is consistent with previous determinations, for instance iodobenzene 1.05 K [90] and aniline 0.4 K [77] for the molecular beam from an Even-Lavie valve.

Overall, the gas phase results presented in Fig. 5.5 appear as expected and seem well understood.

The results for the droplet experiments are shown in Fig. 5.6. For the low kick pulse fluences in panel a)-d) a prompt alignment peak appears within the

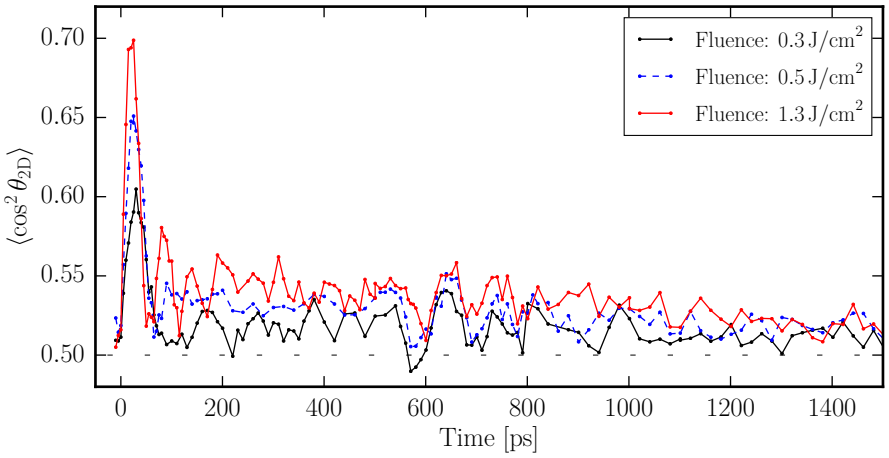

FIG. 5.8: Direct comparison of the alignment traces in Fig. 5.6 a)-c).

first 100 ps. As the kick pulse fluence is increased, the peak becomes more narrow and tall, and occurs earlier. This is consistent with the earlier results on alignment of e. g. CH_3I in helium droplets [17], and is similar to the alignment dynamics in the gas phase (compare e. g. to Fig. 5.5 a2)-d2)). It is noted that the prompt alignment dynamics here appear about $2-3$ times slower than for the isolated molecules, which is a considerably lower than the factor 10-170 reported for CH_3I [17]. A factor $2-3$ is in much better agreement with the expectation from rotationally-resolved spectra [15].

As the kick pulse fluence is increased, a new substructure appears in the prompt alignment peak (panels e2-i2) at very early times (< 10 ps). The feature becomes more prominent as the kick pulse fluence is increased, while the slower structure diminishes. This fast structure is very similar to the one observed for CS_2 in Fig. 5.2. A direct comparison of the isolated molecules and those in droplets is seen in Fig. 5.7. Before about 1 ps, the two traces closely follow each other. At 1 ps an abrupt change in this gas-phase-like structure occurs for the droplet trace. The trace flattens out and decays towards the secondary peak, which then decays completely within about 100 ps.

The droplet data presented here exhibits new features never observed before. After the prompt alignment peak, pronounced ringings or oscillations can be seen (see Fig. 5.6 a)-e)). These ringings resemble those that usually occur after the prompt alignment peak in alignment traces for isolated molecules, for example in Fig. 5.5 c2-i2). Another new feature is the appearance of a distinct oscillatory structure around 550–750 ps in Fig. 5.6 a-c). The droplet traces in those panels are shown in the same window in Fig. 5.8. The oscillatory structure appears at

essentially the same time for the three lowest kick pulse fluences. For the lowest kick pulse fluence, the oscillation dips below $\langle\cos^2\theta_{2D}\rangle = 0.5$ just before 600 ps. As the kick pulse fluence increases, the structure becomes slightly more narrow with slightly higher degrees of alignment at the central peak. This is similar to the behavior of rotational revivals for isolated molecules. This structure is the most clear indication of coherent rotation out to at least 700 ps for the lowest three kick pulse fluences.

Another new feature never seen before is that the "permanent" alignment level, or local average, increases with increasing kick pulse fluence for the lowest three kick pulse fluences in the full time range 100–1500 ps. This is similar to the alignment behavior for isolated molecules. However, the local average is clearly seen to slowly decrease over the whole time range for all three traces in Fig. 5.8. As mentioned below Fig. 5.1 on page 62, any excited state[3] contributes positively to a permanent alignment level above $\langle\cos^2\theta_{2D}\rangle = 0.5$. Furthermore, the oscillations in the $F = 1.3\,\mathrm{J/cm^2}$ trace (red) are initially fast, but gradually become slower. In the gas phase, the fastest time structure is given by the beat frequency between the two highest populated J states (for $\langle\cos^2\theta\rangle$ – for $\langle\cos^2\theta_{2D}\rangle$ higher frequencies are expected, but only at much lower amplitudes, see section 2.2.2). These two experimental observations suggest that the J states populated by the kick pulse gradually decays. As the kick pulse fluence in increased (Fig. 5.6 d1)-i1)), the permanent alignment level no longer increases, but quickly vanishes, indicating an even faster decay of J states. The fast initial feature before 5 ps shows up at the same kick pulse fluence where the permanent alignment level has decayed completely. One interpretation of this is that the rotation crosses the excitation threshold at that kick pulse fluence, creating a roton. Does the roton backflow [40, 42] hit the molecule on a time scale of 1-2 ps?

The gas phase traces in Fig. 5.5 were only recorded out to 500 ps, and the droplet traces in Fig. 5.6 were recorded to 1.5 ns. In order to have at least one complete comparison, the gas phase experiment at a kick pulse fluence of $0.51\,\mathrm{J/cm^2}$, i. e. panel b) in Fig. 5.5, was selected to be extended up to 1.5 ns. The result is shown in Fig. 5.9. As can be seen, an interesting result turned up, and it was decided that the experiment should be extended up to the longest delay possible at 3.2 ns. Both the permanent alignment level and the amplitude of the revivals decay all by themselves for isolated I_2 molecules, and the alignment trace is not periodic as expected from the theory in chapter 2 (see equations (2.32), (2.34) and (2.35) on page 23). Since a decay of the permanent alignment level can only come from a decay of population from high to low J states, three questions arise from the result in Fig. 5.9: 1) What mechanism causes isolated I_2 molecules to loose angular momentum? 2) How severe is the decay? and 3) How much of the decay in the droplet results Fig. 5.6a)-c) is caused by this self-decay and how much is caused by the helium environment? Aperiodicity was already seen in the gas phase result Fig. 5.5 at high kick pulse fluences due to centrifugal distortion.

[3] Or deviation from equipartition by overrepresentation of low M in case $M > 0$ before the kick.

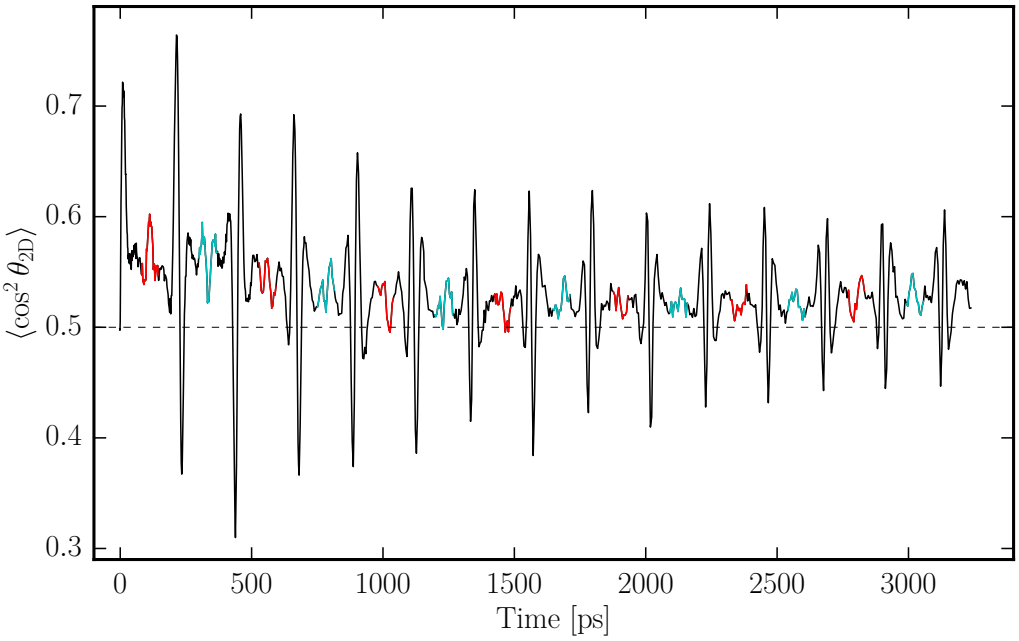

FIG. 5.9: Measured degree of alignment for isolated I_2 molecules exposed to the same $F = 0.51\,\mathrm{J/cm^2}$ pulse as in Figs. 5.5b) and 5.6b). The time is extended to 3.2 ns. The $1/4 + n$ and $3/4 + n$ revivals have been colored red and light blue, respectively.

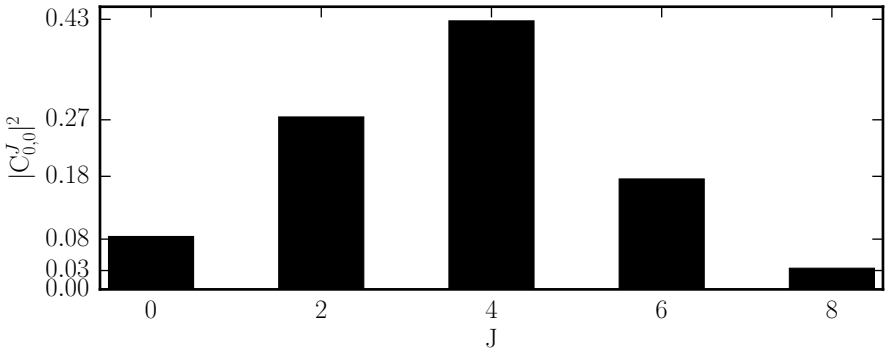

FIG. 5.10: Simulated rotational state distribution after the kick pulse used in Fig. 5.9 of an isolated I_2 molecule initially residing entirely in the ground state $|000\rangle$.

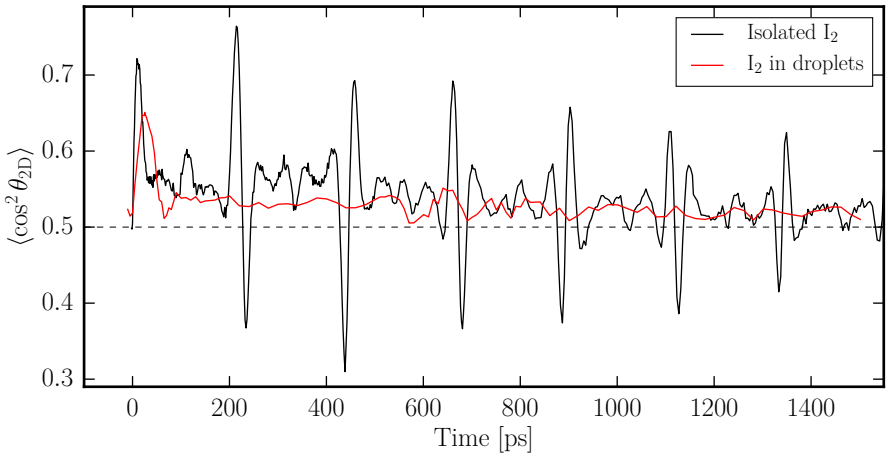

FIG. 5.11: Direct comparison of the measured degree of alignment represented by $\langle \cos^2 \theta_{2D} \rangle$ for isolated I_2 molecules and I_2 in helium droplets. The two traces are recorded under the same conditions, with the same kick pulse fluence $F = 0.51\,\mathrm{J/cm^2}$.

However, centrifugal distortion can not explain the observed decay of alignment, since the centrifugal distortion does not mix J levels (to first order, it is just an additional term in the rotational energy).

To answer question 2, then, see Figs. 5.10 and 2.3 (page 25). Figure 5.10 shows the rotational state distribution after the kick pulse used in Fig. 5.9. Clearly, the induced wave packet is not at all very broad, and a decay of just one $\hbar$ would be enough to significantly alter the permanent alignment level (compare Fig. 2.3).

As for question 1), since ^{127}I has nuclear spin $5/2 \geq 1$, the nuclei have nonzero quadrupole moments[58]. These can interact with the electron distribution of a rotating, linear molecule as long as $J \geq 1$. The selection rule for this interaction is $\Delta J = 0, \pm 1, \pm 2$. With the relatively large ^{127}I nucleus and the large number of electrons in I_2, it seems likely that this quadrupole interaction is strong enough to explain the needed decay. Rotational angular momentum could be transferred to nuclear spin.

Note that with the $\Delta J = \pm 1$ selection rule, the rotational wave function changes parity. Thus the quater revivals should changed from pointing upwards to pointing downwards (see the note on page 31). The $1/4 + n$ revivals (red) and $3/4 + n$ revivals (light blue) indeed seems to be oscillating, roughly in counter-phase, for the duration of the experiment (see Fig. 5.9).

As for the third question, it is not clear to what degree this effect influences the decay in the droplets for the low kick pulse fluences. However, from Fig. 5.11 the

decay time does seem very comparable. The permanent alignment level reaches roughly $\langle \cos^2 \theta_{2D} \rangle = 0.5$ in the same amount of time $t \approx 1500$ ps for the two traces. Furthermore, the permanent alignment levels seem very similarly sloped in the interval 750–1500 ps. It seems reasonable to suspect that without this effect, the decay would have at least taken longer. Perhaps the revival-like structure around 650 ps in the droplet data would then have been stronger without the self-decay. It would be interesting to try the experiment again with another heavy molecule where the nuclear spin is less than 1. Another approach towards stronger revivals is to find an even heavier molecule that supports a broader rotational wave packet before interacting with the helium, since the nuclear spin interaction would then take longer to drive the molecular rotation towards the low J states that exhibit decaying permanent alignment levels (see Fig. 2.3 on page 25).

5.3 Summary

In brief, an introduction to previous results on aligning molecules inside helium droplets have been given. The historical results are inconsistent with those of rotationally-resolved spectra since the alignment results clearly show that the rotation is hindered by the helium environment.

A new experiment where I_2 molecules are impulsively aligned both inside helium droplets and in isolation was described. In the experiment, the alignment, characterized by $\langle \cos^2 \theta_{2D} \rangle$, is measured by recording the emission direction of I^+ (from isolated molecules) and IHe^+ (from molecules in droplets) ionic fragments from Coulomb exploding the molecules.

The result of this experiment shows several new, never observed before features of alignment of molecules inside helium droplets. Most importantly, for low kick fluences, clear signs of free, coherent rotation out to at least 600 ps are seen. Many of the features indicating coherent rotation vaguely resemble those for rotation of isolated molecules. In particular, a revival-like structure between 550–750 ps is seen, positioned independently on the kick pulse fluence. This structure becomes slightly more defined with increasing kick pulse fluence, up to a point where the coherence becomes lost and very fast initial dynamics emerge.

Lastly, apparent deviation from free, coherent rotation is seen even for isolated I_2 molecules. This deviation is tentatively ascribed to quadrupole interactions between the atomic nuclei and the electrons. For the low kick pulse strengths, it is unclear exactly to what degree the breakdown of free, coherent rotation can be explained by the helium environment and how much can be ascribed to the quadrupole interaction. It seems that neither effects are negligible. New impulsive alignment experiments on other heavy molecules are required to elucidate the conditions under which helium nanodroplets permit free rotation and thereby strong field-free alignment of molecules.

CHAPTER 6

Rationalization of observed alignment behavior through simplified models

The new droplet results presented in the previous chapter seem as if they are closer to being describable with the alignment theory for isolated molecules than all the previous results. For example, the new results exhibit for the first time ever what appears to be a rotational revival in the droplet phase. The surprising decay of alignment in the corresponding gas phase experiment seems to suggest that the rotation is even more free than what could otherwise be interpreted from the droplet results alone.

Why is I_2 more free to rotate than all the previously studied molecules? In this chapter, two simplified models are presented to give at least qualitative answers to this question. The first is a quantum mechanical model of a linear rotor with just a single helium atom attached. Although this may sound almost too simplified, the model turns out to have surprisingly high predictive power. The theoretical model is described in section 6.1 and was developed by Robert Zillich based on existing theory for atom-spherical top van der Waals complexes [91]. I implemented the model in a simulation program, which is described in section 6.2. In section 6.3, predictions of this model is described and compared to the experiments. The results of the quantum model inspired my supervisor Henrik Stapelfeldt to develop a classical model, described in section 6.4, which in many ways is in good agreement with the quantum mechanical model, and which further relates the experimental results to classical properties of superfluid helium.

The quantum mechanical model and simulation program presented here was also presented in my progress report in the middle of my PhD study. The work on and description of the quantum mechanical model forms the basis of a publication

in preparation [A3], and the classical model is incorporated in another manuscript in preparation [A2].

6.1 Quantum model

The interaction between a molecule and a neutral, closed shell (helium) atom is the van der Waals force between either a permanent or induced dipole of the molecule and the induced dipole of the helium atom. The van der Waals force is also what binds the atoms in a helium droplet together.

The theory of atom-spherical top van der Waals complexes was developed by Hutson and Thornley [91] in 1993. Robert Zillich specialized the theory to the case of a linear molecule, and incorporated the interaction between the molecule and an alignment laser field. The specialization to linear molecules is in order to ensure computational feasibility of the model.

6.1.1 Coordinate system

In order to calculate the alignment of a molecule-atom complex induced by a linearly polarized laser pulse, the two-body Schrödinger equation for the molecule degrees of freedom (rotation) and the atom (translation) must be solved. The molecule-atom system is described by the coordinates $\mathbf{r_0}$ for the molecule center of mass position, the direction $\mathbf{\Omega}$ of the molecule axis, and by the position of the atom $\mathbf{r}_1$ (see Fig. 6.1). Because of translational invariance, only the relative translational motion, described by $\mathbf{r} = \mathbf{r_1} - \mathbf{r_0}$ is needed. The vector $\mathbf{r}$ is from the molecule center mass to the atom. As in chapter 2, the polarization direction $\hat{\mathbf{E}}_{\text{laser}}$ of the laser field is taken to be along the Z axis. Consequently, θ is again

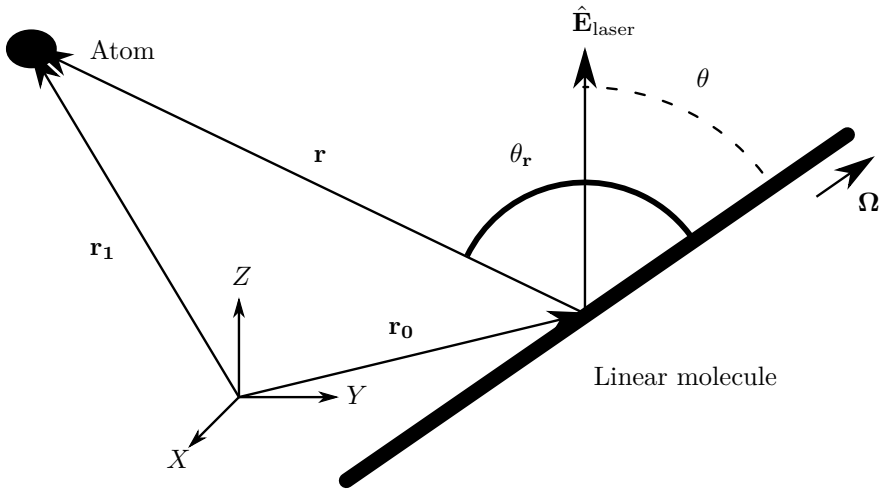

FIG. 6.1: Space-fixed molecule-atom coordinate system.

both the angle between the laser polarization and the molecule and the polar angle of the molecular axis in the lab frame. The length of $\mathbf{r}$ is denoted r and the angle between the molecular axis (pointing in the $\mathbf{\Omega}$ direction) and $\mathbf{r}$ is denoted $\theta_{\mathbf{r}}$.

In these coordinates, the Hamiltonian takes the form

$$\mathcal{H} = \mathcal{H}_{\text{free}} + V(\theta, t) - \frac{\hbar^2}{2\mu}\nabla^2_{\mathbf{r}} + W(r, \theta_{\mathbf{r}}), \tag{6.1}$$

where, as in (2.1), $\mathcal{H}_{\text{free}} = \frac{\mathbf{j}^2}{2I}$ is the rotational Hamiltonian of the isolated molecule. Note the slight notational difference $\mathbf{j}$ being the angular momentum of the molecule about its center of mass, $\mathbf{J}$ being reserved as the total angular momentum. The moment of inertia of the molecule reduces to a single value I. Note the resemblance to (2.5). The rotation around the molecular axis has been left out and instead two terms have been added. These are $-\hbar^2/2\mu\nabla^2_{\mathbf{r}}$, which is the kinetic energy of the relative motion of the molecule and atom, and $W(r, \theta_{\mathbf{r}})$, which is the potential energy for the molecule-atom interaction. The atom-molecule reduced mass $\mu = m_{\text{at}}m_{\text{mol}}/(m_{\text{at}} + m_{\text{mol}})$ is calculated from the mass of the atom m_{at} and the mass of the molecule m_{mol}. Finally, V is the molecule-laser potential (2.4) as used previously. The laser field is modeled exactly as in the previous chapters 2 and 3. Similarly, thermal and focal volume averaging is implemented as in chapter 3.

Since the strong E-field changes the polarization of both the atom and the molecule, the molecule-atom interaction potential $W(r, \theta_{\mathbf{r}})$ is transiently increased during the pulse. For separations between the atom and the molecule larger than or equal to the value in the ground state ($r \sim 4\,\text{Å}$) the effect is, however, negligible and not included here.

6.2 Implementation

To solve the Schrödinger equation with the Hamiltonian (6.1), it is convenient to express the Hamiltonian in terms of the angular momentum $\mathbf{L}$ of the orbital motion of the entire system about its center of mass

$$\mathcal{H} = \frac{B\mathbf{j}^2}{\hbar^2} + \frac{\mathbf{L}^2}{2\mu r^2} - \frac{\hbar^2}{2\mu r}\frac{\partial^2}{\partial r^2} + V(\theta, t) + W(r, \theta_{\mathbf{r}}). \tag{6.2}$$

The rotational constant $B = \hbar^2/2I$ is as used previously. This form allows expansion of the wave function Ψ in the coupled eigenbasis of $\mathbf{j}^2$, $\mathbf{L}^2$, $\mathbf{J}^2$ and J_z, where $\mathbf{J} = \mathbf{j} + \mathbf{L}$ is the total angular momentum and J_z is its projection on the laser polarization axis,

$$\Psi_N(\mathbf{r}, \mathbf{\Omega}) = \sum_{j,L,J} c_{jLJN}(r) \langle \mathbf{r}, \mathbf{\Omega} | jLJN \rangle . \tag{6.3}$$

Here j, m and L, M are the quantum numbers associated with $\mathbf{j}^2$ and $\mathbf{L}^2$, respectively, J is the total angular momentum quantum number and $N = m + n$ is the

	$\alpha_\parallel$ [Å^3]	$\alpha_\perp$ [Å^3]	$\Delta\alpha$ [Å^3]	B [GHz]	mass [amu]
CS_2	15.6[92]	5.3[92]	10.3	3.271[93]	76.14
HCCH	4.675†	2.889†	1.786	35.27[93]	26.04
I_2	14.562[94]	8.4627[94]	6.0993	1.12[93]	253.81
He					4.003

† From Ref. 93, calculated with a density functional in the B3LYP/aug-cc-pVTZ basis.

Table 6.1: Model parameters for species used in the simulations.

quantum of its projection on the laser polarization axis. The coupled basis is

$$\langle \mathbf{r}, \mathbf{\Omega} | jLJN \rangle = \sum_{mM} \langle jmLM | JN \rangle \, Y_{jm}(\mathbf{\Omega}) Y_{LM}(\mathbf{\Omega}_r), \tag{6.4}$$

where $\mathbf{\Omega}_r$ is the direction of the vector $\mathbf{r}$ and the Clebsch-Gordan coefficient $\langle jmLM|JN\rangle$ couples the spherical harmonic angular momenta eigenstates $|jm\rangle$ and $|LM\rangle$ for the individual angular momenta in the sum.

This choice of basis ensures conservation of N at all times and conservation of energy and $\mathbf{J}^2$ before and after the pulse. These conservation laws are not guaranteed to be obeyed if for example the uncoupled basis $|jm\rangle|JM\rangle$ is used because of numerical round-off errors. The conservation is guaranteed only as long as the expansion coefficients stay normalized, however.

The expansion onto the $|jLJN\rangle$ basis discretizes all angular dependence. The radial direction is discretized in $2^7 - 1 = 127$ equidistant steps separated with a distance $\Delta r = 0.16\,\text{Å}$ for CS_2 and $\Delta r = 0.14\,\text{Å}$ for HCCH and I_2. The number of radial steps is chosen as a power of 2 minus 1 for maximum performance of the fast discrete sine transform discussed below. The molecular data used in the simulations are listed in table 6.1.

Inserting the expansion (6.3) in the Schrödinger equation and projecting onto the $|j'L'J'N'\rangle$ state yields the coupled channel equations for the radial wave function $u_{jLJN}(r) = r c_{jLJN}(r)$

$$\begin{aligned} i\hbar \dot{u}_{jLJN}(r) = &\left(Bj(j+1) + \frac{\hbar^2 L(L+1)}{2\mu r^2} - \frac{\hbar^2}{2\mu}\frac{\partial^2}{\partial r^2} \right) u_{jLJN}(r) \\ &+ \sum_{j'J'} V_{jLJN}^{j'LJ'N}(t) u_{j'LJ'N}(r) + \sum_{j'L'} W_{jLJN}^{j'L'JN}(r) u_{j'L'JN}(r). \end{aligned} \tag{6.5}$$

Here, the $\frac{1}{r}\frac{\partial^2}{\partial r^2} r$ operator has been converted to $\frac{\partial^2}{\partial r^2}$, which is diagonal in Fourier space, by working with the radial wave function u instead of the expansion coefficients c. The coupled channel equation (6.5) have been derived e. g. in Ref. 91 for general molecules, but only in the field-free case. It was Robert Zillich who derived this generalization.

The interaction matrix elements are

$$V_{jLJN}^{j'L'J'N'}(t) = \langle j'L'J'N'|V(\theta,t)|jLJN\rangle. \tag{6.6}$$

$$W_{jLJN}^{j'L'J'N'}(r) = \langle j'L'J'N'|W(r,\theta_{\mathbf{r}})|jLJN\rangle \tag{6.7}$$

In (6.5), some primed quantum numbers have been omitted because the potential matrices are diagonal in those numbers.

6.2.1 Matrix elements

To solve the coupled channel equations, expressions for the matrix elements (6.6) and (6.7) must be obtained. Doing so is a rather technical and uneventful exercise in angular momentum algebra. The following result that I derived simplifies the work involved when dealing with already known molecular operators and observables, i. e. operators that are independent of the atom degrees of freedom (equivalently the quantum numbers r, L and M), like those already given and derived in chapter 2. Assume

$$A_{jm}^{j'm'} = \langle j'm'|A|jm\rangle \tag{6.8}$$

is a known matrix representation of a molecular operator A, for example $A = \cos^2\theta$ or $A = \cos^2\theta_{2\mathrm{D}}$. Then in the coupled basis

$$\begin{aligned}
A_{jLJN}^{j'J'N'} &= \langle j'L'J'N'|A|jLJN\rangle \\
&= \sum_{MM'mm'} \langle j'L'J'N'|j'm'L'M'\rangle \langle L'M'|\langle j'm'|A|jm\rangle|LM\rangle \langle jmLM|jLJN\rangle \\
&= \sum_{MM'mm'} A_{jm}^{j'm'} \langle j'L'J'N'|j'm'L'M'\rangle \langle jmLM|jLJN\rangle \delta_{LL'}\delta_{MM'} \\
&= \delta_{LL'} \sum_{mm'} A_{jm}^{j'm'} \langle j'm'L'(N'-m')|J'N'\rangle \langle jmL(N-m)|JN\rangle \delta_{N-m,N'-m'}.
\end{aligned} \tag{6.9}$$

It is seen that $A_{jLJN}^{j'J'N'}$ is only changed by the appearance of two Clebsch-Gordan coefficients, and is only non-zero if $L = L'$, $N - m = N' - m' \Leftrightarrow \Delta N = \Delta m$, and if the following selection rules are obeyed:

$$|j' - L| \leq J \leq j' + L \tag{6.10}$$

$$|j - L| \leq J \leq j + L. \tag{6.11}$$

With this result, the $\cos^2\theta$ operator (2.16) is re-expressed in the coupled basis

$$\begin{aligned}
&\langle j'L'J'N'|\cos^2\theta|jLJN\rangle = \delta_{N,N'}\delta_{L,L'}\sqrt{(2J+1)(2J'+1)} \\
&\times \sum_m \left[(-1)^m \frac{2}{3}\sqrt{(2j+1)(2j'+1)} \begin{pmatrix} j & j' & 2 \\ 0 & 0 & 0 \end{pmatrix} \begin{pmatrix} j & j' & 2 \\ m & -m & 0 \end{pmatrix} + \frac{1}{3}\delta_{j,j'}\right] \\
&\times \begin{pmatrix} j & L & J \\ m & N-m & -N \end{pmatrix} \begin{pmatrix} j' & L & J' \\ m & N-m & -N \end{pmatrix}.
\end{aligned} \tag{6.12}$$

The relation between the Clebsch-Gordan coefficients and the Wigner 3j symbols

$$\langle j_1 m_1 j_2 m_2 | j_3 m_3 \rangle = (-1)^{j_1 - j_2 + m_3} \sqrt{2j_3 + 1} \begin{pmatrix} j_1 & j_2 & j_3 \\ m_1 & m_2 & -m_3 \end{pmatrix} \tag{6.13}$$

have also been used to obtain (6.12). The $\cos^2\theta$ operator doubles as both the observable and an ingredient in the interaction matrix (6.6) as

$$V_{jLJN}^{j'L'J'N'}(t) = -\frac{E_0(t)^2}{4} \left(\Delta\alpha \langle j'L'J'N' | \cos^2\theta | jLJN \rangle + \alpha_\perp \right). \tag{6.14}$$

The $\cos^2\theta_{2\mathrm{D}}$ observable is not implemented as the simulation is already close to being computationally infeasible.

The molecule-atom potential energy surface $W(r, \theta_{\mathbf{r}})$ is taken as program input. The potential energy surface is taken from Ref. 95 for CS_2-He, from Ref. 96 for HCCH-He and from Ref. 97 for I_2-He. For a linear molecule the cylindrical symmetry allows the potential to be expanded in Legendre polynomials

$$W(r, \theta_{\mathbf{r}}) = \sum_{\lambda} P_\lambda(\cos\theta_{\mathbf{r}}) W_\lambda(r). \tag{6.15}$$

The program input consists of the expansion coefficients $W_\lambda(r)$ for $\lambda = 0, \ldots, \lambda_{\max}$, where $\lambda_{\max} = 16$ for CS_2 and HCCH and $\lambda_{\max} = 24$ for I_2. In the case of CS_2, HCCH and I_2, odd λ coefficients are zero because of the inversion symmetry. With the spherical harmonics addition theorem [58]

$$P_\lambda(\cos\theta_{\mathbf{r}}) = \frac{4\pi}{2\lambda + 1} \sum_{\nu} Y_{\lambda\nu}^*(\mathbf{\Omega}_{\mathbf{r}}) Y_{\lambda\nu}(\mathbf{\Omega}), \tag{6.16}$$

the expansion (6.15) is expressed in terms of angular momenta states $|\lambda\nu\rangle$

$$W(r, \theta_{\mathbf{r}}) = \sum_{\lambda\nu} \frac{4\pi}{2\lambda + 1} Y_{\lambda\nu}^*(\mathbf{\Omega}_{\mathbf{r}}) Y_{\lambda\nu}(\mathbf{\Omega}) W_\lambda(r) \tag{6.17}$$

which are then further coupled with the coupled basis states to give the matrix elements (6.7). The angular momentum algebra involved was performed by Robert Zillich, and is not reproduced here. The result is

$$W_{jLJN}^{j'L'}(r) = \sum_{Mm} \sum_{m',\lambda\nu,M'} (2J+1)(-1)^{m+M'} \begin{pmatrix} j & L & J \\ m & M & -N \end{pmatrix} \begin{bmatrix} j & \lambda & j' \\ -m & \nu & m' \end{bmatrix} \begin{bmatrix} L & \lambda & L' \\ -M & -\nu & M' \end{bmatrix} \begin{pmatrix} j' & L' & J \\ m' & M' & -N \end{pmatrix} \frac{4\pi W_\lambda(r)}{2\lambda + 1}, \tag{6.18}$$

with the abbreviation

$$\begin{bmatrix} a & b & c \\ u & v & w \end{bmatrix} \equiv \left(\frac{(2a+1)(2b+1)(2c+1)}{4\pi} \right)^{1/2} \begin{pmatrix} a & b & c \\ u & v & w \end{pmatrix} \begin{pmatrix} a & b & c \\ 0 & 0 & 0 \end{pmatrix}. \tag{6.19}$$

Numerically, the sum over four 3-j symbols is much more efficiently calculated as a Wigner 6-j symbol.

In the simulation, the Gnu Scientific Library (GSL) [64] is used to calculate 3-j and 6-j symbols. GSL uses numerically unstable textbook formulas for both 3-j and 6-j symbols. For the 3-j symbols, this is not a problem because only the $\cos^2\theta$ operator is needed, and the formulas are stable for the low quantum numbers encounted here. However, I had to modify the GSL source code for calculating the 6-j symbols to handle the large quantum numbers involved. I extended the stable region by modifying the used formula to work with the logarithm of factorials instead of with the factorials directly, as suggested by Robert Zillich. This was done before I became aware of stable, fast recursion relations [66, 68]. It is noted that Jonathan G. Underwood is in the process of implementing the recursion relations of Ref. 68 in the GSL.

6.2.2 Propagation

The coupled channel equations (6.5) is a set of coupled, linear partial differential equations describing the time evolution of the wave function. In contrast, the coupled channel equations for the isolated molecule (2.11) are ordinary differential equations. The numerical solution of ordinary differential equations is straightforward, since standard numerical algorithms like those of the celebrated Runge-Kutta family are widely available in numerical libraries.

The addition of another differential $\partial^2/\partial r^2$ in (6.5) from the kinetic energy term turns the ordinary differential equations into partial differential equations. They are still linear, though, which means e. g. the time evolution after the pulse could be solved by expanding the wave function in the energy eigenstates, at least if these states could be found in a reasonable amount of time. With a δ kick pulse, the wave function immediately after the pulse could be found in the uncoupled representation $|jm\rangle|LM\rangle$ with the theory for the isolated molecule, since the pulse would not influence the atom state, which furthermore is frozen for the duration of the pulse. It is less clear how a finite pulse should be implemented.

This approach is not taken, as the model is anticipated to be extended to include more than one helium atom. In fact, following my work on the simulation, the model has already been extended by Robert Zillich, but only in two dimensions, since the time complexity scales badly with the number of coordinates. By including more than one helium atom, the equations become nonlinear, and the eigenstate expansion would not work. The nonlinearity comes from the interaction between the helium atoms. The complexity of this problem is similar to the complexity arising in treating more than one electron in atomic physics calculations.

In this simulation, the time evolution is generated directly with the time evolution operator [62]. The wave function at any time t can be be found from the initial wave function at time t_0

$$\Psi_N(t) = \mathscr{U}(t, t_0)\Psi_N(t_0), \tag{6.20}$$

where $\mathscr{U}(t,t_0) = \exp(-i\mathcal{H}(t-t_0)/\hbar)$ is the time evolution operator, in this case for a time-independent Hamiltonian. Calculating $\mathscr{U}(t,t_0)$ for arbitrary t is not feasible. Therefore, the propagation is done in small time steps dt, on the order 5–10 fs, where also the Hamiltonian (6.2) is approximately time-independent. Experience has shown that the high intensity pulses populate j, J states up to around $j_{\max} = J_{\max} = 200$, in turn coupling L up to around $L_{\max} = 30$ during the first few ps. With a radial grid consisting of $N_r = 127$ points, the size of the full Hamiltonian matrix would be hundreds of petabytes. This size requirement can be avoided by working with the terms in the Hamiltonian individually, since they couple the channels $jLJNr$ relatively sparsely. The matrix exponential generally does not satisfy the usual relation $\exp(A+B) = \exp(A)\exp(B)$ except when A and B commute. However, by applying the second order Trotter approximation [98]

$$e^{(A+B)dt} = e^{Adt/2}e^{Bdt}e^{Adt/2} + O(dt^3). \tag{6.21}$$

twice, a more manageable expression for the time evolution operator becomes

$$\begin{aligned}\mathscr{U}(dt) = \exp\left(-i\mathcal{H}dt/\hbar\right) \approx \exp(-idtT/2\hbar)\exp(-idtW'/2\hbar)\\ \times \exp(-idtV/\hbar)\exp(-idtW'/2\hbar)\exp(-idtT/2\hbar).\end{aligned} \tag{6.22}$$

Here $T = -\frac{\hbar^2}{2\mu}\frac{\partial^2}{\partial r^2}$ and $W' = Bj(j+1) + \frac{\hbar^2 L(L+1)}{2\mu r^2} + W$. V and W are the operators corresponding to the last two expressions in the coupled channel equations (6.5) for the field of the laser pulse and the molecule-atom interaction, respectively.

The T operator is diagonal in Fourier (k) space, since

$$\frac{\partial^2}{\partial r^2}\hat{u}(k)e^{ikr} = -k^2\hat{u}(k)e^{ikr}. \tag{6.23}$$

The action of $\exp(-idtT/2\hbar)$ on the Fourier transformed radial wave function $\hat{u}(k)$ is simply $\exp(-idtT/2\hbar)\hat{u}(k) = \exp(-(\hbar k)^2/4\mu)\hat{u}(k)$, and the action in position space is obtained by an inverse Fourier transform. Since $u(0) = ra(r) = 0 = u(\infty)$, only a discrete sine transform of u is needed. With an implied 0 at the first grid point, the discrete sine transform is most efficient if the grid size is a power of 2 minus 1.

Even after accounting for the selection rules in (6.18), storing the couplings in the $\exp(-idtW'/2\hbar)$ matrix would require 60 gigabytes of memory for each N. This seems surprising given that the expansion of W in Legendre polynomials in the molecular coordinates only requires a few kilobytes. But the situation is complicated by the exponential and the couplings in (6.18). This size can be halved because after 63 radial steps, W is neglecible, and only the diagonal elements of W' remain. Furthermore, inspection of the (unitless) matrix elements of $\exp(-idtW'/2\hbar)$ show that 90% of them have a magnitude below 10^{-10}, probably because of the small time step, giving a value close to the identity matrix, which is diagonal. These small elements are discarded, and a list of the remaining, non-negligible matrix elements is kept. The size is further reduced by storing

the matrix elements in IEEE 754 single precision format after calculating them in double precision. These approximations reduces the 60 gigabyte matrix to only 2-3 gigabytes, allowing the equations to be solved on a standard desktop computer. Two versions of the matrix is stored, since the time step during the pulse is shorter than after the pulse. A comparison with a simulation using the full 60 gigabyte W' matrix shows that the change in normalization of the state vector due to these approximations is less than on part in 10 000 even after 1 ns simulated time. Simulations using the large matrix were carried out on large virtual machines in the Amazon cloud[1].

The last factor $\exp(-idtV(t)/\hbar)$ in the middle of (6.22) due to the laser interaction presents the most serious challenge, since it is time-dependent. A recalculation of the matrix exponential would seem to be required in each time step. Several methods for calculating the matrix exponential exists [99]. Since in quantum mechanics, most matrices are Hermitian and thereby diagonalizable, a simple and relatively efficient way is to diagonalize the matrix $A = M^H \mathrm{diag}(\lambda_i) M$. Then

$$\exp(A) = \exp(M^H \mathrm{diag}(\lambda_i) M) = M^H \exp(\mathrm{diag}(\lambda_i)) M = M^H \mathrm{diag}(\exp(\lambda_i)) M. \tag{6.24}$$

Since the laser interaction potential

$$V(\theta, t) = \underbrace{-\frac{E_0(t)^2}{4}}_{\text{Time dependence}} \underbrace{(\Delta\alpha \cos^2\theta + \alpha_\perp)}_{\text{Angular dependence}} \tag{2.4}$$

is factored into a scalar time dependence and a constant matrix angular dependence, essentially only one matrix-matrix product is required[2] in each time step. However, in this basis, the matrix-matrix product would take almost 10 minutes to compute on a single core of the latest computer hardware, and correspondingly faster on multiple cores. This would render the calculations infeasible. For example, a 0.37 K initial ensemble would take half a year of cpu time to propagate if 30 focal volume intensities must be sampled.

6.2.3 Partial time steps in Krylov subspaces

The calculation is made feasible by the realization that the matrix $\exp(-idtV/\hbar)$ in itself is uninteresting, as only its action on the state vector is needed. This action can be approximated by projecting the V matrix down to the m dimensional Krylov subspace $\mathcal{K}_m(V, |\Psi\rangle)$ generated by V and the state vector $|\Psi\rangle$ [98, 100]

$$\mathcal{K}_m(V, |\Psi\rangle) = \mathrm{span}\{|\Psi\rangle, V|\Psi\rangle, V^2|\Psi\rangle, \ldots, V^{m-1}|\Psi\rangle\}. \tag{6.25}$$

[1] http://aws.amazon.com

[2] I realized after the implementation that this argumentation is somewhat flawed. Only two much cheaper matrix-vector operations are required since $(M^H \mathrm{diag}(\exp(\lambda_i))M)|\Psi\rangle = M^H(\mathrm{diag}(\exp(\lambda_i))(M|\Psi\rangle))$. However, unlike in the Krylov method below, the matrices are not sparse. The time complexity of the Krylov method is essentially just that of 9 vector-vector operations due to the almost diagonal representation of $\cos^2\theta$.

Intuitively, $\mathcal{K}_m(V, |\Psi\rangle)$ can be thought of as approximately an eigenspace of V surrounding $|\Psi\rangle$, since $|\Psi\rangle$ stays in the space under the action of V.

The vectors in the definition (6.25) are most likely not orthognonal, as the repeated action of V turns them towards the eigenvector of V with the largest eigenvalue. Since V is Hermitian and sparse, an orthonormal basis $V_m = [\mathbf{v}_1, \mathbf{v}_2, \ldots, \mathbf{v}_m]$ of $\mathcal{K}_m(V, |\Psi\rangle)$ with $\mathbf{v}_1 = \beta|\Psi\rangle$ is found very efficiently using the Lanczos procedure (see Appendix B). The action of $\exp(-idtV/\hbar)$ on $|\Psi\rangle$ is then calculated as

$$\begin{aligned}\exp(-idtV/\hbar)|\Psi\rangle &\approx (V_m^H V_m)^{-1} V_m^H \exp(-idtV/\hbar)|\Psi\rangle \\ &= \beta V_m^H \exp(-idtV/\hbar) V_m \mathbf{e}_1 \\ &\approx \beta \exp(-idt V_m^H V V_m/\hbar)\mathbf{e}_1, \end{aligned} \tag{6.26}$$

where the first standard basis vector in the Krylov subspace $\mathbf{e}_1 = (1, 0, \ldots, 0)^T$ (representing $\mathbf{v}_1$) picks out the first column of the matrix exponential. Two key approximations are made. First, the matrix-vector product $\exp(-idtV/\hbar)|\Psi\rangle$ is approximated with the projection of the product onto the Krylov subspace. Recognize $(V_m^H V_m)^{-1} V_m^H$ as the projection operator onto the column space of V_m (also known as the pseudoinverse). Applied to $\exp(-idtV/\hbar)|\Psi\rangle$ it gives the least squares solution to the overdetermined system $V_m|x\rangle = \exp(-idtV/\hbar)|\Psi\rangle$, where $|x\rangle$ is the vector in the Krylov subspace to be found. Then, the many-dimensional problem is reduced to an m dimensional problem by approximating the projection of the matrix exponential with the matrix exponential of the projection. In the calculations, $m = 10$ suffices to accurately reproduce the results of using the full exponential of the laser interaction. The 3-diagonal $V_m^H V V_m$ matrix is directly available as output from the Lanczos procedure. The first column of the exponential of this 10×10 matrix is trivially calculated. The most expensive operation is calculating the 9 successive matrix-vector products $V|\Psi\rangle, V^2|\Psi\rangle, \ldots, V^9|\Psi\rangle$ for the Lanczos procedure. Here, the sparseness of V facilitates the process.

The above technique is justified by comparing with the truncated Taylor expansion

$$\exp(V)|\Psi\rangle \approx |\Psi\rangle + \frac{1}{2}V|\Psi\rangle + \cdots + \frac{1}{(m-1)!}V^{m-1}|\Psi\rangle. \tag{6.27}$$

Clearly, the truncated Taylor expansion is a member of $\mathcal{K}_m(V, |\Psi\rangle)$. Now, the projection operator $(V_m^H V_m)^{-1} V_m^H$ picks the vector from the Krylov subspace with the smallest distance from $\exp(V)|\Psi\rangle$. The above approximations are therefore better than simply truncating the Taylor expansion.

The entire process of applying this approximation to the state vector takes at most a few seconds, which should be compared with the 10 minutes for the diagonalization method. Avoiding the exponential of the full matrix has the added benefit of not having to store a huge matrix. Only the sparse V matrix must be stored. In this way, the memory requirement for handling V is brought down to a negligible amount.

The exponential of the W' matrix is calculated via diagonalization, as it must only be done once, and the Krylov subspace method seems to work a lot worse with this matrix, requiring $m > 300$ for the approximation to become reasonable.

6.2.4 Propagation in imaginary time: Initial state distribution

Substitution $dt \to idt$ gives a real phase in the time evolution operator

$$\exp(-i\mathcal{H}dt/\hbar) \to \exp\left(-\mathcal{H}dt/\hbar\right). \tag{6.28}$$

Propagation of an initial guess for the wave function in imaginary time [101]

$$\exp\left(-\mathcal{H}dt/\hbar\right)\Psi = \sum_n \exp\left(-E_n dt/\hbar\right) a_n |E_n\rangle \tag{6.29}$$

converges to the ground state (assuming $a_0 \neq 0$) because higher energy terms in the sum decay faster. Numerically, the wave function must be normed in each step to avoid drowning in round-off errors. Finally, the ground state energy is obtained by acting on the normed final wave function

$$E_0 = -\frac{\hbar}{dt} \ln\left|\exp\left(-\mathcal{H}dt/\hbar\right)\Psi_{\text{final}}\right|. \tag{6.30}$$

The higher lying states are found by projecting out all the lower lying states every few imaginary time steps, which ensures orthogonality. This method reproduces the bound state energies calculated with the BOUND program mentioned in Hutson and Thornley [91]. The BOUND program was run by Robert Zillich.

The initial thermal ensemble can be selected by giving each state a Boltzmann weight $w_n \propto \exp(-E_n/k_bT)$, although in this thesis, only the ground state has been used as the initial state, however with focal volume averaging taken into account.

It is noted, however, that higher lying states have been seen to lead to remarkably different long time alignment dynamics when exposed to weak alignment laser pulses. When kicked very gently, the different initial states apparently lead to alignment traces with widely different revival times, some longer than 1 ns even for HCCH-He. The revival time for HCCH in gas phase is just 14.2 ps. The much longer revival times are likely a consequence of the much slower orbital motion of the helium. At least some of revival times seem to correspond to the energy level difference between the bound states, first calculated for HCCH in Refs. 96, 102 and later reproduced by the simulation program. The different revival times could point towards an explanation for the missing or weak revivals in helium droplets as partially a consequence of a deviation from the regular energy level structure of isolated molecules. So far, these considerations are merely speculations, as the effects of a changed energy level structure on rotational revivals have only briefly been studied in this PhD project.

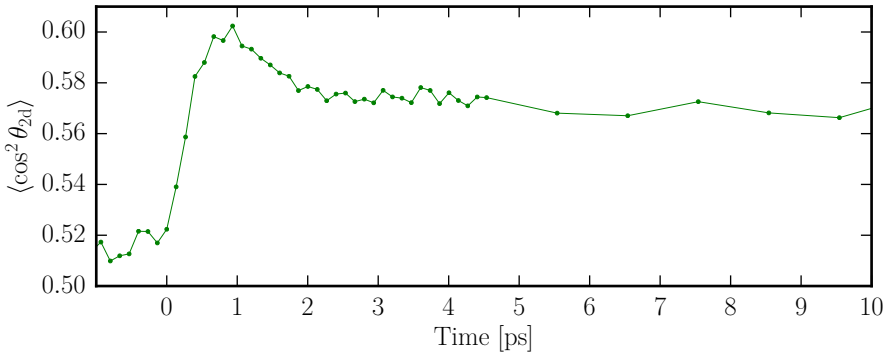

FIG. 6.2: Measured degree of alignment for CS_2 inside droplets characterized by $\langle\cos^2\theta_{2D}\rangle$. The parameters are $\tau = 330\,\text{fs}$ and $I_0 = 3.7 \times 10^{13}\,\text{W/cm}^2$.

6.3 Predictions

The original motivation for implementing this model was to understand the results shown in Figs 5.1 and 5.2 in the previous chapter. Particularly, the results of the fast behavior for CS_2 called for a better understanding of the two observed regimes of alignment behavior. Figure 6.2 expands on the early time for the CS_2 data shown in Fig. 5.2.

Figure 6.3 shows the time evolution of the probability density as function of the distance between the He atom and the molecular center of mass calculated for CS_2 and with the pulse configuration that was used in Fig. 6.2. The probability density $P(r)$ is calculated by averaging the wave function Ψ_N over all angles

$$P(r) = \int d\Omega d\Omega_r |\Psi_N(\mathbf{r}, \Omega)|^2. \tag{6.31}$$

Figure 6.3a) shows how a large fraction of the wave packet is ejected from the molecule after the pulse. Significant probability amplitude travels about 16 Å, reaching the simulation boundary after about 1 ps. This corresponds to a speed of roughly 1600 m/s in the center of mass frame, and a kinetic energy well above the binding energy. The simulation shows that the helium dissociates from the rotating molecule.

The simulation does not take more than one helium atom into account. However, assuming that the ejected helium atom travels the average He-He distance of 3.6 Å [50] before elastically colliding with the surrounding helium and travelling 3.6 Å back again with the same speed, a return time of 0.45 ps is obtained. Notice that this return time is for the fastest parts of the wave packet. When the reflected helium collides with the molecule, the free rotation of the molecule breaks down. This interpretation is in good agreement with the observed behavior in

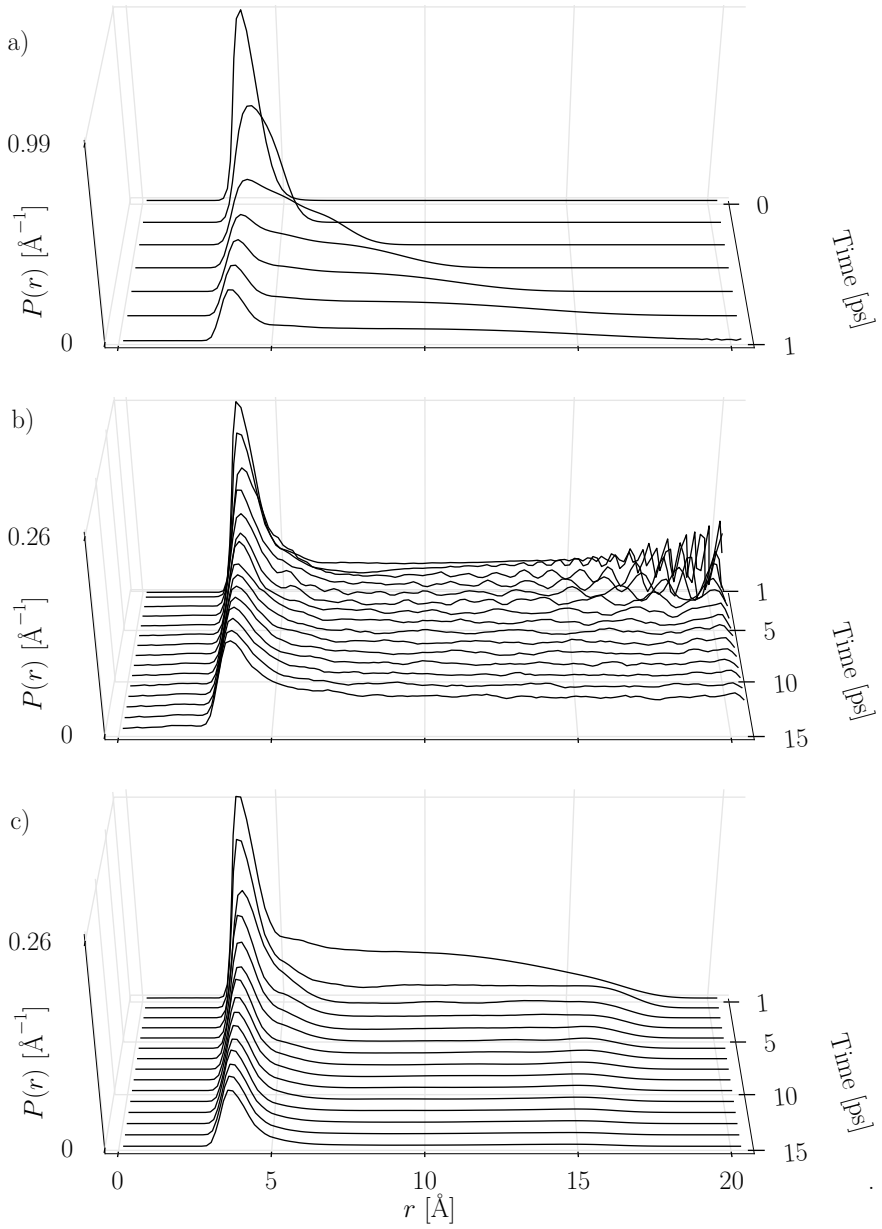

FIG. 6.3: Distributions of CS_2-He separation when the complex in its ground state is subjected to a 330 fs, 3.7×10^{13} W/cm^2 Gaussian pulse centered at $t = 0$. a) Early-time dynamics 0-1 ps. The ground state distribution is transformed by the pulse. b) Longer-time dynamics 1-15 ps. c) As b), but after employing absorbing boundary conditions.

Figs. 6.2 and 5.2, where the free rotation of CS_2 breaks down after about 1 ps. Possibly the ejected helium atoms in the droplet move slightly slower because of the increased inertia.

6.3.1 Boundary treatment: absorption of probability amplitude

It is apparent from the oscillatory counterpropagating wave pattern in Fig. 6.3b) that the wave packet reflects at the end of the simulation grid at $r = 20$ Å, which is unphysical, at least as far as the 1 helium model is concerned. The effect of using a finite grid is to impose the implicit condition that the wave function must be zero outside the grid, equivalent to a hard wall. The spurious reflections cause unphysical interactions between the molecule and the reflected atom, leading in turn to unphysical rotational behavior. In the light of the foregoing discussion, however, the hard wall may not seem like a bad way to model the surrounding helium.

In order to get realistic results for the molecule dynamics for times longer than 1 ps, the spurious reflections must be eliminated. To do so, the wave packet approaching the end of the spherical simulation cell $r \in [0, r_{max}]$ is removed by employing absorbing boundary conditions [103]. By multiplying the radial wave functions with a function that gradually goes from 1 to 0 between $r_{max} - \Delta$ and r_{max},

$$f(r) = \begin{cases} 1 & \text{for } r < r_{max} - \Delta \\ \exp\left[1 - \frac{1}{1-\left(\frac{r-(r_{max}-\Delta)}{\Delta}\right)^2}\right] & \text{for } r \geq r_{max} - \Delta \end{cases} \tag{6.32}$$

the reflections are almost completely removed. In the calculations, the number of absorbing grid cells N_Δ is 32, which means that absorption takes place over the distance $\Delta = N_\Delta \Delta r \approx 5$ Å. The effect of absorbing boundary conditions is seen in Fig. 6.3c). The absorption is improved by increasing Δ and hence the number of absorbing grid cells, and with a more gradual decrease of the multiplicative factor $f(r)$. This transfer function $f(r)$ is equivalent to a complex potential in the Hamiltonian with negative imaginary part. With a complex absorbing potential, the propagation is no longer unitary. Indeed the norm of the wave function is now a decreasing function of time.

Perhaps unintuitively, the absorbed probability amplitude at large r contains state information about the freely rotating molecule seemingly left behind. The molecular probability amplitude in the dissociating channels is lost to the boundary. In order to calculate any expectation value therefore, the molecular probability leaving the boundary must be accounted for. The expectation value for any observable A, depending only on the molecular state, e.g. $A = \cos^2\theta$, is calculated as

$$\langle A \rangle = \sum_{jj'JJ'LN} A^{j'J'}_{jLJN} \int_0^\infty dr\ u^*_{jLJN}(r) u_{j'LJ'N}(r). \tag{6.33}$$

Here, $A^{j'J'}_{jLJN} = \langle j'LJ'N|A|jLJN\rangle$ is a matrix element of A. Absorbing the radial wave function $u_{jLJN}(r)$ for large r modifies the weighting of the matrix elements, yielding a wrong expectation value. This information must be recorded before the probability is absorbed at the boundary and the information is lost. To do so, the probability current, defined in (6.35), at some radial distance R smaller than the start of the absorption zone is integrated over time. R should be large enough that $W(r \geq R) \approx 0$ for any angle $\theta_{\mathbf{r}}$. Furthermore, the laser pulse must have finished before any probability amplitude reaches $r = R$. Lastly, the centrifugal barrier $\hbar^2 L(L+1)/2\mu R^2$ should be much smaller than the rotational energy of the molecule $Bj(j+1)$ for all involved combinations of j and L. This is expected to be fulfilled because dissociation happens for molecules that rotate fast, and because R is chosen as large as possible. If these conditions are fulfilled, the coupled channel equations (6.5) decouple, and the expectation value becomes

$$\begin{aligned}\langle A\rangle = &\sum_{jj'JJ'LN} A^{j'J'}_{jLJN} \int_0^R dr\ u^*_{jLJN} u_{j'LJ'N} \\ &+ \sum_{jj'JJ'LN} A^{j'J'}_{jLJN}\ U_{jj'}(t) \int_0^t dt'\ U_{j'j}(t') I^{j'J'}_{jLJN}(R).\end{aligned} \tag{6.34}$$

where $U_{jj'}(t) = \exp\left(\frac{i(Bj(j+1)-Bj'(j'+1))}{\hbar}t\right)$ is a phase factor and the probability current is

$$I^{n'}_n(R) = \frac{i\hbar}{2\mu}\left[u_{n'}(r)\frac{\partial}{\partial r}u^*_n(r) - u^*_n(r)\frac{\partial}{\partial r}u_{n'}(r)\right]_{r=R}. \tag{6.35}$$

Here, $n = jLJN$ is a collective index. After accumulating the dissociated probability amplitude with a phase offset $U_{j'j}(t')$ as it leaves the $r = R$ surface, the phase factor $U_{jj'}(t)$ is responsible for all time evolution of the expectation value for the dissociated part of the wave packet. The expectation value inside the $r = R$ surface is calculated as normal. Note that for an isolated molecule, $\exp(-iBj(j+1)(t-t')/\hbar)$ is the time evolution operator for the $|jm\rangle$ stationary state. $U_{jj'}(t-t')$ evolves the product of expansion coefficients $u^*_{jLJN}(R)u_{j'LJ'N}(R)$ in time. That is, the probability amplitude that propagated through the $r = R$ surface at time t' in a small time step dt'. This time evolution is that of an isolated molecule, as could be expected. A derivation of this result following an idea from Robert Zillich is given in Appendix A.3.

This method is feasible since only the time integrals in (6.34) corresponding to the nonzero entries in the sparse matrix representation of $A = \cos^2\theta$ are needed. The remaining time integrals may be nonzero, but they are multiplied by a zero valued matrix element.

6.3.2 Dissociation probability: breaking-free

The effective moment of inertia of small molecules in helium droplets can be understood as being caused by a small number (about 10 or even less) of helium

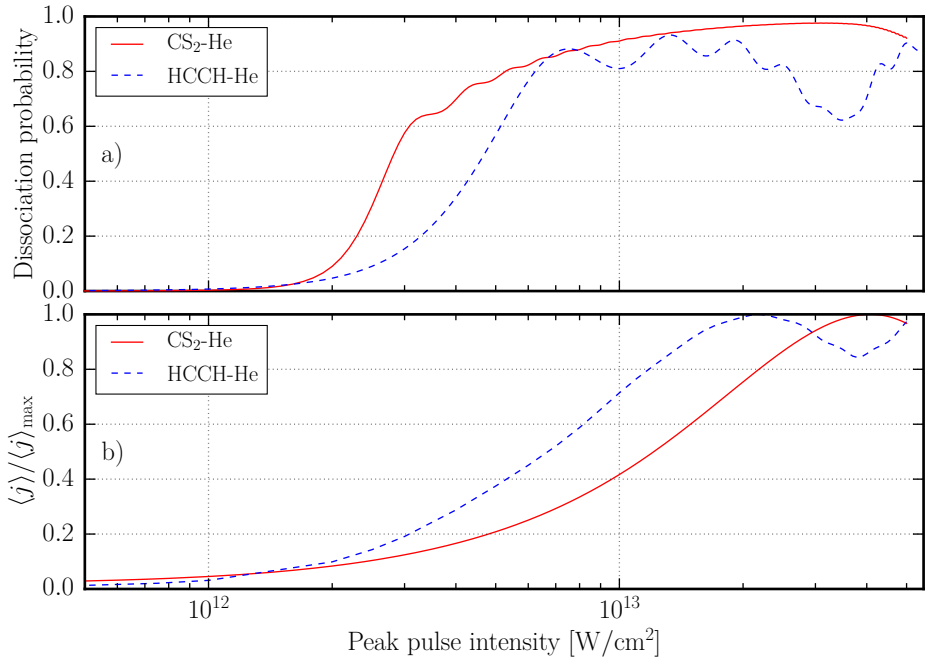

FIG. 6.4: a) Dissociation probability for CS_2-He and HCCH-He upon exciting the ground state with a 300 fs Gaussian pulse as function of peak intensity. b) The expectation value of the molecular angular monentum quantum number j for CS_2-He and HCCH-He under the same conditions as in a), immediately after the pulse. The expectation values have been divided by the maximum expectation value $\langle j \rangle_{\max} = 95.75$ for CS_2-He and $\langle j \rangle_{\max} = 8.63$ for HCCH-He.

atoms forming a solvation shell around the molecule [15]. In the case of OCS for example, only 6 atoms at the OCS-He potential minimum nicely explains the observed moment of inertia [50]. As seen above, the CS_2-He complex dissociated violently, with relative speeds of up to 1600 m/s. It seems reasonable to suppose that the same, high rotational energy causes ejection of the helium atoms from the solvation shell of the CS_2 molecule in helium droplets.

How low must the intensity become before the dissociation stops? To answer this question, the dissociation probability of CS_2-He and HCCH-He as a function of the laser pulse intensity for a fixed pulse duration of 300 fs is calculated. To calculate the dissociation probability, the wave function is projected down to the space of all bound states, spanned by the discrete field-free $V = 0$ energy eigenstates with energy $E < W(r = \infty) = 0$. The dissociation probability is then

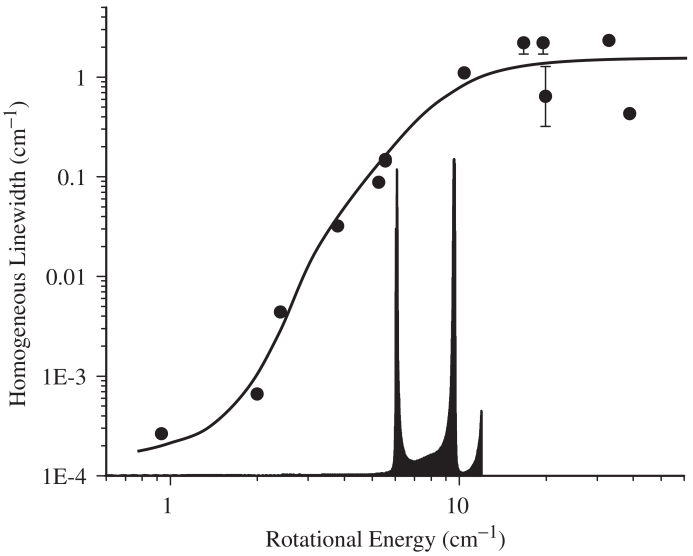

FIG. 6.5: Homogeneous linewidth observed for different molecules as a function of the excited state rotational energy. The density of states for the bulk helium excitations is also plotted (thereby excluding droplet compression and surface modes). The sharp increase in linewidth with increasing rotational energy correlates well with the location of the roton band of bulk helium. Excerpt from [15].

obtained from the square modulus of the projected wave function as

$$P_d = 1 - \sum_{\substack{J \\ E<0}} |\langle E, J, N|\Psi_N(t)\rangle|^2 \,. \tag{6.36}$$

Here, $|E, J, N\rangle$ is an energy eigenstate, and the projection is evaluated after the pulse. P_d is the probability that the kick pulse causes the complex to dissociate. Another more direct way to calculate the dissociation probability is to propagate the wave function to long times (hundreds of picoseconds). The dissociation probability can then be calculated as 1 minus the square modulus of the wave function that remains after the effects of the absorbing boundary. Such a calculation, which is a lot slower, is in good agreement with the results of the projection method.

The result is shown in Fig. 6.4a) (note the logarithmic first axis). For the CS_2 results presented earlier, a kick pulse intensity of $3.7 \times 10^{13}\,\mathrm{W/cm^2}$ is used. As can be seen, a reduction of the pulse strength of more than an order of magnitude is required in order to stop the dissociation completely. According to a simulation, just below the dissociation threshold a 300 fs kick pulse with an intensity of $1 \times 10^{12}\,\mathrm{W/cm^2}$ excites rotational levels in CS_2 essentially only up to

$j = 6$. This is also true if the moment of inertia is increased by a factor 3. This narrow wave packet can not be expected to align very well, particularly inside droplets due to blurring from nonaxial recoil.

With a rotational constant $B = 0.109\,\mathrm{cm}^{-1}$ [93] the rotational energy of the $j = 6$ state is as high as $4.6\,\mathrm{cm}^{-1}$. From Fig. 6.5, the rotationally-resolved linewidth would be expected to be roughly $0.8\,\mathrm{cm}^{-1}$. From the time-energy uncertainty principle

$$\Delta E \Delta t \geq \frac{\hbar}{2} \tag{6.37}$$

assuming that the (FWHM) linewidth corresponds to $2\Delta E$ and the lifetime corresponds to Δt when the equality holds, the lifetime τ_l is estimated from the linewidth ν given in cm^{-1} as

$$\tau_l = \frac{1}{2\pi(\nu c \cdot 100\,\mathrm{cm/m})}. \tag{6.38}$$

Inserting $\nu = 0.8\,\mathrm{cm}^{-1}$ gives a lifetime of about 100 ps. Increasing the intensity to $2 \times 10^{12}\,\mathrm{W/cm}^2$, which is near the dissociation threshold, gives a maximum rotational state $j \approx 12$, corresponding to a rotational energy of $17\,\mathrm{cm}^{-1}$. The lifetime here is only about 5 ps.

Acetylene HCCH of a given parity only supports a 2-level sine-like rotational wave packet before reaching the dissociation threshold of $7.4\,\mathrm{cm}^{-1}$ [96], which incidentally is close to the roton energy gap ($\sim 6\,\mathrm{cm}$) [104]. With a rotational constant of $1.18\,\mathrm{cm}^{-1}$, the rotational energy gives a lifetime of roughly 20 ps.

Are the linewidth results in the well-known Fig. 6.5 related to a centrifugal breakup of the helium solvation shell? These results certainly seem to suggest that this is the case, since the onset of dissociation correlates with the onset of broader lines in the figure, that again correlate with the roton energy. Is there some deeper connection between the roton band gap and the rotational energy required for breaking loose attached helium? Or is the correlation just a coincidence in the case of CS_2-He and HCCH-He? As will be discussed below, an alternative explanation having to do with the velocity of the outermost helium atoms exceeding the Landau velocity also seems to explain some of the observed experimental results. Perhaps a centrifugal breakup of the solvation shell complements the description of rotational decay as being caused by couplings with bulk helium excitations.

Regardless of the cause of the increasing linewidths, it is clear from these results that heavier molecules than CS_2 and HCCH must be used if the aim is to see rotational revivals inside helium droplets. The region of kick pulse intensities that do not lead to dissociation must support wave packets that are broad enough to give appreciable alignment (see Fig. 6.4a)). This conclusion gives quantitative confirmation of the speculations of Jens Hedegaard Nielsen [53, pp. 132–135].

One early aim of the new helium droplet machine presented in chapter 4 was to be able to align HCCH in droplets. The very isotropic HCCH-He interaction potential and its short revival time ($\sim 14\,\mathrm{ps}$) was though to permit alignment

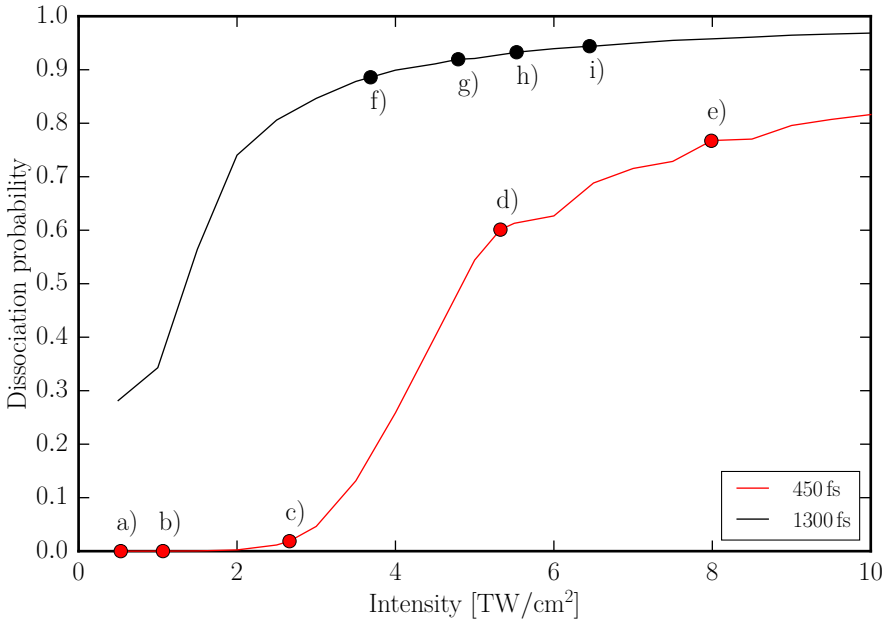

FIG. 6.6: Dissociation probability calculated for I_2-He upon exciting the ground state with a 450 fs (red) and 1.3 ps (black) pulse as a function of the peak intensity. The dots on the curves are the dissociation probabilities calculated for the pulses used in the experiments presented on page 71. The point labels correspond to the panel labels in Fig. 5.6. Fine structure in the dissociation probability curves is not captured due to a too large sample spacing.

revivals. The above considerations, however, lead instead to looking at heavier molecules, in particular I_2, of which results have been presented in chapter 5. The dissociation probability for I_2-He is shown in Fig. 6.6. The dissociation probability is calculated for the two pulse durations that are used in the experiments. From the simulations, it is seen that I_2-He supports a rotational wave packet with up to $j \approx 18$ before dissociating. This is because of the deeper I_2-He potential well, which supports many more bound states. Additionally, the much heaver I^+ fragments are ejected from the droplet with less deviation from axial recoil. So there is a better opportunity for observing revivals. Incidentally, the increased number of bound states makes the calculation (6.36) more time consuming.

The labeled dots in Fig. 6.6 indicate the dissociation probability calculated for I_2-He when subject to the same pulses that are used in the experiments (see Fig. 5.6) on page 71. Note that there is neglicible dissociation probability for the first three intensities, where coherent rotational behavior was observed for

I_2 molecules in droplets. The coherence is quenched for the panels d) and e), where the calculated dissociation probability coincidentally rises. In panels f)-i), the fast feature at the first few ps manifests itself. This coincides with the high likelyhood of helium ejection predicted by the simulation, and does not seem to be explainable from Fig. 6.5 alone.

The experimental results can also be reasoned about with Fig. 6.5. According to a gas phase simulation (and a gas phase simulation with a 3 times higher moment of inertia), a wave packet containing states up to $j \approx 18$ is induced with the pulse used in experiment c). For I_2, $B = 0.037\,37\,\mathrm{cm}^{-1}$ [93] The lifetime expected from Fig. 6.5 is only 5 ps, which is much shorter[3] than the coherent dynamics observed at around 650 ps. However, roughly half the wave packet is made up of states below $j = 10$, which all have an expected lifetime longer than 650 ps. At the very lowest intensity used in Fig. 5.6 panels a) and b), all states should have lifetimes of several nanoseconds. Like the result that there should be no dissociation, this result does not explain the decay of alignment observed for the lowest intensity experiment. The disagreement must at least partially be due to the quadrupole effect mention in chapter 5.

The reader may be left wondering: Why does the dissociation probability sometimes decrease with increasing intensity, as seen in Fig. 6.4a)? Both quantum and classical physics offer an explanation. Classically, as the molecules that are initially close to the alignment axis are rotated faster by the increasing pulse strength, at some point they will rotate past the alignment axis before the pulse is over. After crossing the $\theta = 0$ axis, the remaining pulse causes the molecules to slow down again, thereby loosing energy that would otherwise have been put into ejecting helium. Quantum mechanically, as the energy level spacing increases (see (2.11)), an increase in the pulse intensity leads to a relatively slower population of the higher states, giving the lower states more time to mix. Thus $\langle j \rangle$ and thereby the rotational energy dips down, as is seen in Fig. 6.4b).

6.4 Classical description

The experimental results for I_2 molecules in helium droplets presented in chapter 5 could be rationalized in terms of a simplified quantum mechanical model. According to the model, the disappearance of the revivals is likely due to centrifugal breakup of the solvation shell and the ensuing interactions between the rotating molecule and excited cloud of helium atoms around it, or possibly the "walls" collapsing in on the molecule as the excited atoms move away. At higher intensities, the ejection of helium is so violent that the molecule breaks free from the environment an rotates freely for a few ps. This interpretation is in good agreement with the observed fast dynamics that occur for high kick pulse fluences in both I_2 and CS_2. Importantly, the simplified quantum mechanical description can not relate these findings to the bulk excitations such as rotons in the surrounding

[3] Actually it is about 500 ps if the rotational energy is interpreted as the energy difference between states separated by $\Delta J = 2$.

helium. The rotational energy threshold for exciting rotons is surprisingly close to the threshold for dissociating helium, however.

Inspired by the rotational dissociation results from the quantum mechanical model, my supervisor Henrik Stapelfeldt extended a simple classical model [59–61] to take into account the increased effective moment of inertia due to a He-solvation shell [15, 50]. Here, I reproduce some of Henriks results and extend them with my own observations.

Assuming a linear molecule is initially stationary, a kick pulse induces planar rotation with an angular velocity ω given by integrating up the torque (2.7) over the pulse duration. A result which assumes that the molecule and its rigidly attached solvation shell is stationary for the duration of the pulse is

$$\omega = \frac{1}{2}\frac{\Delta\alpha F}{I_{\text{eff}}\varepsilon_0 c}\sin(2\theta_0), \tag{6.39}$$

where

$$F = \int_{-\infty}^{\infty} I(t)dt \tag{5.2}$$

is the fluence and

$$I_{\text{eff}} = I + I_{\text{He}} \tag{6.40}$$

is the effective moment of inertia for the molecule I and helium shell I_{He}. Initially, the molecule is at an angle θ_0 with the laser pulse and ε_0 and c is the vacuum permittivity and speed of light, respectively. The simplest criterion for dissociation of helium is

$$E_{\text{rot}} > E_b, \tag{6.41}$$

where $E_{\text{rot}} = \frac{1}{2}I_{\text{He}}\omega^2$ is the rotational energy of the helium shell and E_b is the binding energy. This criterion translates to

$$\omega > \sqrt{\frac{2E_b}{I_{\text{He}}}} \tag{6.42}$$

or

$$F_d = \frac{I_{\text{eff}}c}{\pi\Delta\alpha'\sin(2\theta_0)}\sqrt{\frac{E_b}{2I_{\text{He}}}}, \tag{6.43}$$

where it is used that $\sin(2\theta_0) > 0$, where α is expressed as the polarizability volume $\Delta\alpha' = 4\pi\varepsilon_0\Delta\alpha$ and where F_d is the fluence required for dissociation. The binding energy is estimated from the depth of the molecule-helium potential.

With this model, the coupling with rotons can be taken into account by assuming that they will be excited as soon as the linear speed of the outermost helium atoms exceeds the Landau velocity. The criterion for creating rotons is

$$\omega r_{\text{He}} \geq v_L, \tag{6.44}$$

or

$$F_L = \frac{I_{\text{eff}}c}{\pi\Delta\alpha'\sin(2\theta_0)}\frac{v_L}{2r_{\text{He}}}, \tag{6.45}$$

where F_L is the fluence required to create rotons, r_{He} is the distance from the center of rotation to the outermost helium atom and $v_L \approx 56\,\mathrm{m/s}$ is the Landau velocity in helium droplets [20].

It is unclear how many helium atoms to place in the potential and where. Probably the average He-He distance in the droplets of 3.6 Å [50] together with the distance from the center, which gives a circumference, can be used to estimate the number of He atoms in a ring around a cylindrically symmetric molecule.

For I_2 in helium droplets, Robert Zillich calculated $I_{\mathrm{eff}} = 1.67I$ with a quantum Monte Carlo method [105]. Although this factor (1.67) is quite low compared to the factor 3 usually expected for other molecules, it makes sense, since iodine is so heavy and yet small. The few helium atoms that can fit around an I_2 molecule won't change the moment of inertia much.

Assuming that the outermost helium atom is positioned in the potential well furthest from the center at $r_{\mathrm{He}} = 4.828\,\text{Å}$ at a potential depth of $E_b = 44.28\,\mathrm{cm}^{-1}$ [97], this is enough to determine the critical fluences for exciting rotons and for dissociating:

$$F_L = 1.1\,\mathrm{J/cm}^2 \tag{6.46}$$

$$F_d = 4.10\,\mathrm{J/cm}^2. \tag{6.47}$$

Here, the most favorable initial angle $\theta_0 = 45°$ has been assumed. The ground state energy differs significantly from the potential depth. The simulation program presented above gives a ground state energy of $15.78\,\mathrm{cm}^{-1}$, which is in good agreement with Ref. 97. Using this value for the binding energy instead gives

$$F_d = 2.45\,\mathrm{J/cm}^2. \tag{6.48}$$

These fluences ($1.1\,\mathrm{J/cm}^2$ and $2.45\,\mathrm{J/cm}^2$) are between the fluences used in the experiments Fig. 5.6 b)-c) and c)-d) (see page 71), and are not at all far from the fluence that separates coherent rotation from fast initial behavior. The dissociation threshold predicted by the quantum model is about the same, $2.6\,\mathrm{J/cm}^2$. However, the two models are not exactly comparable, as the quantum model only treats one atom, while the classical model treats the entire solvation shell. If anything, the comparison shows that if the molecule-He complex can dissociate, then the solvation shell is also not far from breaking up.

It is again interesting to note that the two criteria, roton excitations on the one hand, and dissociation on the other again agree on roughly the same fluence. It is interesting to divide the critical fluence for each criteria:

$$\frac{F_d}{F_L} = \frac{r_{\mathrm{He}}}{v_L}\sqrt{\frac{2E_b}{I_{\mathrm{He}}}}. \tag{6.49}$$

If $F_d/F_L < 1$ dissociation happens before coupling to rotons, while if $F_d/F_L > 1$ rotons are excited first. Note that this fraction neither depend on the initial angle θ_0, I_{eff} nor on $\Delta\alpha$. For I_2, $F_d/F_L \approx 1$ depending on the exact binding energy used. Since roughly $I_{\mathrm{He}} \propto r_{\mathrm{He}}^2$, only a weak dependence on the solvation shell

geometry of the fraction (6.49) can be expected. Furthermore note that while I_{He} is proportional to the number of helium atoms, the number of helium atoms goes up as E_b increases, since the deeper well has room for more atoms. Thus (6.49) can only depend weakly on the molecule at all.

It would be interesting to find molecules where either $\frac{F_d}{F_L} \ll 1$ or $\frac{F_d}{F_L} \gg 1$, corresponding to either dissociation happening long before coupling to rotons or vice versa. Is that possible? Probably not, given the above discussion, however, some testing of (6.49) with real numbers should be tried. Would it even make sense to have a situation where the solvation shell is destroyed but where the remaining helium cannot be interacted with? The converse, namely having an intact solvation shell moving fast enough to suddenly experience friction with the surrounding environment seems intuitively more plausible. What would the alignment dynamics be like if the intact solvation shell is slowed by friction?

6.4.1 Impact of dissociation on alignment

With the development of the theory behind (6.34) for calculating observables even after absorbing the wave packet at the boundary, it may seem odd that this result has not been used yet. As it turned out, the fact that the helium dissociates at all is the major result. The importance of this result was not realized before the theory behind (6.34) had been developed.

In order to show the results of implementing (6.34), a few alignment traces are presented here. The main purpose is to whet the appetite of a potential future student working with alignment of molecule-atom complexes.

In Fig. 6.7, alignment of CS_2-He below and above the dissociation threshold is compared. The panels on the left a)-d) are for a strong pulse, whereas the panels on the right e)-h) are for a weak pulse below the dissociation threshold. The upper half of the figure expands on the initial 160 ps of the lower half of the figure. Panels a),c),e) and g) are as panels b),d),f),h), respectively, but are calculated for isolated molecules for comparison.

In panel b), the strong pulse causes the helium atom to rapidly dissociate. As a results, the alignment trace looks very similar to the gas phase trace a), only the amplitudes of the revivals and the permanent alignment level are reduced slightly, due to the loss of angular momentum to the ejected helium atom. On a long time scale c)-d), there is no new dynamics, since the helium atom has been ejected and no longer perturbs the free rotation of the molecule.

In panel f), the weaker pulse does not lead to ejection of the helium atom. The alignment dynamics differ from e) already within the first revival time. As can be seen, the revivals are delayed slightly and look differently. At long times h), the alignment dynamics is radically different than for the isolated molecule g). The trace is no longer periodic, at least not with the same rotational period, and a very slow oscillation with a period of almost 1 ns appears. This period is likely related to the orbital dynamics of the helium atom.

In Fig. 6.8, alignment dynamics is shown for HCCH and HCCH-He after a kick pulse with a fluence well above the dissociation threshold. The revivals

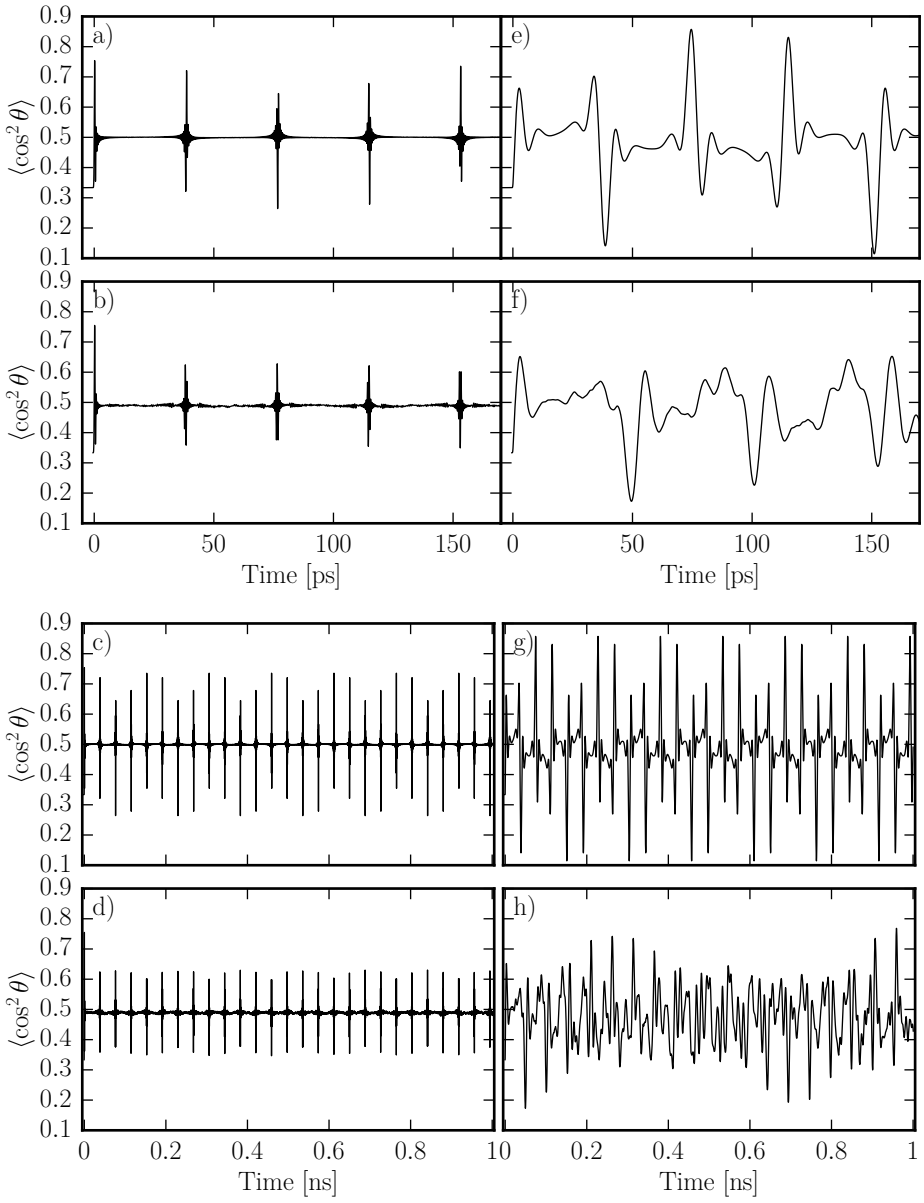

FIG. 6.7: The degree of alignment, represented by $\langle\cos^2\theta\rangle$, as a function of time. a) Isolated CS_2 molecules. b) CS_2-He complexes. c) and d) as a) and b), respectively, but for a longer time window. The intensity of the laser pulse was $3.7 \times 10^{13}\,\mathrm{W/cm^2}$ and the duration 330 fs. e)-h) as a)-d), respectively, but with a $2.0 \times 10^{12}\,\mathrm{W/cm^2}$, 300 fs pulse, i. e. a weaker pulse. The calculations are averaged over the focal volume and started from the ground state.

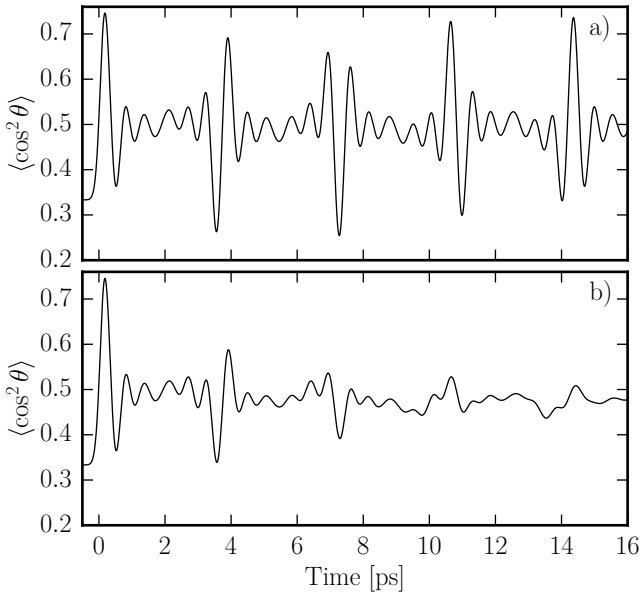

FIG. 6.8: The degree of alignment, represented by $\langle\cos^2\theta\rangle$, as a function of time. a) Isolated HCCH molecules. b) HCCH-He complexes. The intensity is $2.0 \times 10^{13}\,\mathrm{W/cm^2}$ and the duration 300 fs. The calculations are averaged over the focal volume and started from the ground state.

for HCCH-He decay and are almost completely gone after one rotational period. They do not re-appear even after 1 ns. As HCCH has much less rotational inertia, it is more strongly perturbed by the interaction with the helium, and coherence is lost. The dissociation time is comparable to the rotational period of HCCH, which is reflected in the time it takes for the revivals to decay.

For a kick pulse below the dissociation fluence, essentially only a 2-state wave packet can be excited from the ground state. This leads to just a sinusoidal alignment trace, and it is very difficult to tell the difference between the alignment dynamics for HCCH and HCCH-He. However, in the Fourier spectrum, periods as large as 22.8 ps can be identified. This period, which corresponds to an energy of $1.46\,\mathrm{cm^{-1}}$, is in agreement with the smallest difference between energies of stationary states of HCCH-He for even J calculated in Ref. 96.

6.5 Summary

To summarize, it has been shown that a quantum mechanical calculation of the dynamics of a linear molecule with a weakly bound atom after a strong laser pulse is feasible, provided an accurate molecule-atom potential energy surface is

available. This has been demonstrated for HCCH-He, CS_2-He and I_2-He. For molecule-atom complexes, two distinct regimes are identified. For low intensity pulses, the atom stays attached to the molecule and influences the rotational dynamics of the molecule. For high intensity pulses, the atom quickly ($\sim$ few ps) breaks free from the molecule, and the molecule rotates freely hereafter.

This result has been related to the experimental results for I_2 molecules aligned in helium droplets presented in chapter 5. It is assumed that centrifugal breakup of the solvation shell in helium droplets occurs at roughly the same kick pulse fluences that lead to ejection of the helium atom in the molecule-he complex. Under this assumption, the quantum model predicts centrifugal breakup at the same kick pulse fluences where the experiment shows loss of rotational coherence. The appearance of fast rotational dynamics at high kick pulse fluences for I_2 and CS_2 in helium droplets are rationalized as being caused by rapid ejection of helium atoms, leading to free rotation. The free rotaion is short lived, though, because the rest of the droplet crushes in on the molecule shortly hereafter.

A classical model which is in rough agreement with both the quantum model and the experiments partly elucidates the connection between rotational breakup and coupling to rotons in the bulk. The classical model points towards the result that roton excitations become available at the same kick pulse fluences that lead to centrifugal breakup of the solvation shell, independently of the molecule. The robustness of this result has not yet been tested by actually comparing with other molecules than I_2.

CHAPTER 7

Conclusion and outlook

The focus of this PhD project has been on improving the understanding of 1D laser-induced alignment and rotation of molecules embedded in superfluid helium nanodroplets. The work is motivated by the strong contrast between rotationally-resolved spectra and the historical results of aligning molecules inside helium droplets.

In the first part of this thesis, the theory of alignment for isolated molecules is reviewed, and it is extended to include ways of treating $\langle \cos^2 \theta_{2D} \rangle$, which is the characterization of alignment used experimentally. A new result is that $\langle \cos^2 \theta_{2D} \rangle$ can be calculated, even very efficiently, for linear and symmetric top molecules. Another new result is that in the case of a linear molecule, $\langle \cos^2 \theta \rangle$, the primarily theoretical characterization of alignment, can be efficiently reconstructed via Fourier analysis of measurements of $\langle \cos^2 \theta_{2D} \rangle$ alone. The effect of measuring only two velocity components in Coulomb explosion imaging is to introduce new frequencies in the recorded alignment spectra. These frequencies can be identified and removed. New fine structure (higher order revivals) in $\langle \cos^2 \theta_{2D} \rangle$ traces that survive experimental smearing effects (thermal and focal volume averaging) have been identified. Normally, this structure masquerades as experimental noise. However, careful Fourier analysis shows the fingerprint of this fine structure in experimental data.

The theory of alignment of isolated molecules together with the new theory of $\langle \cos^2 \theta_{2D} \rangle$ is incorporated into an efficient and user-friendly 1D alignment simulation program with many practical uses. Comparisons of simulations with experiments show that the theory for $\langle \cos^2 \theta_{2D} \rangle$ is in excellent agreement with experiments. Several applications of this simulation program are demonstrated. For example, by directly comparing simulations to the alignment of molecules

inside helium droplets (after deconvolving nonaxial recoil), the droplet temperature was estimated to be between 0.2 K and 0.5 K, in agreement with an expected temperature of 0.37 K [14]. To my knowledge, this constitutes the first ever determination of the droplet temperature by means of molecular alignment. The temperature determination could potentially be improved by also taking into account the effects of probe selectivity.

A better understanding of nonaxial recoil and probe selectivity would in general provide for the most precise comparisons with experimental results. A direction has been given for incorporating these effects into the theory of alignment in the future.

The new droplet machine recently built in Femtolab by Benjamin Shepperson is described. With this machine, new impulsive alignment experiments on isolated I_2 and I_2 molecules inside helium nanodroplets were conducted. These results show striking new alignment dynamics of both isolated I_2 and I_2 inside droplets. The isolated molecules show alignment behavior that deviates from the normal alignment theory. In particular, a partial decay of rotational angular momentum, consistent with a $\Delta J = \pm 1$ rule is observed. This effect is tentatively ascribed to quadrupole interactions with the iodine nuclei. In spite of this self-decay, the experiments on molecules in droplets show several new, never observed before features of alignment in helium droplets. Clear signs of coherent rotational motion are observed, most striking of which is a revival-like feature between 550–750 ps that seems to be positioned independently of the kick pulse fluence. At higher fluences, however, this feature disappears along with other signs of rotational coherence. Instead, a new fast structure emerges immediately after the pulse, similar to the one observed for CS_2 in helium droplets.

The new results are rationalized with two simplified models. The first model describes a linear molecule with a weakly bound atom quantum mechanically. Simulations using this model were first made feasible after implementing several optimizations. This model shows that the helium atom easily dissociates centrifugally even with relatively weak alignment pulses. The centrifugal dissociation threshold calculated with this model matches incredibly well with the transition between coherent rotation and fast dynamics observed in the I_2 alignment experiments in helium droplets. In this way, the observed fast alignment dynamics is rationalized as being caused by rapid breakup of the helium solvation shell. The breakup leaves the molecule in a small cavity which subsequently collapses, destroying the rotational coherence. Much the same result is obtained in a simple classical model. The classical model further predicts that below the threshold for centrifugal breakup, the highest linear speed of the molecule and solvation shell structure is below the Landau velocity. That would explain the existence of rotational coherence at low kick pulse fluences.

It seems like impulsive alignment of molecules in helium droplets has been reconciled with rotationally-resolved spectroscopy. However, studies of other, heavier molecules are needed in order to confirm the developed theory.

In parallel with the work presented in this thesis, the group of Mikhail Lemeshko has developed what is known as angulon theory [106, 107] based on many-body

physics. Angulons are quantum rotors "dressed" by quantum fields. Angulons offer a different approach to describing the solvation shell of atoms around a molecule in superfluid helium. Although not shown in this thesis, the angulon theory in its current form seems to capture at least some of the observed dynamics of impulsively aligned I_2 molecules in helium droplets, particularly at the lowest fluences.

Appendices

APPENDIX A

Selected derivations

In this appendix, results mentioned in the main text are derived.

A.1 Gaunt coefficient trick on an expansion in rotation matrices

For the observable $\mathcal{O}(\Omega) = \sum_{JKM} a^J_{M,K} \langle \Omega | JKM \rangle$, the matrix elements $\mathcal{O}^{J'}_{JKM} = \langle J'KM|\mathcal{O}|JKM\rangle$ are by definition [58]

$$\begin{aligned}
\mathcal{O}^{J'}_{JKM} &= \sqrt{\frac{2J'+1}{8\pi^2}} \int \mathscr{D}^{J'}_{M,K} \left(\sum_{J''K''M''} a^{J''}_{M'',K''} \right. \\
&\quad \left. \times (-1)^{M''-K''} \sqrt{\frac{2J''+1}{8\pi^2}} \mathscr{D}^{J''}_{-M'',-K''} \right) (-1)^{M-K} \sqrt{\frac{2J+1}{8\pi^2}} \mathscr{D}^{J}_{-M,-K} d\Omega \\
&= \frac{\sqrt{(2J+1)(2J'+1)}}{8\pi^2} \sum_{J''K''M''} a^{J''}_{M'',K''} (-1)^{M''-K''+M-K} \sqrt{\frac{2J''+1}{8\pi^2}} \\
&\quad \times \int \mathscr{D}^{J''}_{-M'',-K''} \mathscr{D}^{J'}_{M,K} \mathscr{D}^{J}_{-M,-K} d\Omega \\
&= \frac{\sqrt{(2J+1)(2J'+1)}}{8\pi^2} \sum_{J''K''M''} a^{J''}_{M'',K''} (-1)^{M''-K''+M-K} \sqrt{\frac{2J''+1}{8\pi^2}} \\
&\quad \times 8\pi^2 \begin{pmatrix} J & J' & J'' \\ -K & K & -K'' \end{pmatrix} \begin{pmatrix} J & J' & J'' \\ -M & M & -M'' \end{pmatrix}
\end{aligned} \tag{A.1}$$

$$= (-1)^{M-K} \sqrt{\frac{(2J+1)(2J'+1)}{8\pi^2}} \times \sum_{J''} a_{0,0}^{J''} \sqrt{2J''+1} \begin{pmatrix} J & J' & J'' \\ K & -K & 0 \end{pmatrix} \begin{pmatrix} J & J' & J'' \\ M & -M & 0 \end{pmatrix} \tag{A.2}$$

where in the last step, the property of 3j symbols that the bottom row must sum to zero has been used. The general matrix element (2.23) is obtained by putting primes on M and K in the first rotation matrix element and following through.

A.2 Taking probe selectivity and nonaxial recoil into account

In this section, the claims of section 2.2.4 are proven.

Probe selectivity: The probability density for the direction Ω of the molecule is given by fundamental quantum mechanics as $P(\Omega) = \Psi^*(\Omega)\Psi(\Omega)$, where $\Psi(\Omega)$ is the rotational wave function. The nonuniform detection probability $W_\rho(\Omega)$ implied by the probe selectivity modulates the observed probability $P(\Omega) \to P(\Omega)W_\rho(\Omega)$. The probability of detecting a molecule pointing along the infinitesimal solid angle $d\Omega$ is therefore $d\Omega \cdot P(\Omega)W_\rho(\Omega)$. The observable $\mathcal{O}$ is thus weighted by the total probability:

$$\langle \mathcal{O}_{\text{with probe selectivity}} \rangle = \int d\Omega \Psi^*(\Omega)\Psi(\Omega) \cdot (W_\rho(\Omega)\mathcal{O}(\Omega)) \,. \tag{A.3}$$

This is the quantum mechanical definition of the expectation value of $W_\rho(\Omega)\mathcal{O}(\Omega)$. By finding the matrix elements of $W_\rho(\Omega)\mathcal{O}(\Omega)$, expectation values for $\mathcal{O}$ with probe selectivity taken into account can be evaluated efficiently.

Nonaxial recoil: Given that the molecule points in some direction Ω, nonaxial recoil is a probability $P(\Omega'|\Omega)$ that another direction Ω' is actually measured. The expectation value of measuring $\mathcal{O}(\Omega')$, given that the molecule points along Ω is then

$$\langle \mathcal{O}' \rangle |_{\Omega} = \int \mathcal{O}(\Omega') P(\Omega'|\Omega) d\Omega'. \tag{A.4}$$

The expectation value $\langle \mathcal{O}' \rangle |_{\Omega}$ integrated over the probability distribution for pointing in the direction Ω, $P(\Omega) = \Psi^*(\Omega)\Psi(\Omega)$ is

$$\begin{aligned}
\langle \mathcal{O}' \rangle &= \int \langle \mathcal{O}' \rangle |_{\Omega} P(\Omega) d\Omega \\
&= \int \int \mathcal{O}(\Omega') P(\Omega'|\Omega) d\Omega' P(\Omega) d\Omega \\
&= \int d\Omega P(\Omega) \left(\int \mathcal{O}(\Omega') P(\Omega'|\Omega) d\Omega' \right) \\
&= \int d\Omega \Psi^*(\Omega)\Psi(\Omega)\widetilde{\mathcal{O}} = \left\langle \widetilde{\mathcal{O}} \right\rangle .
\end{aligned} \tag{A.5}$$

Thus the matrix elements of the observable

$$\widetilde{\mathcal{O}} = \int \mathcal{O}(\Omega') P(\Omega'|\Omega) d\Omega', \tag{A.6}$$

permit efficient evaluation of observables with nonaxial recoil taken into account. If further $P(\Omega'|\Omega) = P(\Omega' - \Omega)$, i. e. the probability can be expressed as only a function of the difference between the two orientations, then (A.6) is a spherical convolution, which can be calculated efficiently.

Nonaxial recoil *and* probe selectivity: The expectation value for $\widetilde{\mathcal{O}}$ with probe selectivity taken into account is by (A.3) given as

$$\left\langle \widetilde{\mathcal{O}}_{\text{with probe selectivity}} \right\rangle = \int d\Omega \Psi^*(\Omega)\Psi(\Omega) \underbrace{\left(W_\rho(\Omega)\widetilde{\mathcal{O}} \right)}_{\mathcal{O}_{\text{total}}(\Omega)} . \tag{A.7}$$

The matrix elements of

$$\mathcal{O}_{\text{total}}(\Omega) = W_\rho(\Omega) \int \mathcal{O}(\Omega') P(\Omega'|\Omega) d\Omega' \tag{A.8}$$

then permit efficient evaluation of the degree of alignment with both probe selectivity and nonaxial recoil taken into account. Note that this is in agreement with the expectation that probe selectivity should be accounted for *before* any nonaxial recoil occurs. The laser should ionize the molecule first, before the fragments can recoil and deviate from a straight line. In (A.7), the probability of measuring a direction Ω' is weighted by the probability of detecting the direction Ω.

A.3 Keeping track of absorbed probability

To account for the lost molecular probability amplitude due to the absorbing boundary in section 6.3.1, the probability current is integrated up just before it hits the absorbing boundary. To see how this works, pick R large enough that $W(r > R) \approx 0$ for all angles $\theta_{\mathbf{r}}$. Further, no probability amplitude should reach $r = R$ before the pulse is over. Then $W = 0$, and the coupled channel equations (6.5) reduce to the Schrödinger equation for a particle in a constant potential

$$i\hbar \dot{u}_n(r) = -\frac{\hbar^2}{2\mu}\frac{\partial^2}{\partial r^2}u_n(r) + E_{jL}^{\text{ang}}(r)u_n(r), \tag{A.9}$$

where $n = jLJN$ is a collective channel index and for large r

$$E_{jL}^{\text{ang}}(r) = \frac{\hbar^2 L(L+1)}{2\mu r^2} + Bj(j+1) \approx Bj(j+1) \equiv E_j^{\text{rot}}. \tag{A.10}$$

At $r > R$, the channels are no longer coupled, since no primed channels occur in (A.9). The expectation value (6.33) is split up

$$\langle A \rangle = \sum_{jj'JJ'LN} A_{jLJN}^{j'J'} \int_0^R dr\; u_{jLJN}^* u_{j'LJ'N} + \sum_{jj'JJ'LN} A_{jLJN}^{j'J'} \int_R^\infty dr\; u_{jLJN}^* u_{j'LJ'N}. \tag{A.11}$$

The first term is calculated as usual, but the other term is replaced by using the continuity equation $\frac{\partial \rho_w}{\partial t} = -\frac{\partial j_w}{\partial r} + \sigma(r,t)$. Setting the weight density $\rho_w = u_n^*(r)u_{n'}(r)$ and assuming the source term σ is zero, the infinite integral

$$\int_R^\infty dr\; u_{jLJN}^* u_{j'LJ'N} = \int_0^t dt'\; j_w(R) \tag{A.12}$$

is replaced by a *finite time* integral of the current $j_w(R)$. After evaluating $\dot{\rho}_w$ using (A.9) (and the complex conjugate of (A.9)), the current and source terms are identified as

$$j_w(R) = \frac{i\hbar}{2\mu}\left[u_{n'}(r)\frac{\partial}{\partial r}u_n^*(r) - u_n^*(r)\frac{\partial}{\partial r}u_{n'}(r)\right]_{r=R} \tag{A.13}$$

$$\sigma = \frac{i(E_j^{\text{rot}} - E_{j'}^{\text{rot}})}{\hbar}\rho_w(r). \tag{A.14}$$

The diagonal source term is zero, as could be expected since ρ_w is then just the probability density $|u_n(r)|^2$, and probability must be conserved. The off-diagonal source term is non-zero because of the constant potential. The total weight is not conserved, and the analysis has broken down! However, a rescaling of the radial wave function

$$w_n = \exp\left(\frac{iE_j^{\text{rot}}}{\hbar}t\right)u_n \tag{A.15}$$

leading to a new weight density $\rho_w \to \tau_w = w_n^* w_{n'}$ can be shown to remove the source term. This is seen by applying the continuity equation on τ_w instead of ρ_w. In this way $\langle A \rangle$ can be calculated by integrating up the current corresponding to the conserved τ_w

$$\begin{aligned}\langle A \rangle = &\sum_{jj'JJ'LN} A_{jLJN}^{j'J'} \int_0^R dr\ u_{jLJN}^* u_{j'LJ'N} \\ &+ \sum_{jj'JJ'LN} A_{jLJN}^{j'J'}\ U_{jj'}(t) \frac{i\hbar}{2\mu} \int_0^t dt'\ U_{j'j}(t') \left[u_{n'}(r) \frac{\partial}{\partial r} u_n^*(r) - u_n^*(r) \frac{\partial}{\partial r} u_{n'}(r) \right]_{r=R},\end{aligned} \tag{A.16}$$

where the phase $U_{jj'}(t) = \exp\left(\frac{i(E_j - E_{j'})}{\hbar} t\right)$ derive from the rescaling of the radial wave function. The current corresponding to τ_w is

$$k_w = U_{j'j} j_w. \tag{A.17}$$

APPENDIX B

Arnoldi and Lanzcos processes

The orthogonalization procedure used in the Krylov subspace method (see section 6.2.3) are summarized in the following. For more detail, refer to the literature, e.g. [98–100] and references therein.

For the m dimensional Krylov subspace generated by a matrix A and a vector b,

$$\mathcal{K}_m(A, b) = \text{span}\{b, Ab, A^2b, \ldots, A^{m-1}b\} \tag{B.1}$$

the Arnoldi process is a stabilized version of the Gram-Schmidt process for obtaining an orthonormal basis $V_m = [\mathbf{v}_1, \mathbf{v}_2, \ldots, \mathbf{v}_m]$ of the Krylov subspace. It starts with the normed vector b and iteratively projects out previous vectors. At each step, the matrix A is applied to the resulting vector instead of successively to the original vector b. This is what makes it stable. Along the way, the overlaps with previous vectors, and the final norm of the vector, is stored in an upper Hessenberg matrix H_m (i.e. upper triangular with one additional lower off-diagonal). The overlaps are stored in the upper triangle just like in the Gram-Schmidt QR decomposition algorithm. The final norms are stored in the lower off-diagonal. The matrix H_m satisfies $AV_m = V_m H_m \Rightarrow V_m^H A V_m = H_m$, i.e. H_m is the projection of A onto the Krylov subspace.

If A is Hermitian, then, since H_m has zeroes below the first lower off-diagonal, it must also have zeros above the first upper off-diagonal. That is, it must be tridiagonal. Effectively, this means that most overlaps are zero, and the vector in each iteration is automatically orthogonal to all but the previous vector.

The Lanzcos process is just the Arnoldi process where only the previous vector, and not all previous vectors are projected out in each step.

Bibliography

[1] B. Friedrich and D. Herschbach. "Alignment and trapping of molecules in intense laser fields". *Phys. Rev. Lett.* **74**, 23 (1995), DOI: 10.1103/PhysRevLett.74.4623.

[2] T. Seideman. "Rotational excitation and molecular alignment in intense laser fields". *J. Chem. Phys.* **103**, 18 (1995), DOI: 10.1063/1.470206.

[3] T. Seideman. "On the dynamics of rotationally broad, spatially aligned wave packets". *J. Chem. Phys.* **115**, 13 (2001), DOI: 10.1063/1.1400131.

[4] T. Seideman. "Revival Structure of Aligned Rotational Wave Packets". *Phys. Rev. Lett.* **83**, 24 (1999), DOI: 10.1103/PhysRevLett.83.4971.

[5] H. Stapelfeldt and T. Seideman. "*Colloquium* : Aligning molecules with strong laser pulses". *Rev. Mod. Phys.* **75**, (2 2003), DOI: 10.1103/RevModPhys.75.543.

[6] J. Itatani et al. "Tomographic imaging of molecular orbitals". *Nature* **432**, 7019 (2004), DOI: 10.1038/nature03183.

[7] C. B. Madsen et al. "Manipulating the Torsion of Molecules by Strong Laser Pulses". *Phys. Rev. Lett.* **102**, 7 (2009), DOI: 10.1103/PhysRevLett.102.073007.

[8] J. Wu et al. "Ultrafast optical imaging by molecular wakes". *Appl. Phys. Lett.* **97**, 16 (2010), DOI: doi:10.1063/1.3505138.

[9] J. Maurer et al. "Molecular-Frame 3D Photoelectron Momentum Distributions by Tomographic Reconstruction". *Phys. Rev. Lett.* **109**, 12 (2012), DOI: 10.1103/PhysRevLett.109.123001.

[10] J. Küpper et al. "X-Ray Diffraction from Isolated and Strongly Aligned Gas-Phase Molecules with a Free-Electron Laser". *Phys. Rev. Lett.* **112**, 8 (2014), DOI: 10.1103/PhysRevLett.112.083002.

[11] R. Boll et al. "Imaging molecular structure through femtosecond photoelectron diffraction on aligned and oriented gas-phase molecules". *Faraday Discuss.* (2014). DOI: 10.1039/C4FD00037D.

[12] B. Wolter et al. "Ultrafast electron diffraction imaging of bond breaking in di-ionized acetylene". *Science* **354**, 6310 (2016), DOI: 10.1126/science.aah3429.

[13] K. K. Lehmann and G. Scoles. "SUPERFLUID HELIUM: The Ultimate Spectroscopic Matrix?" *Science* **279**, 5359 (1998), DOI: 10.1126/science.279.5359.2065.

[14] J. P. Toennies and A. F. Vilesov. "Superfluid Helium Droplets: A Uniquely Cold Nanomatrix for Molecules and Molecular Complexes". *Angew. Chem. Int. Ed.* **43**, 20 (2004), DOI: 10.1002/anie.200300611.

[15] M. Y. Choi et al. "Infrared spectroscopy of helium nanodroplets: novel methods for physics and chemistry". *Int. Rev. Phys. Chem.* **25**, 1 (2006), DOI: 10.1080/01442350600625092.

[16] D. Pentlehner et al. "Laser-induced adiabatic alignment of molecules dissolved in helium nanodroplets". *Phys. Rev. A* **87**, 6 (2013), DOI: 10.1103/PhysRevA.87.063401.

[17] D. Pentlehner et al. "Impulsive Laser Induced Alignment of Molecules Dissolved in Helium Nanodroplets". *Phys. Rev. Lett.* **110**, 9 (2013), DOI: 10.1103/PhysRevLett.110.093002.

[18] L. Christiansen et al. "Alignment enhancement of molecules embedded in helium nanodroplets by multiple laser pulses". *Phys. Rev. A* **92**, 5 (2015), DOI: 10.1103/PhysRevA.92.053415.

[19] L. Christiansen. "Laser Induced Alignment of Molecules Embedded in Helium Droplets: Exploration and Potential Applications". PhD thesis. Aarhus University, 2015.

[20] N. B. Brauer et al. "Critical Landau Velocity in Helium Nanodroplets". *Phys. Rev. Lett.* **111**, 15 (2013), DOI: 10.1103/PhysRevLett.111.153002.

[21] E. J. Yarmchuk and R. E. Packard. "Photographic studies of quantized vortex lines". *Journal of Low Temperature Physics* **46**, 5-6 (1982), DOI: 10.1007/bf00683912.

[22] W. Vinen and J. Niemela. "Quantum Turbulence". *Journal of Low Temperature Physics* **128**, 5-6 (2002), DOI: 10.1023/A:1019695418590.

[23] L. F. Gomez, E. Loginov, and A. F. Vilesov. "Traces of Vortices in Superfluid Helium Droplets". *Phys. Rev. Lett.* **108**, 15 (2012), DOI: 10.1103/PhysRevLett.108.155302.

[24] L. F. Gomez et al. "Shapes and vorticities of superfluid helium nanodroplets". *Science* **345**, 6199 (2014), DOI: 10.1126/science.1252395.

[25] F. Ancilotto, M. Pi, and M. Barranco. "Vortex arrays in nanoscopic superfluid helium droplets". *Phys. Rev. B* **91**, 10 (2015), DOI: 10.1103/PhysRevB.91.100503.

[26] S. Angus and K. de Reuck, eds. *International Theromdynamic Tables of the Fluid State: Helium*. Pergamon Press, 1971. ISBN: 0080209572.

[27] R. J. Donnelly. "The two-fluid theory and second sound in liquid helium". *Phys. Today* **62**, 10 (2009), DOI: 10.1063/1.3248499.

[28] S. Grebenev et al. “Spectroscopic investigation of OCS (p-H2)n (n = 1–16) complexes inside helium droplets: Evidence for superfluid behavior”. *J. Chem. Phys.* **132**, 6 (2010), DOI: doi:10.1063/1.3274509.

[29] F. London. “On the Bose-Einstein Condensation”. *Phys. Rev.* **54**, (11 1938), DOI: 10.1103/PhysRev.54.947.

[30] A. Leggett. “Superfluidity”. *Rev. Mod. Phys.* **71**, (2 1999), DOI: 10.1103/RevModPhys.71.S318.

[31] W. F. Vinen. “An Introduction to Quantum Turbulence”. *Journal of Low Temperature Physics* **145**, 1-4 (2006), DOI: 10.1007/s10909-006-9240-6.

[32] W. Vinen. “An introduction to quantum turbulence”. *Philosophical Transactions of the Royal Society A: Mathematical, Physical and Engineering Sciences* **366**, 1877 (2008), DOI: 10.1098/rsta.2008.0084.

[33] F. Dalfovo and S. Stringari. “Helium nanodroplets and trapped Bose–Einstein condensates as prototypes of finite quantum fluids”. *J. Chem. Phys.* **115**, 22 (2001), DOI: 10.1063/1.1424926.

[34] J. S. Brooks and R. J. Donnelly. “The calculated thermodynamic properties of superfluid helium-4”. *Journal of Physical and Chemical Reference Data* **6**, 1 (1977), DOI: http://dx.doi.org/10.1063/1.555549.

[35] L. Tisza. “Transport Phenomena in Helium II”. *Nature* **141**, 3577 (1938), DOI: 10.1038/141913a0.

[36] L Landau. “Theory of the superfluidity of helium II”. *Phys. Rev.* **60**, 4 (1941), DOI: 10.1103/PhysRev.60.356.

[37] D. V. Osborne. “Second Sound in Liquid Helium II”. *Proc. Phys. Soc. A* **64**, 2 (1951), DOI: 10.1088/0370-1298/64/2/302.

[38] A. Leitner. *Alfred Leitner’s Old Physics Stories*. http://alfredleitner.com/superfluid.html. Also available on YouTube https://www.youtube.com/watch?v=S3O-5KTYq6o&list=PL442F47F12D99C4D2&index=1. Accessed 2014-12-18. 1963.

[39] R. P. Feynman. “Atomic Theory of the Two-Fluid Model of Liquid Helium”. *Phys. Rev.* **94**, (2 1954), DOI: 10.1103/PhysRev.94.262.

[40] R. P. Feynman and M. Cohen. “Energy Spectrum of the Excitations in Liquid Helium”. *Phys. Rev.* **102**, (5 1956), DOI: 10.1103/PhysRev.102.1189.

[41] M. Cohen and R. P. Feynman. “Theory of Inelastic Scattering of Cold Neutrons from Liquid Helium”. *Phys. Rev.* **107**, (1 1957), DOI: 10.1103/PhysRev.107.13.

[42] D. E. Galli, E. Cecchetti, and L. Reatto. “Rotons and Roton Wave Packets in Superfluid ^{4}He”. *Phys. Rev. Lett.* **77**, (27 1996), DOI: 10.1103/PhysRevLett.77.5401.

[43] D. R. Allum, P. V. E. McClintock, and A. Phillips. "The Breakdown of Superfluidity in Liquid ^{4}He: An Experimental Test of Landau's Theory". *Philos. Trans. R. Soc. (London) Ser. A* **284**, 1320 (1977), DOI: 10.1098/rsta.1977.0008.

[44] M. Hartmann et al. "Direct Spectroscopic Observation of Elementary Excitations in Superfluid He Droplets". *Phys. Rev. Lett.* **76**, 24 (1996), DOI: 10.1103/PhysRevLett.76.4560.

[45] R. P. Feynman. "Chapter II: Application of Quantum Mechanics to Liquid Helium". Ed. by C. J. Gorter. Vol. 1. Progress in Low Temperature Physics. Elsevier, 1955, pp. 17 –53. DOI: http://dx.doi.org/10.1016/S0079-6417(08)60077-3.

[46] R. Feynman. "Superfluidity and Superconductivity". *Rev. Mod. Phys.* **29**, (2 1957), DOI: 10.1103/RevModPhys.29.205.

[47] W. V. Alphen et al. "The dependence of the critical velocity of the superfluid on channel diameter and film thickness". *Physics Letters* **20**, 5 (1966), DOI: 10.1016/0031-9163(66)90958-9.

[48] E. L Andronikashvilli. "Direct observation of two types of motion in helium II". *J. Phys U.S.S.R* **10**, (201 1946). I have been unable to retrieve the original paper, but the experiment is mentioned in numerous articles, e. g. Refs. 49, 105.

[49] S. Grebenev, J. P. Toennies, and A. F. Vilesov. "Superfluidity Within a Small Helium-4 Cluster: The Microscopic Andronikashvili Experiment". *Science* **279**, 5359 (1998), DOI: 10.1126/science.279.5359.2083.

[50] S. Grebenev et al. "The rotational spectrum of single OCS molecules in liquid ^{4}He droplets". *J. Chem. Phys.* **112**, 10 (2000), DOI: 10.1063/1.481011.

[51] D. M. Brink and S. Stringari. "Density of states and evaporation rate of helium clusters". *Z. Phys. D: At. Mol. Clusters* **15**, 3 (1990), DOI: 10.1007/BF01437187.

[52] M. Hartmann et al. "Rotationally Resolved Spectroscopy of SF_6 in Liquid Helium Clusters: A Molecular Probe of Cluster Temperature". *Phys. Rev. Lett.* **75**, 8 (1995), DOI: 10.1103/PhysRevLett.75.1566.

[53] J. H. Nielsen. "Laser-Induced Alignment and Orientation of Quantum-State Selected Molecules and Molecules in Liquid Helium Droplets". PhD thesis. Aarhus: Aarhus University, 2012.

[54] C. Z. Bisgaard. "Laser induced alignment". PhD thesis. Aarhus University, 2006.

[55] L. Christensen et al. "Deconvoluting nonaxial recoil in Coulomb explosion measurements of molecular axis alignment". *Phys. Rev. A* **94**, (2 2016), DOI: 10.1103/PhysRevA.94.023410.

[56] T. Seideman and E. Hamilton. "Nonadiabatic Alignment by Intense Pulses. Concepts, Theory, and Directions". *Adv. At. Mol. Opt. Phys* **52**, (2005), DOI: 10.1016/S1049-250X(05)52006-8.

[57] B. Friedrich and D. Herschbach. "Polarization of Molecules Induced by Intense Nonresonant Laser Fields". *J. Phys. Chem.* **99**, 42 (1995), DOI: 10.1021/j100042a051.

[58] R. N. Zare. *Angular Momentum: Understanding Spatial Aspects in Chemistry and Physics*. Wiley-Interscience, 1991. ISBN: 0471858927.

[59] I. S. Averbukh and R. Arvieu. "Angular Focusing, Squeezing, and Rainbow Formation in a Strongly Driven Quantum Rotor". *Phys. Rev. Lett.* **87**, 16 (2001), DOI: 10.1103/PhysRevLett.87.163601.

[60] M. Leibscher, I. S. Averbukh, and H. Rabitz. "Molecular Alignment by Trains of Short Laser Pulses". *Phys. Rev. Lett.* **90**, 21 (2003), DOI: 10.1103/PhysRevLett.90.213001.

[61] M. Leibscher, I. S. Averbukh, and H. Rabitz. "Enhanced molecular alignment by short laser pulses". *Phys. Rev. A* **69**, 1 (2004), DOI: 10.1103/PhysRevA.69.013402.

[62] J. J. Sakurai. *Modern Quantum Mechanics*. Addison Wesley, 1993. ISBN: 0201539292.

[63] V. Dribinski et al. "Reconstruction of Abel-transformable images: The Gaussian basis-set expansion Abel transform method". *Rev. Sci. Instrum.* **73**, 7 (2002), DOI: 10.1063/1.1482156.

[64] B. Gough. *GNU Scientific Library Reference Manual - Third Edition*. 3rd. Network Theory Ltd., 2009. ISBN: 0954612078, 9780954612078.

[65] D. Goldberg. "What Every Computer Scientist Should Know About Floating-point Arithmetic". *ACM Comput. Surv.* **23**, 1 (1991), DOI: 10.1145/103162.103163.

[66] K. Schulten and R. G. Gordon. "Exact recursive evaluation of 3j- and 6j-coefficients for quantum-mechanical coupling of angular momenta". *J. Math. Phys.* **16**, 10 (1975), DOI: 10.1063/1.522426.

[67] *SLATEC Common Mathematical Library, Version 4.1, July 1993. A comprehensive software library containing over 1400 general purpose mathematical and statistical routines written in Fortran 77.* http://www.netlib.org/slatec/, accessed 21-April-2016.

[68] J. H. Luscombe and M. Luban. "Simplified recursive algorithm for Wigner 3j and 6j symbols". *Phys. Rev. E* **57**, (6 1998), DOI: 10.1103/PhysRevE.57.7274.

[69] J. Rasch and A. C. H. Yu. "Efficient Storage Scheme for Precalculated Wigner 3 j , 6 j and Gaunt Coefficients". *SIAM J. Sci. Comput.* **25**, 4 (2004), DOI: 10.1137/s1064827503422932.

[70] J. P. M. Flude. "The Edmonds asymptotic formulas for the 3j and 6j symbols". *Journal of Mathematical Physics* **39**, 7 (1998), DOI: http://dx.doi.org/10.1063/1.532474.

[71] P. W. Milonni and J. H. Eberly. *Laser Physics*. Wiley, 2010. ISBN: 0470387718.

[72] J. H. Nielsen et al. "Stark-selected beam of ground-state OCS molecules characterized by revivals of impulsive alignment". *Phys. Chem. Chem. Phys.* **13**, (2011), DOI: 10.1039/c1cp21143a.

[73] H. Stapelfeldt. "Alignment of molecules by strong laser pulses". *The European Physical Journal D - Atomic, Molecular and Optical Physics* **26**, 1 (2003), DOI: 10.1140/epjd/e2003-00064-2.

[74] J. G. Underwood et al. "Velocity map imaging with non-uniform detection: Quantitative molecular axis alignment measurements via Coulomb explosion imaging". *Review of Scientific Instruments* **86**, 7 (2015), DOI: 10.1063/1.4922137.

[75] A. A. Søndergaard. *Laser-induced alignment calculator for symmetric top molecules*. https://github.com/femtolab-aarhus/alignment_calculator. 2016.

[76] B. Bransden and C. Joachain. *Physics of Atoms and Molecules (2nd Edition)*. Pearson, 2003. ISBN: 058235692X.

[77] U. Even et al. "Cooling of large molecules below 1 K and He clusters formation". *J. Chem. Phys.* **112**, 18 (2000), DOI: 10.1063/1.481405.

[78] A. V. Jørgensen and L. Christensen. "Spectral method for laser pulse characterization". Unpublished notes, derivations and simulations. 2016.

[79] M. Lewerenz, B. Schilling, and J. P. Toennies. "A new scattering deflection method for determining and selecting the sizes of large liquid clusters of 4He". *Chemical Physics Letters* **206**, 1–4 (1993), DOI: 10.1016/0009-2614(93)85569-A.

[80] A. Bohr and B. R. Mottelson. *Nuclear Structure*. World Scientific Pub Co Inc, 1998. ISBN: 9810239807.

[81] V. Weisskopf. "Statistics and Nuclear Reactions". *Phys. Rev.* **52**, (4 1937), DOI: 10.1103/PhysRev.52.295.

[82] H. Buchenau et al. "Mass spectra and time-of-flight distributions of helium cluster beams". *J. Chem. Phys.* **92**, 11 (1990), DOI: doi:10.1063/1.458275.

[83] A. T.J. B. Eppink and D. H. Parker. "Velocity map imaging of ions and electrons using electrostatic lenses: Application in photoelectron and photofragment ion imaging of molecular oxygen". *Rev. Sci. Instrum.* **68**, 9 (1997), DOI: 10.1063/1.1148310.

[84] R. J. LeRoy. "Spectroscopic Reassignment and Ground-State Dissociation Energy of Molecular Iodine". *The Journal of Chemical Physics* **52**, 5 (1970), DOI: 10.1063/1.1673357.

[85] J. Tellinghuisen. "Resolution of the visible-infrared absorption spectrum of I2 into three contributing transitions". *The Journal of Chemical Physics* **58**, 7 (1973), DOI: 10.1063/1.1679584.

[86] H. Sakai et al. "Metastable Triply Charged Diatomic Molecules Produced with Femtosecond Pulses". *Phys. Rev. Lett.* **81**, 11 (1998), DOI: 10.1103/PhysRevLett.81.2217.

[87] A. Braun and M. Drabbels. "Photodissociation of alkyl iodides in helium nanodroplets. II. Solvation dynamics". *J. Chem. Phys.* **127**, 11 (2007), DOI: 10.1063/1.2767262.

[88] M. Gruebele et al. "Femtosecond temporal spectroscopy and direct inversion to the potential: Application to iodine". *Chemical Physics Letters* **166**, 5-6 (1990), DOI: 10.1016/0009-2614(90)87134-d.

[89] P. M. Felker. "Rotational coherence spectroscopy: studies of the geometries of large gas-phase species by picosecond time-domain methods". *J. Phys. Chem.* **96**, 20 (1992), DOI: 10.1021/j100199a005.

[90] F. Filsinger et al. "Quantum-state selection, alignment, and orientation of large molecules using static electric and laser fields". *J. Chem. Phys.* **131**, 6 (2009), DOI: 10.1063/1.3194287.

[91] J. M. Hutson and A. E. Thornley. "Atom-spherical top van der Waals complexes: A theoretical study". *J. Chem. Phys.* **100**, 4 (1994), DOI: 10.1063/1.466499.

[92] K. J. Miller. "Calculation of the molecular polarizability tensor". *Journal of the American Chemical Society* **112**, 23 (1990), DOI: 10.1021/ja00179a045.

[93] *NIST Computational Chemistry Comparison and Benchmark Database*. http://cccbdb.nist.gov/, consulted on 2015-11-10.

[94] G. Maroulis et al. "Electrooptical Properties and Molecular Polarization of Iodine, I2". *The Journal of Physical Chemistry A* **101**, 5 (1997), DOI: 10.1021/jp962578u.

[95] H. Farrokhpour and M. Tozihi. "Ab initio intermolecular potential energy surfaces of He-CS_2, Ne-CS_2, and Ar-CS_2". *Mol. Phys.* **111**, (2013),

[96] G. Galinis et al. "Formation of coherent rotational wavepackets in small molecule-helium clusters using impulsive alignment". *Faraday Discuss.* **171**, (0 2014), DOI: 10.1039/C4FD00099D.

[97] L. Garci'a-Gutierrez et al. "Intermolecular Ab Initio Potential and Spectroscopy of the Ground State of HeI 2 Complex Revisited". *J. Phys. Chem. A* **113**, 19 (2009), DOI: 10.1021/jp901250u.

[98] C Leforestier et al. "A comparison of different propagation schemes for the time dependent Schrödinger equation". *Journal of Computational Physics* **94**, 1 (1991), DOI: 10.1016/0021-9991(91)90137-a.

[99] C. Moler and C. V. Loan. "Nineteen Dubious Ways to Compute the Exponential of a Matrix, Twenty-Five Years Later". *SIAM Rev.* **45**, 1 (2003), DOI: 10.1137/s00361445024180.

[100] R. Sidje. "Expokit: A software package for computing matrix exponentials". *ACM Trans. Math. Softw.* **24**, 1 (1998),

[101] R. Kosloff and H. Tal-Ezer. "A direct relaxation method for calculating eigenfunctions and eigenvalues of the schrödinger equation on a grid". *Chemical Physics Letters* **127**, 3 (1986), DOI: 10.1016/0009-2614(86)80262-7.

[102] G. Galinis et al. "Probing the structure and dynamics of molecular clusters using rotational wavepackets". *arXiv:1402.5401 [physics]* (2014).

[103] R. Kosloff and D. Kosloff. "Absorbing boundaries for wave propagation problems". *Journal of Computational Physics* **63**, 2 (1986), DOI: 10.1016/0021-9991(86)90199-3.

[104] K. Nauta and R. E. Miller. "The vibrational and rotational dynamics of acetylene solvated in superfluid helium nanodroplets". *The Journal of Chemical Physics* **115**, 18 (2001), DOI: 10.1063/1.1412257.

[105] T. Zeng and P.-N. Roy. "Microscopic molecular superfluid response: theory and simulations". *Reports on Progress in Physics* **77**, 4 (2014), DOI: 10.1088/0034-4885/77/4/046601.

[106] R. Schmidt and M. Lemeshko. "Rotation of Quantum Impurities in the Presence of a Many-Body Environment". *Phys. Rev. Lett.* **114**, (20 2015), DOI: 10.1103/PhysRevLett.114.203001.

[107] R. Schmidt and M. Lemeshko. "Deformation of a Quantum Many-Particle System by a Rotating Impurity". *Phys. Rev. X* **6**, (1 2016), DOI: 10.1103/PhysRevX.6.011012.